SLAC-PUB-5704
KEK-TH-284
DTP/91/78
TU-397
KEK preprint 91-6
UT-594
March 1992
(M)

Top Quark Pair Production Near Threshold*

Y. Sumino[1], K. Fujii[2], K. Hagiwara[2,3], H. Murayama[4], C.-K. Ng[5]

[1]Department of Physics, University of Tokyo, Tokyo, 113 Japan
[2]KEK, Tsukuba, Ibaraki, 305 Japan
[3]Department of Physics, University of Durham, DH1 3LE, U.K.
[4]Department of Physics, Tohoku University, Sendai, 980 Japan
[5]Stanford Linear Accelerator Center, Stanford University, Stanford, CA 94309 USA

Abstract

We present a novel formalism to calculate the total and the differential cross sections for heavy unstable top-quark pair production near threshold. Within the context of the non-relativistic quark model, we introduce the running toponium width, $\Gamma_{\rm tt}(E,{\rm p})$, in the Schrödinger equation for the three-point Green's function that governs the $t\bar{t}$ contribution to the e^+e^- annihilation process. The effect of the running of the width is found to be significant in two aspects: (i) it takes account of the phase space volume for the decay process $t\bar{t} \to bW^+\bar{b}W^-$, and provides a consistent framework for calculating the differential cross sections; and (ii) it reduces the widths of the low-lying resonances to considerably less than $2\Gamma_t(m_t^2)$. Furthermore, the running of the width causes the total cross section to decrease significantly at c.m. energies below the first "resonance" enhancement, whereas it makes the "peak" cross section more distinct than is obtained in the fixed toponium width approximation. We use the two-loop improved QCD potential in our calculation, and the $\alpha_s(m_Z)_{\overline{\rm MS}}$ dependences of the total and differential cross sections are studied quantitatively. We find that the correlations in the α_s and m_t measurements are opposite in the total and differential cross sections, and that simultaneous measurements would lead to an accurate determination of both parameters.

Submitted to Physical Review D

Work supported in part by the UK Science and Engineering Research Council, the Department of Energy, contract DE-AC03-76SF00515 (SLAC), and by MESC (Ministry of Education, Science and Culture Japan) under Grant-in-Aid International Science Research Program No. 03041087.

1 Introduction

The threshold region of heavy quark production has always been an ideal laboratory for onium spectroscopy. As the experimental lower limit on the top mass continued to increase, however, physicists started worrying about the effect of the top quark decay width, which grows like m_t^3 for $m_t \gg m_b + M_W$ [1]. A large width would smear out resonance structures [2,3,4] and might conceal most of the informations otherwise available. This seemingly unwelcome feature of a heavy top quark, on the contrary, turned out to be advantageous in many ways, as was first pointed out by Fadin and Khoze in their pioneering papers [5]. The key observation is the fact that the large top quark width should act as an infrared cutoff, or a physical "smearing" [6] of the total cross section which prevents the non-perturbative regime of QCD affecting the threshold cross section. Thus, the threshold region for heavy top pair production provides us with a very clean test of perturbative QCD. Moreover, since the QCD contribution is now predictable over the whole threshold region, we may even hope to extract the effect of Higgs exchange [7,8] from the precision measurement of the threshold cross section. These new possibilities triggered the recent works by several authors [9,10,11,12].

In this paper, we attempt to construct a basis for the quantitative study of the process, which can be an ideal place to measure the top quark mass, its width, as well as the strong coupling constant. The Green's function method introduced by Fadin and Khoze [5] and later refined by Strassler and Peskin [9] provides us with a handy tool to calculate the total cross section, without the need for summing over many resonance states [8,10,13]. At first sight, it seems to be possible to apply their Green's function approach to the calculation of differential cross sections, simply by allowing the decaying top quark to follow the Breit-Wigner resonance shape. Unfortunately, when we naively do this and carry out the phase space integration, we immediately run into a trouble: the optical theorem does not hold, or the integral of the differential cross section does not reproduce the total cross section as calculated from the imaginary part of the relevant Green's function. We find that this lack of unitarity necessitates the introduction of the running toponium width, which is smaller than twice the on-shell top quark width when the available energy is small, or when the constituent top quark kinetic energy is large under the influence of an attractive potential. After the effect is appropriately taken into account, the differential cross sections become consistent with unitarity and they provide us with additional useful information on the physics of the $t\bar{t}$ threshold. In particular, we find that the correlation between the α_s and m_t measurements for the differential

cross sections is opposite to that expected for the total cross section, which gives us an opportunity to determine the two parameters accurately.

This is, however, not the whole story. The most essential effect of the running toponium width is found in the resonance structures, i.e. in the energy dependence of the total $t\bar{t}$ production cross section. The running of the top quark width alters, in a non-trivial way, the positions of the poles of the Green's function on the complex energy plane. For example, the rise of the total cross section at the threshold is made significantly steeper than the prediction based on the fixed toponium width approximation. We will discuss the physical significance of the running toponium width in detail, and, we compare its running behavior to that suggested by the electroweak gauge invariance.

Our paper is organized as follows. In section 2, we start with an intuitive illustration of what should happen to a $t\bar{t}$ pair produced in the threshold region, which subsequently decays into a pair of bW under the influence of non-perturbative QCD interactions. Then, in section 3, we present the theoretical framework based on the non-relativistic formalism, thereby introducing a three-point Green's function to describe the production and the decay of the toponium. Section 4 gives a concrete definition of the running toponium width and demonstrates how it restores the unitarity relation and how it affects the prediction for the threshold cross section, by using a simple Coulombic potential for illustration. In section 5, we introduce our QCD potential, and other previously proposed potentials, to be used in the following sections. Observables that are derived from the total and differential cross sections are closely examined in section 6. We find that simultaneous measurements of the total and differential cross sections allow an efficient determination of the basic parameters, α_s and m_t, in the threshold region. In section 7, we give a brief discussion regarding the basis of our non-relativistic formulation in terms of a relativistic field theoretical approach. We summarize our findings in section 8. Technical details, including a fairly detailed description of our calculational procedure, are explained in appendices.

2 Physical Picture

In this section, we present an intuitive picture of the physics in the $t\bar{t}$ threshold region. We emphasize that this process can be reliably described by perturbative QCD, due to the large mass and width of the top quark.

We are concerned with the process where t and $\bar{t}$ are pair created and subsequently

decay into bW's (see Fig. 1);

$$e^+e- \to \gamma, Z \to t\bar{t}("\Theta") \to (bW^+)(\bar{b}W^-). \tag{2.1}$$

Re-annihilation of the $t\bar{t}$ pair is found to be negligible for $m_t \gtrsim 100$ GeV [8,13]. We would like to treat the production and decays of $t\bar{t}$ in the lowest order of the electroweak theory while keeping the QCD interactions between the $t\bar{t}$ state. This is achieved formally by splitting the Lagrangean into two parts

$$\mathcal{L} = \mathcal{L}_0 + \mathcal{L}_{\rm EW}, \tag{2.2}$$

where $\mathcal{L}_0$ contains the strong interaction, and by treating the electroweak interactions $\mathcal{L}_{\rm EW}$ perturbatively. The S matrix element for the process (2.1) is then expressed as

$$S_{fi} \;=\; < bW^+\bar{b}W^- | T e^{i\int d^4x \mathcal{L}_{\rm EW}} | e^+e^- >, \tag{2.3}$$

and the lowest-order contribution appears at the fourth order of the electroweak interaction:

$$\begin{aligned} S_{fi} \;=\; & \int d^4x d^4y d^4z d^4\omega \\ & \times \frac{g_W}{\sqrt{2}} V_{tb}^* [\bar{u}_b \gamma^\mu \frac{1-\gamma_5}{2}]_\alpha \epsilon^*_{\mu W^+} e^{i(p_b + p_{W^+})\cdot x} \\ & \times \frac{g_W}{\sqrt{2}} V_{tb} [\gamma^\nu \frac{1-\gamma_5}{2} v_{\bar{b}}]_\beta \epsilon^*_{\nu W^-} e^{i(p_{\bar{b}} + p_{W^-})\cdot y} \\ & \times \langle 0 \,|\, T\; t_\alpha(x) \bar{t}_\beta(y) : \bar{t}_\gamma(z) t_\delta(z) : |\, 0 \rangle \sum_{V=\gamma,Z} [v_V^t \gamma^\rho + a_V^t \gamma^\rho \gamma_5]_{\gamma\delta} \\ & \times \langle 0 \,|\, T\; V_\rho(z) V_\sigma^*(\omega) \,|\, 0 \rangle \, \bar{v}_{e^+} (v_V^e \gamma^\sigma + a_V^e \gamma^\sigma \gamma_5) u_{e^-} e^{-i(p_{e^-} + p_{e^+})\cdot\omega}. \end{aligned} \tag{2.4}$$

Here $g_W = e \sin\theta_W$ is the $SU(2)_L$ gauge coupling, v_V^f and a_V^f are the vector and axial-vector couplings of the fermion f and the neutral vector boson V ($=\gamma$ or Z), and V_{tb} is the KM matrix element. We note that the repeated indices μ, ν, ρ and σ are four-vector indices (in the Bjorken-Drell metric) whereas α, β, γ and δ are four-spinor indices. The vector boson propagators are expressed in the lowest-order of $\mathcal{L}_{\rm EW}$ as

$$< 0|T\; V_\rho(z) V_\sigma^*(\omega)|0 > = \int \frac{d^4p}{(2\pi)^4} e^{-ip\cdot(z-\omega)} \frac{-ig_{\rho\sigma}}{p^2 - m_V^2 + im_V\Gamma_V} \tag{2.5}$$

for $V = \gamma$ and Z, in the Feynman gauge. In the amplitude (2.4), we treat the b and $\bar{b}$ quarks as free particles and ignore their strong interactions [14].

The non-trivial and interesting part of the process is contained in the three-point Green's function

$$K(x,y,z)_{\alpha\gamma,\delta\beta} \;=\; \langle 0\,|\,T\,t_\alpha(x)\,\bar{t}_\beta(y):\bar{t}_\gamma(z)t_\delta(z):|\,0\,\rangle\,, \tag{2.6}$$

which expresses the amplitude where a $t\bar{t}$ pair is created at a space-time point z and the t ($\bar{t}$) quark decays at another point x (y), see Fig. 1. This three-point function contains the effect of full QCD interactions, in the absence of which it reduces to the product of t and $\bar{t}$ free propagators. Since the created t and $\bar{t}$ will have small velocities near the threshold, the system related to this Green's function is regarded as a non-relativistic t and $\bar{t}$ system which is bounded by the static potential $V(|\mathbf{r}_1-\mathbf{r}_2|)$ to form the toponium resonances. We can then use the non-relativistic Schrödinger equation to estimate the effect of the non-perturbative strong interactions. It is expected that the process probes the short distance behavior of the potential due to the large t-quark mass.

The main contribution to the potential $V(r)$ comes from the QCD interaction. At short distances $r \ll \Lambda_{QCD}^{-1}$, the perturbative picture of one-gluon exchange becomes valid, and hence $V(r)$ behaves like the Coulomb potential near the origin:

$$V(r) \sim -C_F\frac{\alpha_s}{r}, \tag{2.7}$$

with the color factor $C_F = 4/3$. We note therefore that there are 3 typical time scales in this system, namely

$$\Gamma_\Theta^{-1} \qquad \text{toponium lifetime,} \tag{2.8}$$

$$a_0 = (\alpha_s m_t)^{-1} \qquad \text{Bohr radius,} \tag{2.9}$$

$$a_0/\alpha_s \qquad (\text{Coulomb level})^{-1}. \tag{2.10}$$

Let us first examine the time evolution of the system in the case where $\Gamma_\Theta^{-1} \gg a_0/\alpha_s \gg a_0$. Suppose that at $t = 0$, a $t\bar{t}$ pair is created at the space point $\mathbf{x} = 0$ (see Fig. 2). At this moment, the wave packet of the $t\bar{t}$ system is like a δ function (with the size of $\sim 1/m_t$) at the origin, which is the superposition of all plane waves with an equal weight:

$$\psi(\mathbf{x})\Big|_{t=0} \simeq \delta^3(\mathbf{x}) = \int \tfrac{d^3\mathbf{p}}{(2\pi)^3}\, e^{i\mathbf{p}\cdot\mathbf{x}-iEt}\Big|_{t=0}. \tag{2.11}$$

All the plane waves quickly spread outwards from the origin $\mathbf{x} = 0$. Each plane wave spreads until it reaches the potential barrier at a distance of the Bohr radius. It is then bounced back and starts oscillating within the potential wall. The fastest wave (we are

concerned with the group velocity here) will reach the barrier at the time $t = a_0$ ($|\mathbf{p}| = \infty$). Lower momentum waves will reach there successively. It is from the time $t \sim a_0/\alpha_s$, when the typical waves related to the bound states reach the barrier, that the concept of various resonance states becomes meaningful. We may then say that the toponium is formed. The velocity of the typical wave is equal to α_s, which is a familiar picture for the Coulomb potential problem. These resonance states will remain until the t or $\bar{t}$ quark decays at the time scale Γ_Θ^{-1}. The waves that have momentum less than Γ_Θ/α_s will never reach the potential wall.

In the realistic case, $m_t \sim 100$ to 200GeV, the lifetime of toponium and the time scale for resonance formation are of the same order of magnitude,

$$\Gamma_\Theta^{-1} \sim a_0/\alpha_s. \tag{2.12}$$

It is then expected from the above picture that this system will probe the QCD potential since

$$\Gamma_\Theta^{-1} \gg a_0, \tag{2.13}$$

so that the waves oscillate a considerable number of times within the potential barrier before the decay occurs. Also, because

$$\Gamma_\Theta^{-1} \lesssim \Lambda_{QCD}^{-1}, \tag{2.14}$$

t and $\bar{t}$ quarks decay via the electroweak interaction before the hadronization effect becomes significant [2,4]. Lower momentum waves with $|\mathbf{p}| \lesssim \Gamma_\Theta/\alpha_s$ do not feel the QCD potential. Thus, we are free from the uncertainties coming from non-perturbative QCD at long distances. We have confirmed the observation [9] that indeed the total cross section is quite insensitive to the long distance behavior of $V(r)$ near the threshold.

The characteristic features may be summarized as follows. High momentum waves with $|\mathbf{p}| > \Gamma_\Theta/\alpha_s \sim 1/a_0$ reach the potential wall before the top decay, and the $t\bar{t}$ production cross section will be affected by the toponium resonance formation. On the other hand, the lower momentum waves with $|\mathbf{p}| < \Gamma_\Theta/\alpha_s$ do not reach the potential wall, and the details of the multiple resonance structure that is predicted for the stable top quark will be smeared out. We are no longer able to resort to the spectroscopy to determine the form of $V(r)$. It is necessary therefore to consider the interplay among the various resonance states.

3 Non-Relativistic Formulation

In this section, we study the non-relativistic approximation to the non-perturbative binding effects between t and $\bar{t}$ in the threshold region. We derive formulas for the differential and total cross sections in terms of Green's functions of the Schrödinger equation.

It is known [15] that near the threshold of heavy quark anti-quark pair creation, the QCD interaction between the pair is approximately described by the non-relativistic Hamiltonian with a spin-independent instantaneous potential

$$\begin{aligned}\mathcal{H} &= \psi_1^\dagger\left(m_t - \frac{\Delta}{2m_t}\right)\psi_1 + \psi_2^\dagger\left(m_t - \frac{\Delta}{2m_t}\right)\psi_2 \\ &\quad + \frac{1}{2}\int d^3\mathbf{x}'\,\psi_1^\dagger\psi_2'^\dagger V(|\mathbf{x}-\mathbf{x}'|)\psi_1\psi_2' \qquad (3.1)\end{aligned}$$

with $\psi_i = \psi_i(\mathbf{x},t)$, $\psi_i' = \psi_i(\mathbf{x}',t)$. ψ_1 and ψ_2 denote t and $\bar{t}$ fields, respectively. They are 2 component spinors satisfying

$$\frac{1+\gamma^0}{2}\psi_1 = \psi_1, \qquad (3.2)$$

$$\frac{1-\gamma^0}{2}\psi_2 = \psi_2. \qquad (3.3)$$

It is easy to find the propagators of this system for the one-particle and the two-particle states. For the one-particle states, since t or $\bar{t}$ has no partner to interact with, the propagator is given by that of a free particle as

$$K_1(x^0,\mathbf{x};y^0,\mathbf{y}) = \int \frac{d^4p}{(2\pi)^4}\frac{i\,e^{-ip\cdot(x-y)}}{p^0 - m_t - \mathbf{p}^2/2m_t + i\epsilon}. \qquad (3.4)$$

Note that we chose the boundary condition such that K_1 vanishes for $x^0 < y^0$. For the two particle states, we may split the propagator into two parts as

$$K_2(x^0,\mathbf{x}_1,\mathbf{x}_2;y^0,\mathbf{y}_1,\mathbf{y}_2) = K_G(x^0,\mathbf{x}_G;y^0,\mathbf{y}_G)\,K_r(x^0,\mathbf{x}_r;y^0,\mathbf{y}_r) \qquad (3.5)$$

where K_G and K_r represent the propagators in the c.m. coordinate and in the relative coordinate, respectively, with

$$\mathbf{x}_G = \frac{\mathbf{x}_1+\mathbf{x}_2}{2}, \qquad \mathbf{y}_G = \frac{\mathbf{y}_1+\mathbf{y}_2}{2}, \qquad (3.6)$$

$$\mathbf{x}_r = \mathbf{x}_1 - \mathbf{x}_2, \qquad \mathbf{y}_r = \mathbf{y}_1 - \mathbf{y}_2. \qquad (3.7)$$

K_G is a free propagator given by

$$K_G(x^0,\mathbf{x};y^0,\mathbf{y}) = \int \frac{d^4p}{(2\pi)^4}\frac{i\,e^{-ip\cdot(x-y)}}{p^0 - 2m_t - \mathbf{p}^2/4m_t + i\epsilon}, \qquad (3.8)$$

while K_r may be identified with the kernel for the time-dependent Schrödinger equation

$$\left\{-\frac{\Delta_{\mathbf{x}}}{m_t}+V(|\mathbf{x}|)-i\frac{\partial}{\partial x^0}\right\}K_r(x^0,\mathbf{x};y^0,\mathbf{y})=-i\,\delta^4(x-y) \tag{3.9}$$

with the boundary condition $K_G, K_r \equiv 0$ for $x^0 < y^0$.

We are now ready to express the three-point function $K(x,y,z)$ in (2.6) in terms of the propagators K_1 and K_2, see Fig. 1. Out of 6 different time orderings of the operators in K, only two orderings are relevant in the non-relativistic approximation, namely

$$\begin{aligned} K(x,y,z)_{\alpha\gamma,\delta\beta} &= \langle 0\,|\,T\,t_\alpha(x)\,\bar{t}_\beta(y)\,:\bar{t}_\gamma(z)t_\delta(z):\,|\,0\rangle \\ &= \left(\tfrac{1+\gamma^0}{2}\right)_{\alpha\gamma}\left(\tfrac{1-\gamma^0}{2}\right)_{\delta\beta}\Big[\int d^3\mathbf{r}\,K_1(x^0,\mathbf{x};y^0,\mathbf{r})\,K_2(y^0,\mathbf{r},\,\mathbf{y};z^0,\mathbf{z},\,\mathbf{z}) \\ &\quad+\int d^3\mathbf{r}\,K_1(y^0,\mathbf{y};x^0,\mathbf{r})\,K_2(x^0,\mathbf{r},\,\mathbf{x};z^0,\mathbf{z},\,\mathbf{z})\Big]. \end{aligned} \tag{3.10}$$

Note that, due to the boundary condition of the propagators, the first term on the right hand side (r.h.s.) of the second equation survives only at $x^0 > y^0 > z^0$, whereas the second term is non-vanishing only at $y^0 > x^0 > z^0$. The first term represents the case where a $t\bar{t}$ pair is created at time $t = z^0$, propagates while forming the toponium resonance until $t = y^0$, when the anti-top quark decays via the electroweak (EW) interaction, and the remaining top quark propagates freely until it decays at $t = x^0$. The top quark decays before the anti-top quark in the latter term. It can be checked that the eq.(3.10) gives the correct non-relativistic limit of the relativistic three-point function for $V(r) = 0$.

By taking the Fourier transform of (3.10), we obtain the three-point function in momentum space as

$$\tilde{K}(p_t,p_{\bar{t}})_{\alpha\gamma,\delta\beta}=\left(\frac{1+\gamma^0}{2}\right)_{\alpha\gamma}\left(\frac{1-\gamma^0}{2}\right)_{\delta\beta}\tilde{G}(\mathbf{p};E)\,[D(p_t)+D(p_{\bar{t}})] \tag{3.11}$$

where $D(p)$ represents the non-relativistic propagator

$$iD(p)=\frac{i}{p^0-m_t-\mathbf{p}^2/2m_t+i\Gamma_t/2}. \tag{3.12}$$

We set the 4-momentum of t and $\bar{t}$, respectively, as $p_t = (p^0,\mathbf{p})$, $p_{\bar{t}} = (\bar{p}^0,-\mathbf{p})$ with $p^0+\bar{p}^0 = 2m_t+E$. Here, we introduced the top quark width in place of the $i\epsilon$ prescription in eq. (3.4). The Green's function $\tilde{G}(\mathbf{p};E)$ is defined as the Fourier transform of the toponium Green's function $G(\mathbf{x};E)$, which satisfies the time-independent inhomogeneous Schrödinger equation:

$$\left\{-\frac{\Delta}{m_t}+V(r)-\left(E+i\frac{\Gamma_\Theta}{2}\right)\right\}G(\mathbf{x};E)=\delta^3(\mathbf{x}), \tag{3.13}$$

$$\tilde{G}(\mathbf{p};E)=\int d^3\mathbf{x}\,e^{-i\mathbf{p}\cdot\mathbf{x}}\,G(\mathbf{x};E). \tag{3.14}$$

Here we introduced in the Schrödinger equation Γ_Θ, the decay width of the toponium, to implement its unstableness [16]. The width Γ_Θ of the two-particle state is, in general, a function of momentum:

$$\Gamma_\Theta = \Gamma_\Theta(E, \mathbf{p}). \tag{3.15}$$

We give an extensive discussion on the effect of Γ_Θ in the next section.

We note that by using the three-point function (3.11), we can compute the helicity amplitudes for the process $e^+e^- \to bW^+\bar{b}W^-$: the T-matrix element in momentum space is written explicitly as

$$\begin{aligned} T_{fi} &= -\frac{g_W}{\sqrt{2}} V_{tb}^* [\bar{u}_b \gamma^\mu \frac{1-\gamma_5}{2}]_\alpha \epsilon^*_{\mu W^+} \cdot \frac{g_W}{\sqrt{2}} V_{tb} [\gamma^\nu \frac{1-\gamma_5}{2} v_{\bar{b}}]_\beta \epsilon^*_{\nu W^-} \\ &\times \left(\frac{1+\gamma^0}{2}\right)_{\alpha\gamma} \left(\frac{1-\gamma_0}{2}\right)_{\delta\beta} \tilde{G}(\mathbf{p}; E) \left[D(p_t) + D(p_{\bar{t}})\right] \\ &\times \sum_{V=\gamma,Z} [v_V^t \gamma^\rho + a_V^t \gamma^\rho \gamma_5]_{\gamma\delta} \frac{1}{q^2 - m_V^2 + i m_V \Gamma_V} \bar{v}_{e^+} (v_V^e \gamma_\rho + a_V^e \gamma_\rho \gamma_5) u_{e^-}, \end{aligned} \tag{3.16}$$

which is obtained by inserting (2.5), (2.6) and (3.11) into (2.4). It is also straightforward [17] to include the subsequent W decays in realistic applications [12]. Correlations among the decay products that are expected for heavy top quark decays [2,18] can hence be incorporated naturally along with the enhancement factor due to the Green's function $\tilde{G}(\mathbf{p}; E)$. It should be noted that the QCD correction factor $\tilde{G}(\mathbf{p}; E)$ not only depends on the total energy $\sqrt{s} = 2m_t + E$ but also on the three momentum $\mathbf{p}$ of the bW system in the collision c.m. frame. In this paper, only the S-wave component of the Green's function is evaluated exactly since the P-wave amplitudes from the top quark axial-vector coupling is absent for the non-relativistic t and $\bar{t}$ wave functions in (3.11). A detailed study of the QCD corrections to the P-wave amplitudes [19] will be reported elsewhere [20].

The differential cross section is obtained from the above T matrix elements as

$$d\sigma = \frac{1}{2s} \overline{\Sigma} |T_{fi}|^2 d\Phi_4(bW^+\bar{b}W^-), \tag{3.17}$$

where $\overline{\Sigma}$ denotes summing over final particle helicities and the color degrees of freedom and averaging over initial $e^\pm$ helicities, and $d\Phi_4(bW^+\bar{b}W^-)$ denotes the Lorentz invariant 4-body phase space factor. Integration over the final state phase space of the differential cross section (3.17) gives the total cross section at a given c.m. energy, $\sqrt{s} = 2m_t + E$. On the other hand, the non-relativistic Hamiltonian formalism enables us to derive the

total cross section directly from the Green's function. The optical theorem relates the top quark contribution to the total cross section and the photon vacuum polarization tensor $\Pi_t^{\mu\nu}(q)$ as (see Fig. 3)

$$\sigma_{tot}(e^+e^- \to t\bar{t}) = \frac{4\pi\alpha}{s^2}(-g_{\mu\nu})\, Im\, \Pi_t^{\mu\nu}(q), \tag{3.18}$$

where we have included only the photon ($V = \gamma$) as an intermediate vector boson for brevity. Its four-momentum is set as $q = (2m_t + E, \mathbf{0})$ in the c.m. frame. It is straightforward to obtain $\Pi_t^{\mu\nu}(q)$ by following steps similar to those that lead to the three-point function $\tilde{K}(p_t, \bar{p}_t)$ in terms of $\tilde{G}(\mathbf{p}; E)$ in (3.11). We find

$$\begin{aligned} \Pi_t^{\mu\nu}(q) &= 3 \cdot \left(i\frac{2}{3}e\right)^2 tr\left[\gamma^\mu \frac{1+\gamma^0}{2}\gamma^\nu \frac{1-\gamma^0}{2}\right] G(\mathbf{x}=0; E) \\ &= \frac{32\pi\alpha}{3}(q^\mu q^\nu/s - g^{\mu\nu})\, G(\mathbf{x}=0; E). \end{aligned} \tag{3.19}$$

Inserting (3.19) into (3.18), we obtain

$$\sigma_{tot}(e^+e^- \to t\bar{t}) = \frac{128\pi^2\alpha^2}{3s^2}\, Im\, G(\mathbf{x}=0; E). \tag{3.20}$$

Therefore, the total cross section is obtained from the imaginary part of the Green's function at the origin [5,9], $Im\, G(\mathbf{x} = 0; E)$, as well as by integrating over the differential cross section (3.17) which is enhanced by the square of its Fourier transform $\tilde{G}(\mathbf{p}; E)$. Their equality should be guaranteed by the unitarity of the toponium Green's function, which is the subject of the following section.

4 Effect of the Running Decay Width

We try to clarify the effect of the running of the toponium width Γ_Θ in this section. In fact, it gives a considerable effect to the observable cross sections in the threshold region. We first explain, in subsection 4.a, the motivation for including the running of the decay widths in our calculation. The off-shell behavior of the top quark running width $\Gamma_t(p_t^2)$, which is intimately related to the toponium running width $\Gamma_\Theta(E, \mathbf{p})$, is discussed in subsection 4.b from the viewpoint of the electroweak gauge invariance. The toponium width Γ_Θ is determined in subsection 4.c, followed by the discussion on its physical implications in subsection 4.d. We present our numerical method to evaluate the Green's function in the presence of the running width in the Appendices. All the examples presented in this section adopt a purely Coulombic potential with a fixed strong coupling constant so that they can be compared with the known analytic results whenever available. A more realistic QCD potential will be introduced in the next section.

4.a Need for the Inclusion of the Running Effect

By using the formulas derived in the previous section, one can check the unitarity relation between the differential cross section and the total cross section. It turns out, however, that there would be a considerable discrepancy in the unitarity relation had we used twice the constant on-shell decay width $\Gamma_\Theta = 2\Gamma_t(m_t^2)$, for the toponium width, in evaluating the Green's function.

In Fig. 4, we show the total $t\bar{t}$ pair production cross section as a function of the binding energy $E = \sqrt{s} - 2m_t$, for the purely Coulombic potential ($V = -C_F\alpha_s/r$) with a fixed coupling constant α_s [21] for $m_t = 150$ GeV. We switched off the Z contribution in the e^+e^- annihilation channel for simplicity. The dashed line is obtained directly from the total cross section formula (3.20) whereas the dotted line is obtained by integrating over the differential cross section formula (3.17), both with the constant top-quark on-shell width. The discrepancy is at the level of 7–10% at $E \gtrsim 0$, 12% at the peak of the cross section, and it exceeds the 50% level at $E \lesssim -5$ GeV. The integral of the differential cross section is smaller than the naive prediction of the optical theorem (3.20), partly because of the small available phase space at $E \lesssim 0$ and partly because of the broadness of the top-quark Breit-Wigner resonance shape. We find that the discrepancy between the two results is even larger for smaller m_t values. We should properly take into account the running of the decay widths to restore unitarity [22].

In the framework of our non-relativistic approximation, we find that unitarity is restored only when order $\mathbf{p}^2/m_t^2$ corrections to the width Γ_Θ are included. This may be seen from the unitarity relation between the Green's functions defined by eqs. (3.13) and (3.14) in the last section:

$$2\,Im\,G(\mathbf{x}=0;E) = \int \tfrac{d^3\mathbf{p}}{(2\pi)^3}\,|\tilde{G}(\mathbf{p};E)|^2\,\Gamma_\Theta, \tag{4.1}$$

which can be shown directly by using the definition

$$G(\mathbf{x};E) = \langle \mathbf{x}\,|\,\frac{-1}{E-H+i\Gamma_\Theta/2}\,|\,\mathbf{x}'=0\,\rangle\,, \tag{4.2}$$

and the operator identity

$$2Im\frac{-1}{E-H+i\Gamma_\Theta/2} = \frac{-1}{E-H-i\Gamma_\Theta/2}\cdot\Gamma_\Theta\cdot\frac{-1}{E-H+i\Gamma_\Theta/2}\,. \tag{4.3}$$

The relation (4.1) then follows by taking the $\mathbf{x}=\mathbf{x}'=0$ matrix element and by inserting the complete set of the momentum eigenstates. It should be noted that the identity (4.1) holds exactly even when Γ_Θ depends on E and $\mathbf{p} = -i\nabla$. We see the explicit appearance

of the 'toponium' width Γ_Θ on the r.h.s. of (4.1), rather than just in the denominator of $\tilde{G}(\mathrm{p}; E)$. This is related to the phase space volume in the differential cross section formula eq. (3.17). It is, therefore, important to keep the order p^2/m_t^2 terms in Γ_Θ in the evaluation of $Im\, G(0; E)$ to preserve unitarity. After all, Γ_Θ is the only physical quantity carrying the information of the $t\bar{t}$ decay process when we apply the optical theorem (3.20) to evaluate the total cross section.

4.b Determination of the Top-Quark Running Width $\Gamma_t(p_t^2)$

In this subsection, we study the running width of the top-quark $\Gamma_t(p_t^2)$ whose off-shell behavior is found to determine essentially the physical toponium width in the next subsection. We discuss the general problem of determining the off-shell top quark width in view of its dependence on the electroweak gauge parameter.

The running width is obtained in the unitary gauge by replacing m_t^2 by $p_t^2 = s_t$ in the on-shell decay width formula:

$$\Gamma_t(s_t)|_{unitary} = \theta(s_t - m_W^2)\, \frac{G_F}{\sqrt{2}} \frac{\sqrt{s_t}}{8\pi} (s_t + 2m_W^2)(1 - \frac{m_W^2}{s_t})^2. \tag{4.4}$$

Throughout this section we assume a massless b quark and a stable W.

There is the subtlety here that the running of the effective top-quark width as defined from the imaginary part of the top-quark self-energy depends on our gauge choice in the electroweak sector. For example in the 't Hooft-Feynman gauge ($\xi_W = 1$), the running width behaves as [24]

$$\Gamma_t(s_t)|_{\xi_W=1} = \theta(s_t - m_W^2) \frac{G_F}{\sqrt{2}} \frac{\sqrt{s_t}}{8\pi} (m_t^2 + 2m_W^2)(1 - \frac{m_W^2}{s_t})^2. \tag{4.5}$$

The large s_t behavior of the top quark running width is now proportional to $s_t^{1/2}$ rather than $s_t^{3/2}$ of eq. (4.4), which may be regarded as representing the prediction of the longitudinal W Nambu-Goldstone boson equivalence theorem [25] in the limit $s_t \sim m_t^2 \gg m_W^2$. For instance, in the limit of vanishing gauge coupling $g_W \to 0$, the top quark decay width should be approximated by its decay into the b-quark and the charged Nambu-Goldstone boson, whose off-shell behavior may most naturally be expressed by eq. (4.5) with $m_W = 0$.

Qualitatively, both running widths decrease for top quark invariant mass $s_t < m_t^2$. The large discrepancy in the unitarity relation can be traced back to this off-shell behavior; when t and $\bar{t}$ are bound to form the toponium state, the invariant mass of each particle

is typically off-shell ($s_t < m_t^2$) and the effective width becomes smaller than the on-shell width $\Gamma_t(m_t^2)$.

However, quantitatively, the above gauge dependence of the running top-quark width is relevant in our non-relativistic approximation, since we should consistently take account of the order $\mathbf{p}^2/m_t^2$ corrections to the widths for the sake of unitarity. We will find in the next subsection that the shift in the invariant mass squared of the bW system, $s_t - m_t^2$, is indeed of this order. Hence, what is relevant to our approximation is the coefficient $\Gamma_t'(m_t^2)$ of the expansion

$$\Gamma_t(s_t) = \Gamma_t(m_t^2) + \Gamma_t'(m_t^2)(s_t - m_t^2) + O((s_t - m_t^2)^2). \tag{4.6}$$

The two expressions (4.4) and (4.5) for the relativistic running width then give

$$\Gamma_t'(m_t^2) = \frac{G_F m_t}{16\pi\sqrt{2}}(1 - \frac{m_W^2}{m_t^2})(3 + 3\frac{m_W^2}{m_t^2} + 6\frac{m_W^4}{m_t^4}) \quad \text{in the unitary gauge,} \tag{4.7}$$

$$= \frac{G_F m_t}{16\pi\sqrt{2}}(1 - \frac{m_W^2}{m_t^2})(1 + 5\frac{m_W^2}{m_t^2} + 6\frac{m_W^4}{m_t^4}) \quad \text{in the Feynman gauge,} \tag{4.8}$$

which differ by a factor of three in the relevant limit of $m_W^2/m_t^2 \to 0$. The running of the effective width around the pole $s_t = m_t^2$ is hence a factor of three larger in the unitary gauge than what is naively expected by the equivalence theorem in this limit.

The important point is that we are concerned with the determination of the physical quantities Γ_n, the widths of the resonances. The running top-quark width $\Gamma_t(s_t)$ is needed for the determination of the running toponium width $\Gamma_\Theta(E, \mathbf{p})$ and hence of the Γ_n's, because of our approximation ('the spectator quark model' [26]) that it is determined by the free decays of the constituent off-shell top quarks inside the toponium. Had we known the wave function of the toponium in an arbitrary gauge, its decay width should be obtained independent of the gauge.

In our non-relativistic formalism, we make the following substitutions for the off-shell top quark wave functions

$$\begin{aligned} \Sigma u_t \bar{u}_t &= m_t(\gamma^0 + 1), \\ \Sigma v_t \bar{v}_t &= m_t(\gamma^0 - 1), \end{aligned} \tag{4.9}$$

as can be seen from the two-particle propagator (3.11). In the next subsection, we find that the resulting invariant mass distribution of the bW system is consistent with the desired 'Feynman gauge' behavior.

4.c Determination of Γ_Θ

In this subsection, we determine the decay width of toponium Γ_Θ by performing the 4-body ($bW^+\bar{b}W^-$) phase space integral of the differential cross section explicity. We find that the toponium width as defined by this method is essentially twice the running top quark width evaluated at a specific off-shell point.

We start with the unitarity relation shown diagramatically in Fig. 5;

$$2\,Im\,T_{ii} = \overline{\Sigma}\int d\Phi_4(bW^+\bar{b}W^-)\;\mid T_{fi}\mid^2 . \tag{4.10}$$

We assume that the spin average of the initial e^+e^- state is taken on both sides. The l.h.s. is given in terms of the photon vacuum polarization, and is immediately evaluated as

$$2\,Im\,T_{ii} = \frac{256\pi^2\alpha^2}{3s}\,Im\,G(0;E). \tag{4.11}$$

On the r.h.s., the Fourier transfrom of the three-point function (3.11) appears in the T-matrix element eq. (3.16). We keep the relativistic kinematics in the intermediate steps, and at the end of the calculation we drop higher order terms in $\mathbf{p}^2/m_t^2$.

We first split the final 4-body phase space as

$$d\Phi_4(bW^+\bar{b}W^-) = \frac{d^4p}{(2\pi)^4}\frac{d^4\bar{p}}{(2\pi)^4}(2\pi)^4\delta^4(p+\bar{p}-q)d\Phi_2(bW^+)d\Phi_2(\bar{b}W^-), \tag{4.12}$$

where $d\Phi_2$ denotes the 2-body phase space with the momentum constraint $p_b + p_{W+} = p$ and $p_{\bar{b}} + p_{W-} = \bar{p}$. Then we perform the two 2-body bW phase space integrations $\int d\Phi_2(bW^+)d\Phi_2(\bar{b}W^-)$. We note that the running width $\Gamma_t(s_t)$ appears as a result of the integration of $|T_{fi}|^2$. In fact, the spinor structure associated with the process $t \to bW^+$ after the bW phase space integration reads

$$\sigma(\not{p}_t) \equiv \int d\Phi_2(bW^+)\sum_{bW^+\,spin}\mathcal{M}(t\to bW^+)\,\mathcal{M}(t\to bW^+)^\dagger \tag{4.13}$$

$$= \frac{\Gamma_t(s_t)}{\sqrt{s_t}}\;\not{p}_t(1-\gamma_5), \tag{4.14}$$

where the truncated transition spinor $\mathcal{M}(t\to bW^+)$ is defined as

$$\mathcal{M}(t\to bW^+) = \left[\left(i\frac{g_W}{\sqrt{2}}\right)\epsilon^*_\mu(p_{W+})\,\bar{u}_b(p_b)\,\gamma^\mu\,\frac{1-\gamma_5}{2}\right]^\dagger . \tag{4.15}$$

It should be noted that the running top-quark width that appears in eq. (4.14) by using the above free tbW coupling and the physical W wave function is the unitary gauge width (4.4).

Substituting $\sigma(\not{p})$ and $\sigma(\not{\bar{p}})$ in $|T_{fi}|^2$ and taking the trace of the γ-matrices, we find

$$\Sigma \int d\Phi_4(bW^+\bar{b}W^-) \mid T_{fi} \mid^2$$
$$= \frac{128\pi^2\alpha^2 m_t^2}{3s} \int \frac{d^4p}{(2\pi)^4}\frac{d^4\bar{p}}{(2\pi)^4}(2\pi)^4\delta^4(p+\bar{p}-q)|\tilde{G}(\mathrm{p};E)|^2$$
$$\times |D(p)+D(\bar{p})|^2 \frac{\Gamma_t(p^2)}{\sqrt{p^2}}\frac{\Gamma_t(\bar{p}^2)}{\sqrt{\bar{p}^2}}\, F\Big(\frac{p}{m_t},\frac{\bar{p}}{m_t}\Big). \tag{4.16}$$

The function F reflects the spin structure of $t\bar{t}$, and is given by

$$F(n,\bar{n}) = n^0\bar{n}^0 + |\mathrm{n}||\bar{\mathrm{n}}|\cos^2\theta. \tag{4.17}$$

Here, θ represents the polar angle of the top quark in the c.m. frame. For non-relativistic t and $\bar{t}$, $F\Big(\frac{p}{m_t},\frac{\bar{p}}{m_t}\Big) \simeq 1$. The integrand on the r.h.s. of (4.16) shows the momentum distributions of t and $\bar{t}$ inside the toponium.

At this stage, we find that the invariant mass distributions of t and $\bar{t}$ are of the Breit-Wigner type, and the off-shell distribution is essentially governed by the factor $\Gamma_t(s_t)/\sqrt{s_t}$, which behaves as s_t at $s_t \gg m_t^2$. This should be compared with that of the free relativistic calculation without strong interactions for the corresponding diagram, whose off-shell behavior is governed by the factor $\sqrt{s_t}\,\Gamma_t(s_t)$, which behaves as s_t^2: the off-shell behavior becomes smoother, as $\sim s_t$, only after adding other diagrams which contribute as the non-resonant background continuum. By using the non-relativistic form of the top quark wavefunctions (4.9), we find that the contribution of the t and $\bar{t}$ intermediate states (see Fig. 1) gives the off-shell behavior consistent with the naive expectation from the equivalence theorem [25] in the limit of $s_t,\ m_t^2 \gg m_W^2$.

We now perform the time component integration $\int \frac{dp^0}{(2\pi)}\frac{d\bar{p}^0}{(2\pi)}(2\pi)\delta(p^0+\bar{p}^0-q^0)$ in eq. (4.16). One can verify that the factor $|D(p)+D(\bar{p})|^2$ in the integrand on the r.h.s. exhibits sharp peaks when either t or $\bar{t}$ becomes on-shell, i.e. $p^2 = m_t^2$ or $\bar{p}^2 = m_t^2$, and essentially vanishes elsewhere. Meanwhile other factors behave quite mildly when $p^0(\bar{p}^0)$ varies within the peak regions. Thus, we obtain a very good approximation of the integral by first evaluating the integrand when $p^0(\bar{p}^0)$ is at either of the peaks, then by fixing all factors but $|D(p)+D(\bar{p})|^2$ as constants. Using

$$\int \frac{dp^0}{(2\pi)}\frac{d\bar{p}^0}{(2\pi)}(2\pi)\delta(p^0+\bar{p}^0-q^0)\,|D(p)+D(\bar{p})|^2 = \frac{2}{\Gamma_t(m_t^2)}, \tag{4.18}$$

we find

$$\int d\Phi_4(bW^+\bar{b}W^-) \mid T_{if} \mid^2 = \frac{128\pi^2\alpha^2}{3s}\int \frac{d^3\mathrm{p}}{(2\pi)^3}|\tilde{G}(\mathrm{p};E)|^2\Gamma_{\mathrm{eff}}(E,\mathrm{p}), \tag{4.19}$$

where we defined the effective width $\Gamma_{\rm eff}$ as

$$\Gamma_{\rm eff}(E,\mathbf{p}) \equiv 2\frac{m_t}{\sqrt{k_1^2}}\Gamma_t(k_1^2)\ F\left(\tfrac{k_1}{m_t},\tfrac{k_2}{m_t}\right). \tag{4.20}$$

When $t\,(\bar{t})$ is on-shell, $\bar{t}\,(t)$ becomes off-shell due to the momentum conservation; k_2 denotes the four-momentum of the one which is on-shell whereas k_1 denotes that of the off-shell particle for given E and $\mathbf{p}$. Namely,

$$k_2^0=\sqrt{m_t^2+\mathbf{p}^2},\quad k_1^0=2m_t+E-k_2^0,\quad \mathbf{k}_2=-\mathbf{k}_1=\mathbf{p}. \tag{4.21}$$

Comparing (4.19) with (4.11), we find that $\Gamma_{\rm eff}$ is identified with the toponium width Γ_Θ via the unitarity relation of the Green's function (4.1). This allows us to express analytically the running decay width of toponium. By retaining only the terms up to the order E/m_t and $\mathbf{p}^2/m_t^2$ in (4.20), we find after the angular average

$$\Gamma_\Theta(E,\mathbf{p}) = \frac{G_F}{\sqrt{2}}\frac{m_t^3}{4\pi}\left[\eta_1-\eta_2\frac{\mathbf{p}^2}{m_t^2}\right] \tag{4.22}$$

with

$$\eta_1 = (1-3w^2+2w^3)+(3+3w^2-6w^3)\frac{E}{m_t}, \tag{4.23}$$

$$\eta_2 = \frac{5}{3}+7w^2-\frac{26}{3}w^3, \tag{4.24}$$

and

$$w=\frac{m_W^2}{m_t^2}. \tag{4.25}$$

This approximates (4.20) to the few percent level in the region of $(E,\mathbf{p})$ that is relevant to our calculation ($|E|\lesssim 10$ GeV, $|\mathbf{p}|\lesssim 30$ GeV). The momentum dependence of the running toponium width is shown in Fig. 6 at three reference energies, $E=-2,\ 0,\ +2$ GeV. At $(E,|\mathbf{p}|)=(0,\ 0)$ and $(2,\ 17.3)$ GeV, both t and $\bar{t}$ can be on-shell and $\Gamma_\Theta\simeq 2\Gamma_t(m_t^2)$ [27]. At each energy E, the toponium width Γ_Θ is found to decrease with increasing internal momentum $|\mathbf{p}|$.

Let us examine the physical meaning of $\Gamma_\Theta(E,\mathbf{p})$ as shown above. At first, one might be tempted to identify $\Gamma_\Theta(E,\mathbf{p})$ with $\Gamma_t(p_t^2)+\Gamma_t(p_{\bar{t}}^2)$, as the decay width of Γ_Θ is almost saturated by the weak decays of t and $\bar{t}$. However, the Schrödinger equation (3.13) implies that Γ_Θ should depend only on E and $\mathbf{p}$ in order for the toponium to be regarded as a non-relativistic resonance state composed of t and $\bar{t}$, while these variables do not

determine p_t^2 and $p_{\bar{t}}^2$ completely. In a sense, the toponium width Γ_Θ should be averaged over the various configurations of t and $\bar{t}$ inside the toponium. We find that the dominant configuration is such that either one of the constituents is on-shell. After the appropriate averaging, we obtained (4.22). More intuitively, we may interpret the essential result

$$\Gamma_\Theta(E, \mathrm{p}) \simeq 2\frac{m_t}{\sqrt{k_1^2}}\Gamma_t(k_1^2) \tag{4.26}$$

as the sum of the decay width of the constituent which decays first, since typically the off-shell constituent would decay faster than the on-shell constituent.

4.d Physical Implications

In this subsection, we discuss physical consequences of the running of Γ_Θ which we have evaluated in detail above.

We start by reminding the readers of the relevant physical quantities in our problem. One of most concern is the determination of the positions of the poles of the Green's function $G(\mathrm{x}; E)$ in the complex $E-$plane:

$$G(\mathrm{x}; E) \simeq -\sum_n \frac{\psi_n(\mathrm{x})\psi_n^*(0)}{E - E_n + i\Gamma_n/2}. \tag{4.27}$$

Here $\psi_n(\mathrm{x})$ represents the wave function of the n-th resonance state. The position of the poles, $E_n - i\Gamma_n/2$, are physical quantities, which may manifest themselves as the positions and the widths of the resonance peaks. In particular the widths of the resonances are relevant to the peak shapes, and are affected by our introduction of the running of Γ_Θ. We would like to know its effect and its physical implications.

Let us first consider the case where the potential is switched off, $V(r) = 0$, at energies above the threshold, $E > 0$. In this case, the momentum distribution of $t\bar{t}$ will have a peak when both t and $\bar{t}$ become on-shell. The magnitude of their momenta $|\mathrm{p}|$ is then typically fixed at this configuration once E is given ($|\mathrm{p}| \sim \sqrt{m_t E}$) so that the running width $\Gamma_\Theta(E, \mathrm{p})$ is essentially determined there. Since both t and $\bar{t}$ are on-shell, $k_1^2 = m_t^2$ and $k_2^2 = m_t^2$, this gives $\Gamma_\Theta(E, \mathrm{p}) \simeq 2\Gamma_t(m_t^2)$. Now let us switch on the attractive potential $V(r) < 0$. The kinetic energy of the $t\bar{t}$ system is now *increased* compared to that of the $V(r) = 0$ case, due to the binding energy; see Fig. 7. The relative momentum $2|\mathrm{p}|$ between t and $\bar{t}$ should hence be increased. Consequently, the invariant mass of the top-quark would be typically *smaller* than its on-shell mass under the influence of an attractive potential.

For our case with $V(r) < 0$, we notice a considerable reduction of Γ_Θ as compared to $2\Gamma_t(m_t^2)$ in the region of (E, p) where $|\tilde{G}(\mathrm{p}; E)|^2$ is large, as can be seen from Fig. 6 and Fig. 8. Shown in Fig. 8 are the momentum distribution $4\pi \mathrm{p}^2 |\tilde{G}(\mathrm{p}; E)|^2$ of the final bW system for $m_t = 150$ GeV at the three energies $E = -2$, 0, $+2$ GeV just as in Fig. 6. Also shown by the dashed line is the momentum distribution at $E = 2$ GeV in the zero binding limit. We can see clearly that the peak of $\mathrm{p}^2 |\tilde{G}(\mathrm{p}; E)|^2$ is shifted to larger $|\mathrm{p}|$ as compared with the $V(r) = 0$ case. For instance at $E = +2$ GeV, $|\mathrm{p}| = 17.3$ GeV if both t-quarks are on-shell. However, for $V(r) < 0$, the peak occurs at a considerably higher momentum, $|\mathrm{p}| \sim 20$ GeV, and hence one of the top quarks should be typically off-shell even above the threshold;

$$k_1^2 \lesssim m_t^2 \quad \text{and} \quad k_2^2 = m_t^2. \tag{4.28}$$

The reduction of the toponium width is expected to be even more significant for $E < 0$, where one of the top quarks is forced to become off-shell kinematically; see the $E = -2$ GeV curve in Fig. 6. The toponium width Γ_n is hence expected to be smaller than $2\Gamma_t(m_t^2)$ at all energies where our non-relativistic approximation is valid.

For clarity, let us again emphasize the main physical implications of introducing the running toponium width. If we regard the toponium formed as a dynamical system composed of t and $\bar{t}$, its kinetic energy is increased by an amount equal to the binding energy. The invariant masses of t and $\bar{t}$ decrease correspondingly. This effect renders the widths of the resonances, Γ_n, smaller than $2\Gamma_t(m_t^2)$ due to the running of Γ_t. Moreover, the amount of the increase in the kinetic energy differs for various resonance states, as their wave functions have different shapes in the potential $V(r)$. Hence, the Γ_n's will have different values for different n. We may incorporate these effects into the Green's function $G(\mathrm{x}; E)$ by solving the Schrödinger equation (3.13) with the running width $\Gamma_\Theta(E, \mathrm{p})$.

We can now return to Fig. 4 and explain it fully. The overall feature is that the cross section calculated with the running widths (σ_R) has a sharp peak compared to those with constant widths (σ_{C1} and σ_{C2}). This reflects the reduction of the resonance width. More concrete aspects can be understood by referring to the expression

$$\sigma_{TOT} = \frac{64\pi^2\alpha^2}{3s^2} \int \frac{d^3\mathrm{p}}{(2\pi)^3} |\tilde{G}(\mathrm{p}; E)|^2 \, \Gamma_\Theta(E, \mathrm{p}). \tag{4.29}$$

From the derivation of Γ_Θ, we find that each curve corresponds to a different set of choices whether we use the running width $\Gamma_\Theta = \Gamma_\Theta(E, \mathrm{p})$ or the constant width $\Gamma_\Theta = 2\Gamma_t(m_t^2)$ in evaluating $\tilde{G}(\mathrm{p}; E)$ and Γ_Θ, which is summarized in Table 1. The widths of the resonance states, Γ_n, are relevant in $\tilde{G}(\mathrm{p}; E)$ only at $E \simeq E_n$, since it is the Fourier

transform of $G(\mathbf{x};E)$ given by (4.27). This explains why σ_{C2} approximates σ_R below the first resonance, where the running width effect is important only in the Γ_Θ term of eq. (4.29) which represents appropriate phase space suppression. At the peak of the total cross section, σ_{C1} and σ_{C2} both fall short of σ_R, because the peak height is proportional to Γ_n^{-1}. σ_{C2} is smallest since it incorporates the phase space suppression correctly by performing the final state integration explicitly while neglecting the enhancement due to the smaller toponium width. σ_{C1} gives a better result simply because the double errors in this approximation tend to cancel. In the continuum region which consists of many resonances, σ_R is larger than σ_{C2} since Γ_n enters the denominator of $\tilde{G}(\mathbf{p};E)$. The original constant width approximation σ_{C1} [5] turns out to give a reasonable approximation in this region ($E > 0$) simply because of cancellation. These qualitative trends are common for the realistic confining potential and the non-confining Coulombic potential studied in this section even though the latter has a continuum wave function above the threshold.

It is useful here to compare our result with the traditional heavy quarkonium production cross section formula [8,13]:

$$\sigma_{TOT} = \sum_n 12\pi(\frac{M_n^2}{s})\frac{\Gamma_{ee}\Gamma_n}{(s-M_n^2)^2+(M_n\Gamma_n)^2} + \sigma_{CONT}. \tag{4.30}$$

where σ_{CONT} represents typically the one-loop corrected heavy quark pair production cross section in perturbative QCD [28]. It has been shown [10] that we can replace σ_{CONT} by summation over many resonance states above the $t\bar{t}$ threshold. We can hence express the total cross section as

$$\sigma_{TOT} = \sum_n 12\pi(\frac{M_n^2}{s})\frac{\Gamma_{ee}\Gamma_n}{(s-M_n^2)^2+(M_n\Gamma_n)^2}, \tag{4.31}$$

where the summation over the resonances is taken at all energies. Now, for simplicity, we restrict ourselves to the photon exchange contribution only and find

$$\Gamma_{ee} = 16\pi\alpha^2 e_q^2|\psi_n(0)|^2/M_n^2. \tag{4.32}$$

Substituting eq. (4.32) into eq. (4.31), we obtain

$$\sigma_{TOT} \simeq \frac{96\pi^2\alpha^2 e_q^2}{s^2}\sum_n \frac{\Gamma_n/2}{(E-E_n)^2+(\Gamma_n/2)^2}\psi_n(0)\psi_n^*(0), \tag{4.33}$$

where we used the non-relativistic approximation $s - M_n^2 \simeq 2\sqrt{s}(E - E_n)$ with $E_n = M_n - 2m_t$. Eq. (4.33) can be cast into the form

$$\begin{aligned}\sigma_{TOT} &\simeq \frac{96\pi^2\alpha^2 e_q^2}{s^2}\cdot Im\left[\sum_n \frac{-\psi_n(0)\psi_n^*(0)}{E-E_n+i\Gamma_n/2}\right] \\ &= \frac{96\pi^2\alpha^2 e_q^2}{s^2}\cdot Im\, G(0;E),\end{aligned} \tag{4.34}$$

which is essentially the expression as proposed by Fadin and Khoze [5]. Now if we take the resonance width to be $\Gamma_n = 2\Gamma_t(m_t^2)$, which is common to all the resonance states, and if $\psi_n(\mathbf{x})$ is the solution of the Schrödinger equation

$$H\psi_n(\mathbf{x}) \equiv \left[\frac{\mathbf{p}^2}{m_t} + V(r)\right]\psi_n(\mathbf{x}) = E_n\psi_n(\mathbf{x}), \tag{4.35}$$

then $G(\mathbf{x}; E)$ is a solution of

$$[E - H + i\Gamma_t(m_t^2)]G_C(\mathbf{x}; E) = -\delta^3(\mathbf{x}). \tag{4.36}$$

This is exactly the defining equation of the Green's function as proposed by Strassler and Peskin [9]. Therefore, the traditional approach [8,13] of calculating each Schrödinger wave-function from eq. (4.35) and the Green's function method [5,9] that solves eq. (4.36) give exactly the same results when the widths are taken to be constant and common to all the resonances. Here, the Green's function method is merely a handy tool to sum over many resonance contributions.

Now, when the running of the onium width is taken into account, eq. (4.36) gets modified to

$$[E - H + i\Gamma_\Theta(E, \mathbf{p})/2]G_R(\mathbf{x}; E) = -\delta^3(\mathbf{x}), \tag{4.37}$$

which is the definition of our Green's function, eq. (3.13). In this case, we can no longer express the Green's function $G_R(\mathbf{x}; E)$ as a summation over the resonances whose wave functions satisfy the Schrödinger equation (4.35) since Γ_Θ depends, in general, on both E and $\mathbf{p}$.

Nevertheless, if we directly solve eq. (4.37), the Green's function $G_R(\mathbf{x}; E)$ is expected to inherit the pole structure of $G_C(\mathbf{x}; E)$, though the exact pole positions have to be modified by the introduction of the running width. It should be noted that, if we use the constant width, the residues, $|\psi_n(0)|^2$, and the real parts of the pole positions, M_n, are exactly the same as those obtained in the $\Gamma_t \to 0$ limit, since $|\psi_n(0)|^2$ and M_n are determined by the Schrödinger equation (4.35) which contains no width at all. Therefore, the width effect gives nontrivial physical consequences other than the smearing of multiple-resonance contributions when we take into account the running of the top-quark width.

5 The Potential

The non-relativistic QCD potential $V(r)$ describing the $t\bar{t}$ system can be written as the sum of a short-distance part and a long-distance part. The form of the short-distance

part is given by perturbation theory due to the asymptotic freedom of QCD, while the long-distance part has to be determined phenomenologically. We incorporate the two-loop perturbative QCD effects in our short-distance part of the potential. The overall form of the potential is determined by fitting to charmonium and bottomonium data.

The short-distance potential $V_P(r)$ is calculated reliably in the perturbative QCD. In the next-to-leading order, the interquark potential can be written as [29,30,31]

$$V_P(r) = -\frac{C_F}{r}\alpha_s(\mu_1)_{\overline{\rm MS}} \tag{5.1}$$

where the coupling, α_s, is renormalized by the modified minimal subtraction ($\overline{\rm MS}$) scheme and where we have made a choice of the renormalization scale [32]

$$\mu_1 = \frac{1}{r}\exp\left(-\frac{A(r)}{b_0}\right) \tag{5.2}$$

with

$$b_0 = \frac{11}{6}C_A - \frac{2}{3}n_f T_F, \tag{5.3}$$

$$A(r) = b_0\gamma_E + \frac{31}{37}C_A + \frac{2}{3}T_F\sum_{q=1}^{n_f}[\gamma_E + \log(m_q r) - {\rm Ei}(-e^{5/6}m_q r)]. \tag{5.4}$$

Here $\gamma_E = 0.5772...$ is Euler's constant; $T_F = 1/2$, $C_F = 4/3$ and $C_A = 3$ are color factors; n_f is the number of quark flavors and ${\rm Ei}(-x)$ is the exponential integral

$${\rm Ei}(-x) = -\int_x^\infty \frac{dt}{t}e^{-t}, \tag{5.5}$$

which parametrizes accurately the quark mass dependence of the perturbative potential [31]. In the massless quark limit, the next-to-leading order correction factor $A(r)$ reduces to the well-known result [30,33]

$$A(r) \to b_0\gamma_E + \frac{31}{37}C_A - \frac{5}{9}n_f T_F \quad (\text{as } m_q r \to 0). \tag{5.6}$$

It should be stressed, however, that the charm and bottom quark masses cannot be neglected at distances

$$r m_q \sim 1. \tag{5.7}$$

The running coupling constant $\alpha_s(\mu)$ is fixed by the μ-independent QCD scale parameter

$$\Lambda_{\overline{\rm MS}}^{(n_f)} = \mu\,\exp\left\{-\frac{\pi}{b_0\alpha_s(\mu)} + \frac{b_1}{b_0^2}\log\left[\frac{2}{b_0}\left(\frac{\pi}{\alpha_s(\mu)} + \frac{b_1}{b_0}\right)\right]\right\} \tag{5.8}$$

with

$$b_1 = \frac{17}{12}C_A^2 - \frac{5}{6}C_A n_f T_F - \frac{1}{2}C_F n_f T_F, \tag{5.9}$$

which can easily be solved iteratively.

The contribution of a heavy top quark loop to the toponium potential can always be neglected due to the asymptotic freedom of QCD [34] and the decoupling theorem [35], because the top quark mass is much larger than the inverse of the toponium size of order $\alpha_s m_t$ for $\alpha_s \ll 1$. In the zero width approximation for toponium, the bottom quark loop contribution to the quarkonium potential can also be neglected for $m_t \lesssim 100$ GeV [8]. Therefore, the effective four flavor ($n_f = 4$) theory with $m_u = m_d = m_s = 0$ and $m_c = 1.5$ GeV (fixed) can give a good description of the short distance potential for a wide range of inter-quark distance ($r \gtrsim 1/m_b$). When the top quark is heavier and the decay width of the $t\bar{t}$ system is as high as a few GeV, the short distance potential should be more accurately described by the effective five flavor ($n_f = 5$) theory. Thus, we fix $n_f = 5$ for the QCD potential throughout the paper and retain the charm and bottom quark finite masses. The next-to-leading order correction factor $A(r)$ in eq. (5.4) is then

$$A(r) = b_0\gamma_E + \frac{31}{37}C_A + \frac{2}{3}T_F\left[-\frac{5}{2} + \gamma_E + \log(m_c r) - \mathrm{Ei}(-e^{5/6}m_c r)\right.$$

$$\left. + \gamma_E + \log(m_b r) - \mathrm{Ei}(-e^{5/6}m_b r)\right] \tag{5.10}$$

which is obtained by setting $n_f = 5$ in b_0 and $m_u = m_d = m_s = 0$. We set $m_c = 1.5$ GeV and $m_b = 5$ GeV, whose values are fixed throughout the paper irrespective of the values of m_c and m_b that appear in the fitting of the charmonium and bottomonium data.

The μ-independent QCD scale parameter $\Lambda_{\overline{\mathrm{MS}}}^{(n_f)}$ for $n_f = 4$ and $n_f = 5$ theories are related through the matching condition [36]

$$\alpha_s^{(4)}(\mu = m_b)_{\overline{\mathrm{MS}}} = \alpha_s^{(5)}(\mu = m_b)_{\overline{\mathrm{MS}}}. \tag{5.11}$$

Since we work in the $n_f = 5$ theory, the perturbative QCD potential is completely determined once $\Lambda_{\overline{\mathrm{MS}}}^{(5)}$ is fixed. Since the definition of the $\Lambda_{\overline{\mathrm{MS}}}^{(n_f)}$ parameters are somewhat arbitrary [37], we use the magnitude of the $\overline{\mathrm{MS}}$ coupling constant at $\mu = m_Z$ (=91.17 GeV), $\alpha_s(m_Z)_{\overline{\mathrm{MS}}}$, to parametrize the strength of the QCD interactions. The value of $\Lambda_{\overline{\mathrm{MS}}}^{(5)}$ in our definition is then obtained directly from eq. (5.8). The corresponding $\Lambda_{\overline{\mathrm{MS}}}^{(4)}$ value is obtained from the matching condition (5.11) at $m_b = 5$ GeV. The values of $\Lambda_{\overline{\mathrm{MS}}}^{(4)}$ and $\Lambda_{\overline{\mathrm{MS}}}^{(5)}$ for $\alpha_s(m_Z)_{\overline{\mathrm{MS}}} = 0.10$ to 0.14 are given in Table 2.

While it is justified to neglect dynamical quark mass effects in the potential at small distances ($rm_q \ll 1$), they have to be taken into account at larger distances ($rm_q \sim 1$). In Fig. 9, we show distributions of $-C_F/rV_P(r) = 1/\alpha_s(\mu_1)_{\overline{\rm MS}}$ as functions of r for the massive $n_f = 5$ theory and the corresponding $n_f = 5$ and $n_f = 4$ massless quark theories for $\alpha_s(m_Z)_{\overline{\rm MS}} = 0.10$ and 0.12. For $r \ll 1/m_b$, the effective $n_f = 5$ (solid lines) and the massless $n_f = 5$ (dashed lines) theories agree with each other perfectly, showing that quark mass effects can be neglected at those distances ($r \lesssim 0.05$ GeV^{-1}). At these short distances $r \lesssim 0.05$ GeV^{-1}, the $n_f = 4$ theory deviates appreciably from the $n_f = 5$ theory and hence the $n_f = 5$ theory should be used in this region. On the other hand, for $r \gtrsim 0.2$ GeV^{-1} where most of the interesting charmonium and bottomonium data are sensitive, the $n_f = 5$ massless theory ($m_c = m_b = 0$) is incorrect since there the finite charm and bottom quark masses are non-negligible. Thus, in order to describe as accurately as possible the short distance potential for a wide range of inter-quark distance, we adopt the effective $n_f = 5$ theory with finite charm and bottom quark masses.

At intermediate and long distances, non-perturbative effects of QCD become more important. The inter heavy quark potential in the region

$$0.5 \text{ GeV}^{-1} \lesssim r \lesssim 5 \text{ GeV}^{-1} \tag{5.12}$$

is known [33] to be constrained well by the charmonium and bottomonium data, which is roughly consistent with the logarithmic potential of Quigg and Rosner [39]. At long distances, the potential may rise linearly reflecting the quark confinement. We therefore parametrize our phenomenological potential as follows:

$$\begin{aligned} V(r) &= V_P(r) && \text{at } r < r_0, \\ &= c_0 + c_1 \ln \tfrac{r}{r_0} e^{-r/r_1} + ar && \text{at } r > r_0. \end{aligned} \tag{5.13}$$

We require that the potential $V(r)$ and its first derivative $V'(r)$ be continuous at $r = r_0$:

$$c_0 = -ar_0 + V_P(r_0), \tag{5.14}$$

$$c_1 = r_0 e^{r_0/r_1}[-a + V_P'(r_0)]. \tag{5.15}$$

The above two conditions fix c_0 and c_1 in terms of the remaining three free parameters r_0, r_1 and a, for a given $\alpha_s(m_Z)_{\overline{\rm MS}}$ value. The derivative of the perturbative potential is given exactly by using the two-loop renormalization group equation as

$$\begin{aligned} V_P'(r) = &-\frac{V_P(r)}{r}\{1 - \frac{\alpha_s(\mu_1)_{\overline{\rm MS}}}{\pi} \\ &\times[b_0 + b_1\frac{\alpha_s(\mu_1)_{\overline{\rm MS}}}{\pi}](1 + \frac{2 - \exp(-e^{5/6}m_c r) - \exp(-e^{5/6}m_b r)}{3b_0})\}, \end{aligned} \tag{5.16}$$

where the scale $\mu_1(r)$ is given by eq. (5.2). It is worth noting here that the term multiplying the two-loop beta function factor $[b_0 + b_1\frac{\alpha_s}{\pi}]$ is unity at short distances $m_c r$, $m_b r \ll 1$, whereas in the long distance limit $m_c r$, $m_b r \gg 1$, it reduces to the factor

$$\frac{b_0 + \frac{2}{3}}{b_0}. \tag{5.17}$$

This is nothing but the ratio of the coefficient (5.3) of the effective three flavor theory, $b_0(n_f = 3) = b_0(n_f = 5) + \frac{2}{3}$, and that of our effective five flavor theory, exhibiting the decoupling of heavy quarks at long distances [40].

By varying the free parameters r_0, r_1 and a together with the constituent charm and bottom quark masses, m_c and m_b, this potential gives a good description of the properties of the bottomonium and charmonium data [38] for a range of fixed $\alpha_s(m_Z)_{\overline{\rm MS}}$ values. Note that the dynamical charm and bottom quark masses in the short distance part of the potential are fixed at $m_c = 1.5$ GeV and $m_b = 5$ GeV, respectively (see eq. (5.10)). The results of the χ^2 fit to data for a range of $\alpha_s(m_Z)_{\overline{\rm MS}}$ values are listed in Table 2. The overall χ^2 is found to be very stable to changes in $\alpha_s(m_Z)_{\overline{\rm MS}}$ for the range $0.10 \lesssim \alpha_s(m_Z)_{\overline{\rm MS}} \lesssim 0.14$. In fact, because of the steady changes of parameters with respect to $\alpha_s(m_Z)_{\overline{\rm MS}}$, the parameters of the QCD potential can be very well parametrized by a polynomial in $\alpha_s(m_Z)_{\overline{\rm MS}}$ in this range. The fitted values of the constituent charm and bottom quark masses are slightly low at $\alpha_s(m_Z)_{\overline{\rm MS}} = 0.10$ while they are a little too large at $\alpha_s(m_Z)_{\overline{\rm MS}} = 0.14$. The mass difference $m_b - m_c$ is almost independent of $\alpha_s(m_Z)_{\overline{\rm MS}}$. We note here, however, that a relatively small value $\alpha_s(m_Z)_{\overline{\rm MS}} \sim 0.105$ is inferred from the recent studies of the charmonium and bottomonium spectra in Lattice QCD [43].

In Fig. 10, we show by solid lines our resulting QCD motivated potential for $\alpha_s(m_Z)_{\overline{\rm MS}} = 0.10$, 0.11, 0.12 and 0.13. The optimal potential as obtained by our parametrization is found to be purely perturbative at $r \lesssim 0.2$ GeV^{-1} ($r_0 \sim 0.2$ GeV^{-1} in Table 2), logarithmic in the region 0.3 GeV$^{-1} \lesssim r \lesssim 4$ GeV^{-1}, and starts linearly rising at longer distances. As anticipated [39,33], the slopes of the logarithmic parts are common ($c_1 = 0.875 \pm 0.010$) to all $\alpha_s(m_Z)_{\overline{\rm MS}}$. In order to show the degree of constraints coming from the onium data, we show in Fig. 10 by dashed and dotted lines the region allowed by the five standard deviation shifts of the parameters r_0 and a, respectively, from their best fit values that are listed in Table 2. The one-sigma ranges obtained by the MINUIT program are

$$\begin{aligned} r_0 &= 0.235 \pm 0.010, \\ a &= 0.357 \pm 0.025, \end{aligned} \tag{5.18}$$

for $\alpha_s(m_Z)_{\overline{\rm MS}} = 0.12$.

In Fig. 11, we compare our QCD potential with other phenomenological potentials which all successfully describe the charmonium and bottomonium data. We give brief descriptions of the *Martin*, the *Cornell* and the *Richardson* potentials below:

1. *Martin potential* [44]:

$$V(r) = A + Br^{\nu} \tag{5.19}$$

with

$$A = -7.43,\ B = 7.32,\ \nu = 0.094, \tag{5.20}$$

$$m_c = 1.18, \quad m_b = 4.62 \tag{5.21}$$

in GeV units, which gives a total χ^2 of 190 [42,8].

2. *Cornell potential* [45]:

$$V(r) = -\frac{K}{r} + ar \tag{5.22}$$

with $K = 0.47$, $a = 0.19$ GeV^2, $m_c = 1.32$ GeV and $m_b = 4.75$ GeV, which gives a total χ^2 of 28 [42].

3. *Richardson potential* [46]:

$$\tilde{V}(\mathrm{q}^2) = -\frac{4}{3}\frac{12\pi}{33-2n_f}\frac{1}{\mathrm{q}^2}\frac{1}{\log(1+\mathrm{q}^2/\Lambda_R^2)} \tag{5.23}$$

with

$$\Lambda_R = 0.375 \text{ GeV}, \quad m_c = 1.50 \text{ GeV}, \quad m_b = 4.91 \text{ GeV}. \tag{5.24}$$

for $n_f = 4$, which leads to a total χ^2 of 18 [42,8].

All the data used in the fit and the predictions of the various phenomenological potentials above are listed in Table 3. Contribution of each data point to χ^2 and the sum are also given.

All the potentials in Fig. 11 have a common slope in the region (5.12), consistent with the observation of Buchmüler and Tye [33]. We note that the χ^2 value of the *Martin* potential is relatively large because it is too flat at the short distance limit of this region.

This can be seen from Table 3, where the majority of the large χ^2 of the *Martin* potential comes from its inability to reproduce the bottomonium mass difference $m(1P) - m(1S)$, which is sensitive to the potential in the region around $r \sim 1$ GeV^{-1}. The *Cornell* potential is the most singular at small r because of its Coulombic nature with a constant coupling, while the QCD motivated potential is softened by the running of the coupling constant at small r. The QCD short distance behavior starts showing up only in the region of

$$r \lesssim 0.2 \text{ GeV}^{-1} \tag{5.25}$$

which can be probed by the heavy $t\bar{t}$ system. The *Richardson* potential reproduces the QCD short distance behavior in the leading one-loop order, and it behaves similarly at very short distances to the two-loop improved perturbative potential $V_P(r)$ with $\Lambda^{(4)}_{\overline{\rm MS}} \sim 2\Lambda_R \sim 0.75$ GeV, or $\alpha_s(m_Z)_{\overline{\rm MS}} \sim 0.14$. Hence it may be regarded as an example of a successful QCD potential with a relatively large higher order corrections even at short distances around $r \sim 0.2$ GeV^{-1}. Although most potential models can account for the charmonium and bottomonium data reasonably well, they differ significantly at short distances where perturbative QCD gives quantitative predictions. Therefore we can expect that the detailed study of the $t\bar{t}$ production process will provide us with a good test of QCD.

6 Cross Sections

Using the techniques developed so far, we calculate both total cross sections and differential cross sections. In subsection 6.a, we discuss the dependence of the total cross sections on the physical parameters of the standard model, m_t, and $\alpha_s(m_Z)_{\overline{\rm MS}}$. In subsection 6.b, we study the differential cross sections and compare various phenomenological potentials. It reveals that simultaneous measurements of total and differential cross sections will lead to an efficient determination of α_s and m_t, since their dependences on these parameters are anti-correlated. This is discussed in subsection 6.c. We note that all figures presented in this section are based on the calculation of essentially the one-diagram evaluation (see Fig. 1). Other diagrams which contribute to the process $e^+e^- \to bW^+\bar{b}W^-$ may be added later as small backgrounds. We give a brief discussion on this point in section 7. In order to make our theoretical predictions clear, we do not take account of initial state radiation effects. Studies including both initial state radiation and beamstrahlung effects have been presented elsewhere [47].

6.a Total Cross Section

In this subsection, we discuss the total cross section calculated with the two-loop improved QCD potential presented in the previous section. The Z^0 contribution is now included at the tree level, where the terms proportional to the top-quark axial vector coupling are neglected for the consistency of our S-wave approximation. Also included is the normalization correction due to the hard gluon exchange at the vector $t\bar{t}$ vertex

$$1 - 8\alpha_s/3\pi, \tag{6.1}$$

which has been conventionally included in the calculation of quarkonium resonances [9, 10,33,48]. In this factor, α_s is evaluated at $\mu = m_t$ in the $\overline{\rm MS}$ scheme.

Total production cross sections are calculated directly from the formula (3.20)

$$\sigma_{tot}(e^+e^- \to t\bar{t} \to bW^+\bar{b}W^-) = 96\pi^2\alpha^2\left(1 - \frac{8\alpha_s}{3\pi}\right)^2\left[\frac{Q_t^2}{s^2} - \frac{2Q_t v_e v_t}{s(s-m_Z^2)} + \frac{(v_e^2+a_e^2)v_t^2}{(s-m_Z^2)^2}\right] \times Im\, G(\mathbf{x}=0; E=\sqrt{s}-2m_t), \tag{6.2}$$

where the above vertex correction and the Z^0 contributions are shown explicitly. The coupling factors are $v_e = (-\frac{1}{2}+2s^2)/2sc$, $v_t = (\frac{1}{2}-\frac{4}{3}s^2)/2sc$, $a_e = -1/4sc$ with $s = \sin\theta_W$ and $c = \cos\theta_W$, and $Q_t = 2/3$. We set $\alpha = 1/128$, $\sin^2\theta_W = 0.23$, $m_Z = 91.17$ GeV and $m_W = 80$ GeV in our numerical examples. The imaginary part of the Green's function at the origin has been calculated by using the formula given in Appendix C for each potential: eq. (C.20) for the Coulomb-like potential, and eq. (C.28) for the two-loop improved QCD potential. We note here again that we have neglected the contribution proportional to the top quark axial vector coupling a_t, which is small around the threshold [3] but can receive non-trivial [19] QCD corrections. This effect is presently under investigation [20].

In Figs. 12(a), (b), (c) are shown the total cross sections near threshold for m_t = 100, 150, 200 GeV, respectively, for three values of $\alpha_s(m_Z)_{\overline{\rm MS}}$; 0.11, 0.12, and 0.13. As m_t increases, the resonance structure is smeared out, since the top quark width Γ_t increases rapidly. (Γ_t = 0.095, 0.90, 2.5 GeV, respectively for m_t = 100, 150, 200 GeV). Also, the peak height decreases as it is proportional to Γ_t^{-1}. In each figure, we find that the resonance peaks shift to lower energies and its height is increased for larger α_s. This is because the resonance levels are lowered by the larger binding energy, and the wave functions of the resonance states at the origin, $\psi_n(0)$, grow at the same time.

In order to examine the sensitivity of the threshold cross section to the short distance part of the potential, we show in Fig. 13(a) the total cross section for m_t = 150 GeV with our QCD potential at $\alpha_s(m_Z)_{\overline{\rm MS}} = 0.12$ by a solid line. Also shown by dashed and dotted

lines are the predictions of the potentials with the same short distance behavior but with their intermediate distance part modified by shifting the parameter r_0 by five standard deviations away from its optimal value; see the dashed lines in Fig. 10 which shows the range of the potential covered by the above change of the parameter r_0. The three potentials differ significantly at $r \gtrsim 0.5\text{GeV}^{-1}$. The near degeneracy of the two curves demonstrates well that the short distant part of the potential essentially determines the threshold cross section. This is exactly what has been predicted by Fadin and Khoze [5], as a consequence of the large top quark decay width.

In order to study the effect of the top quark decay width, we show in Fig. 13(b) the same total cross section curves for $m_t = 150$ GeV, but with an artificially reduced top quark decay width ($\Gamma_t = 0.1$ GeV) by setting $|V_{tb}|^2 = 0.11$. The predictions of the three potentials with a common short distance behavior still agree well for the lowest resonance structure but they start deviating significantly for higher levels. This sensitivity to the long distance physics is lost in the realistic case with $\Gamma_t = 0.9$GeV shown in Fig. 13(a), where the effect from the region $r \cdot \Gamma_t \gtrsim 1$ of the phenomenological potential $V(r)$ is cut off by the smearing effect [6]; see Fig. 10.

6.b Differential Cross Section

Differential cross sections are calculated by using the formula

$$d\sigma(e^+e^- \to t\bar{t} \to bW^+\bar{b}W^-) = (1 - \frac{8\alpha_s}{3\pi})^2 \frac{1}{2s} \overline{\Sigma} \int d\Phi_4(bW^+\bar{b}W^-)|T_{fi}|^2 \,, \qquad (6.3)$$

where the matrix element T_{fi} of eq. (3.16) with both γ and Z contributions are calculated by HELAS [17]. The Green's function in momentum space $\tilde{G}(\mathbf{p}; E)$ is evaluated numerically for each potential as explained in detail in Appendices A to C. By integrating out the above differential cross section formula, the numerical program is found to reproduce accurately (at the level of 1–2 %) the results obtained from the total cross section formula eq. (6.2).

We should make one technical comment here: we used the relativistic form of the free top-quark propagator

$$D(p_t) \to 2m_t \Delta_F(p_t^2) = \frac{2m_t}{p_t^2 - m_t^2 + im_t\Gamma_t} \qquad (6.4)$$

in place of its non-relativistic expression (3.12). Although our non-relativistic formalism is not valid for highly off-shell top quarks where the difference is significant, we find that contributions from such highly off-shell top quarks are negligibly small. We also note that

the non-perturbative QCD enhancement factor $\tilde{G}(\mathrm{p};E)$ decreases for highly off-shell top quarks.

After integrating out the final bW^+ and $\bar{b}W^-$ decay angular distributions and integrating over the virtual top quark production angle about the e^+e^- beam direction, we find the double invariant mass distribution for the bW^+ and $\bar{b}W^-$ system:

$$\frac{d\sigma}{dp^2 d\bar{p}^2} = \frac{6\alpha^2 m_t^4}{\pi}\left(1-\frac{8\alpha_s}{3\pi}\right)^2\left[\frac{Q_t^2}{s^2}-\frac{2Q_t v_e v_t}{s(s-m_Z^2)}+\frac{(v_e^2+a_e^2)v_t^2}{(s-m_Z^2)^2}\right]|\tilde{G}(\mathrm{p};E)|^2$$
$$\times\bar{\beta}\left(\frac{p^2}{s},\frac{\bar{p}^2}{s}\right)|\Delta_F(p^2)+\Delta_F(\bar{p}^2)|^2\frac{\Gamma_t(p^2)}{\sqrt{p^2}}\frac{\Gamma_t(\bar{p}^2)}{\sqrt{\bar{p}^2}}\left(\frac{p^0\bar{p}^0}{m_t^2}+\frac{1}{3}\frac{\mathrm{p}^2}{m_t^2}\right), \qquad (6.5)$$

where $\bar{\beta}(a,b)=[1-2(a+b)+(a-b)^2]^{1/2}$ is the two-body phase space factor. The c.m. momentum of the bW system p is then expressed as

$$|\mathrm{p}|=\frac{\sqrt{s}}{2}\bar{\beta}\left(\frac{p^2}{s},\frac{\bar{p}^2}{s}\right). \qquad (6.6)$$

We first identify the quantity which is most sensitive to the QCD interaction in the differential cross sections. We note that all the information on QCD binding effects in the $t\bar{t}$ system are contained in the Green's function $\tilde{G}(\mathrm{p};E)$ that appears in the three-point function in (3.11). Writing

$$\tilde{G}(\mathrm{p};E)\simeq-\sum_n\frac{\phi_n(\mathrm{p})\psi_n^*(0)}{E-E_n+i\Gamma_n/2}, \qquad (6.7)$$

where $\psi_n(\mathrm{x})$ is the wave function of the n-th resonance state, and $\phi_n(\mathrm{p})$ is its Fourier transform, we see that the energy (E) dependence of $\tilde{G}(\mathrm{p};E)$ is essentially the same as for the total cross section, which is proportional to $Im\,G(0;E)$. On the other hand, its p-dependence is given by $\phi_n(\mathrm{p})$, the wave functions of the resonance states in momentum space. Thus, the scale of the E-dependence of $\tilde{G}(\mathrm{p};E)$ is set by $\Delta E\sim\alpha_s^2 m_t$ and Γ_t, while that of the p-dependence is set by $\Delta|\mathrm{p}|\sim\alpha_s m_t$. Therefore, it is best to look directly at the p-dependence of $\tilde{G}(\mathrm{p};E)$, since this provides us with information independent of that from the total cross section, and also because its dependence on the strong binding effects extends over a wide range of the momentum $\sim\alpha_s m_t$. As the differential cross section is proportional to $|\tilde{G}(\mathrm{p};E)|^2$, it is possible to observe directly the $|\mathrm{p}|$ dependence of $|\tilde{G}(\mathrm{p};E)|^2$ at a fixed energy $\sqrt{s}=2m_t+E$: the leading $|\mathrm{p}|$ dependence of the cross section is easily obtained from (6.5) as

$$\frac{d\sigma}{d|\mathrm{p}|} = \frac{6\alpha^2}{\pi}(1-\frac{8\alpha_s}{3\pi})^2\left[\frac{Q_t^2}{s^2}-\frac{2Q_t v_e v_t}{s(s-m_Z^2)}+\frac{(v_e^2+a_e^2)v_t^2}{(s-m_Z^2)^2}\right]$$
$$\times 4\pi\mathrm{p}^2|\tilde{G}(\mathrm{p};E)|^2\,\Gamma_\Theta(E,\mathrm{p}). \qquad (6.8)$$

Fig. 14 shows the $|\mathrm{p}|$-dependence of $|\tilde{G}(\mathrm{p};E)|^2$ multiplied by the phase space factor $4\pi\mathrm{p}^2$ for the QCD potential with $m_t = 150\,\mathrm{GeV}$ and $E = 0$. The peak shifts to larger $|\mathrm{p}|$ as α_s increases. This is due to the increase of the binding energy, which contributes to the kinetic energy of the $t\bar{t}$ system. Also the peak height increases with growing α_s, because of the increase of $|\psi_n(0)|$ as in the case of the total cross section.

In Fig. 15, we show the $|\mathrm{p}|$-dependence of $4\pi\mathrm{p}^2|\tilde{G}(\mathrm{p};E)|^2$ at several energies for the QCD potential. The distributions are given at four energies $E = \sqrt{s} - 2m_t = -6, -3, 0, +3$ GeV for $m_t = 150$ GeV and $\alpha_s(m_Z)_{\overline{\mathrm{MS}}} = 0.12$. There is no resonance enhancement at $E = -6$ GeV, and the factor $4\pi\mathrm{p}^2|\tilde{G}(\mathrm{p},E)|$ is essentially flat there. A clear broad peak appears in the distribution at larger energies. The peak position shifts to larger $|\mathrm{p}|$ as the energy increases.

Fig. 16(a) compares the $|\mathrm{p}|$-dependence of $4\pi\mathrm{p}^2|\tilde{G}(\mathrm{p};E)|^2$ for the various types of potentials, $V(r)$, which are listed in the previous section. The cross section for the Martin potential, which is finite at the origin, is the smallest in magnitude among these potentials. Other potentials are singular at the origin, and their cross sections are relatively large. For the Cornell potential which has a fixed strong coupling constant, $|\tilde{G}(\mathrm{p};E)|^2$ is larger than that for the QCD potential, as this coupling constant was fitted at the bottomonium and the charmonium energy scale; see Fig. 11 for the potential forms.

If we can distinguish the momentum distribution for the one-gluon exchange QCD potential from that for the Martin potential, we may confirm the QCD interaction for the binding of $t\bar{t}$. If we can distinguish it from the Cornell potential, we may confirm the running of the strong coupling constant α_s. We find that it is not an easy task to distinguish the Richardson potential from the two-loop improved QCD potential, mainly because the slopes of the potential are similar. In particular, our QCD potential for $\alpha_s(m_Z)_{\overline{\mathrm{MS}}} = 0.12$ and the best-fit Richardson potential are virtually indistinguishable at $r > 0.3\ \mathrm{GeV}^{-1}$. Only around the $r \sim 0.1\ \mathrm{GeV}^{-1}$ range is there a sizable difference in the slope (see Fig. 11).

In order to examine the shape of the distribution quantitatively, we show in Fig. 16(b) the same $4\pi\mathrm{p}^2|G(\mathrm{p};E)|^2$ distributions which are all rescaled to unity at the peak. Now the differences in the large $|\mathrm{p}|$ region clearly reflect the short distance behavior of the potentials. The Martin potential gives the smallest large $|\mathrm{p}|$ tail because of the absence of the short distance singularity, and the Cornell potential gives the hardest large $|\mathrm{p}|$ tail reflecting its strong Coulombic singularity. The Richardson potential gives the second hardest spectrum, in accordance with its short distance behavior in Fig. 11. A similar observation can be made in the comparison of different $\alpha_s(m_Z)_{\overline{\mathrm{MS}}}$ cases within the QCD

potential (see Fig. 14).

6.c Dependence of Cross Sections on α_s and m_t

One of the most important tasks of future e^+e^- collider experiments is to measure both α_s and m_t in the threshold region.

Even though one may hope that the value of the strong coupling constant $\alpha_s(m_Z)_{\overline{\rm MS}}$ will be well determined by the time of the e^+e^- collider experiments, the present situation [38,43] suggests that there are large higher order corrections to some quantities. Since the short distance potential is, in principle, the best place to measure the effective short distance coupling of QCD, it is desirable to have it independently determined in the top quark threshold production process. It has been known [11,12,47], however, that there is a strong correlation between the measurement of m_t and that of α_s. In this subsection, we explain that the two parameters are efficiently determined by measuring both total and differential cross sections simultaneously.

For the total cross section, if we increase α_s at fixed m_t, we find in Figs. 12(a)-(c) that the resonance peaks shifts to the left due to larger binding energies and at the same time the peak heights are increased. On the other hand, if we decrease m_t while keeping α_s fixed, we find that the peaks shift to the left as the threshold $2m_t$ is lowered. At the same time the peak heights are raised due to the swift reduction of resonance widths. Therefore, the threshold behavior of the total cross section scarcely changes when both m_t and α_s values are simultaneously raised (decreased) appropriately.

Now, in the case of the differential cross section, we find that the momentum distribution of $4\pi {\rm p}^2|\tilde{G}({\rm p};E)|^2$ shows the peak at the momentum scale $|{\rm p}| \sim \alpha_s m_t$. The peak position moves towards the right in Fig. 14 as we raise α_s at fixed m_t. Essentially the same effect is found when we raise m_t at fixed α_s. The differential distribution remains almost the same when m_t and α_s values are changed in the opposite direction such that their product $\alpha_s m_t$ remains constant.

Therefore, the correlations in the α_s and m_t measurements are opposite in the total and differential cross sections. This will in principle allow an efficient determination of the two parameters from the measurements in the threshold region. An accurate measurement of the $|{\rm p}|$ distribution would require a low beamstrahlung collider, a high resolution detector, and a good theoretical understanding of jet physics. This is certainly a challenge which is a worthy endeavor.

7 Discussion

In this section, we give a brief discussion on the unsatisfactory aspects of our non-relativistic formalism. One is that we have restricted our attention to the leading S-wave production of the $t\bar{t}$ pair, and that the P-wave contribution, the effect of the top quark axial vector coupling to the Z boson, has been neglected. Another more fundamental problem is that our non-relativistic formalism does not give a consistent prescription to deal with off-shell top quarks, whose effect has been found to be very important in the threshold region via the running of the effective toponium width.

In the electroweak theory, the off-shell top quark wave function depends on our choice of the gauge, and the correct bW distribution is obtained only after summing over all the electroweak amplitudes in a given order of the perturbation theory. In our problem, we should identify the off-shell top quark wave function in the presence of the non-perturbative QCD interactions. The problem may be illustrated by the one-loop QCD corrected diagrams in Fig. 17 for the process $e^+e^- \to \bar{t}bW^+$. In perturbation theory, the physical bW^+ spectrum is obtained only after summing all the amplitudes in Fig. 17. The leading Coulombic singularity, however, resides only in diagram (a), where the gluons exchanged in the t-channel can be summed to infinite orders [9] when the top-quark wave function has the non-relativistic form, eq. (4.9). In an attempt to develop an approach based on relativistic field theory, we find that the diagram Fig. 17(b) contributes to the threshold cross section in the non-leading order, which is formally of the same order as the known hard gluon exchange correction (6.1) as well as the P-wave axial vector contribution. Investigation in this direction is currently under way [20].

In the present paper, we identify only the leading contribution and the known conventional hard gluon exchange correction (6.1). In a simulation of e^+e^- collider events [11,12,47], however, we would like to have a realistic top quark angular distribution and the 4-body $bW^+\bar{b}W^-$ distributions. This can be achieved approximately by adding to the QCD corrected non-relativistic quark model amplitude T_{fi}^{NR} of eq. (3.16) the tree-level electroweak amplitude without QCD correction $T_{fi}^{(tree)}$ for the process $e^+e^- \to bW^+\bar{b}W^-$

$$T_{fi} = T_{fi}^{NR} + T_{fi}^{(tree)} - T_{fi}^{(tree,NR)}. \tag{7.1}$$

Here, in order to avoid double counting, the non-relativistic part $T_{fi}^{(tree,NR)}$ of the amplitude with both t and $\bar{t}$ propagators should be subtracted. This is equivalent to replacing in the tree-level electroweak amplitude $T_{fi}^{(tree)}$, the product of t and $\bar{t}$ propagators by the

following factor

$$\frac{[\not{p}_t + m_t]_{\alpha\gamma}}{p_t^2 - m_t^2 + im_t\Gamma_t}\frac{[\not{p}_{\bar{t}} - m_t]_{\delta\beta}}{p_{\bar{t}}^2 - m_t^2 + im_t\Gamma_t} - \frac{m_t[\gamma^0 + 1]_{\alpha\gamma}}{p_t^2 - m_t^2 + im_t\Gamma_t}\frac{m_t[\gamma^0 - 1]_{\delta\beta}}{p_{\bar{t}}^2 - m_t^2 + im_t\Gamma_t}. \qquad (7.2)$$

Since it is seen in sect. 4.c that the amplitude proportional to the product of the non-relativistic top-quark propagators gives a mild off-shell behavior consistent with the W_L Nambu-Goldston boson equivalence theorem [25] in the $g_W \to 0$ limit, the sum of the rest of the tree diagrams should also give the mild behavior. The electroweak angular asymmetries are reproduced at the tree level, which is subject to non-leading QCD corrections [19,20].

8 Conclusion

In this paper, we presented a novel formalism to calculate the total and differential cross sections for heavy unstable top-quark pair production near threshold.

After giving an intuitive picture of top-quark pair production and their decay in the attractive QCD potential in section 2, we presented in sections 3 and 4 the non-relativistic formulation to calculate the cross sections near the $t\bar{t}$ threshold by incorporating the QCD binding effect. Our formalism allows us to calculate reliably not only the total cross sections but also the differential cross sections. We demonstrated the importance of using the running toponium width $\Gamma_\Theta(E, \mathrm{p})$, instead of the commonly used constant width $\Gamma_\Theta = 2\Gamma_t(m_t^2)$. The use of the running width is necessary to keep the unitarity relation between the total cross section obtained from summing the final states and that calculated by using the optical theorem; see Fig. 5. The introduction of the running toponium width $\Gamma_\Theta(E, \mathrm{p})$ has been found to give a considerable effect in the determination of the Schrödinger Green's function $G(\mathrm{x}; E)$ and its Fourier transform $\tilde{G}(\mathrm{p}; E)$, which dictate the overall spectral structure of resonances as well as the distributions of $t\bar{t}$ inside the toponium. $\Gamma_\Theta(E, \mathrm{p})$ is determined by the electroweak interaction, whereas the non-perturbative strong interaction governs the Green's function $\tilde{G}(\mathrm{p}; E)$ which gives the momentum distribution of $t\bar{t}$. Their interplay determines the decay widths of the physical resonance states, Γ_n, to be considerably smaller than twice the on-shell top quark width $2\Gamma_t(m_t^2)$. This reflects the increase of the kinetic energies of t and $\bar{t}$ inside the toponium due to the binding energy, as well as lack of phase space for deeply bound states.

In section 5, we determined our phenomenological potential with the two-loop improved QCD behavior at short distances. It was argued that the masses of bottom and

charm quarks inside the exchanged gluon cannot be neglected for the determination of the short distance potential in the region relevant to the toponium resonances.

In section 6, we showed the total and differential cross sections for various values of m_t and α_s. We found that the correlation in the m_t and α_s measurements are opposite in the differential distribution compared to the correlation in the total cross section. Therefore studies of the differential distributions will lead to an efficient determination of the two parameters. The investigation of differential cross sections will provide us with information independent of that extracted from the total cross sections, since we may directly observe the wave function of toponium states in momentum space. We also compared the differential cross sections for various phenomenological potentials.

In section 7, we gave a brief discussion on the limitation of the present non-relativistic formalism. The P-wave contributions and the off-shell top quark wave functions were not taken into account in our framework, and we presented a simple prescription to incorporate these effects at the tree-level of the electroweak theory, in the zero binding limit. A consistent treatment of these effects based directly on relativistic field theory is currently under-way [20].

In Appendices A-C, we show technical details of solving the Schrödinger equation (3.13) for the Green's function $G(\mathrm{x}; E)$ with the running toponium width $\Gamma_\Theta(\mathrm{p}, E)$. Boundary conditions for Coulomb-like and QCD potentials are explicitly solved in Appendix C.

Acknowledgements:

The authors wish to thank discussions with K. Hikasa, K. Higashijima, S. Ishihara, V. Khoze, J.H. Kühn, A.D. Martin, N. McDougall, M.G. Olsson, M. Peskin, D. Zeppenfeld, P.M. Zerwas, and the members of the Japan Linear Collider physics working group. One of the authors (K.H.) thanks UK Science and Engineering Research Council for a Visiting Fellowship. This work was also supported by US Department of Energy contract DE-AC03-76SF00515, and by MESC (Ministry of Education, Science and Culture, Japan) under Grant-in-Aid International Science Research Program No. 03041087.

Appendix A: Evaluation of the Green's Function

In this appendix, we present details of our calculation of the Green's function $G(\mathbf{x}; E)$ which satisfies the time-independent inhomogeneous Schrödinger equation (3.13)

$$\left\{-\frac{\Delta}{m_t} + V(r) - \left(E + i\frac{\Gamma_\Theta}{2}\right)\right\} G(\mathbf{x}; E) = \delta^3(\mathbf{x}), \tag{A.1}$$

with the running width of toponium $\Gamma_\Theta(E, \mathbf{p})$ given by (4.22).

Let us rewrite $\Gamma_\Theta(E, \mathbf{p})$ in the form

$$\Gamma_\Theta(E, \mathbf{p}) = \Gamma_0 - 2\kappa \frac{\mathbf{p}^2}{m_t} \tag{A.2}$$

with

$$\Gamma_0 = \frac{G_F}{\sqrt{2}} \frac{m_t^3}{4\pi} \eta_1, \qquad \kappa = \frac{G_F}{\sqrt{2}} \frac{m_t^2}{8\pi} \eta_2. \tag{A.3}$$

Inserting (A.2) and $\mathbf{p}^2 = -\Delta$ into (A.1), we are led to solve the Schrödinger equation

$$\left[-\frac{\Delta}{\mu} + V(r) - \left(E + i\frac{\Gamma_0}{2}\right)\right] G(\mathbf{x}; E) = \delta^3(\mathbf{x}) \tag{A.4}$$

with the complex effective mass defined as

$$\mu = \frac{m_t}{1 + i\kappa}. \tag{A.5}$$

Since the above equation has the same structure as the Schrödinger equation with a "constant" width, it may seem that we can directly apply the general method for evaluating $G(\mathbf{x}; E)$ and $Im\, G(0; E)$. We need, however, to be careful on one specific point for the evaluation of $Im\, G(0; E)$. To see the problem clearly, again we use the unitarity relation between the Green's functions:

$$2\, Im\, G(0; E) = \int \frac{d^3\mathbf{p}}{(2\pi)^3} |\tilde{G}(\mathbf{p}; E)|^2\, \Gamma_\Theta(E, \mathbf{p}). \tag{A.6}$$

If we look at the large $|\mathbf{p}|$ behavior of the integrand on the r.h.s., we find that this integral is linearly divergent at $|\mathbf{p}| \to \infty$. In fact, the large momentum part of $\tilde{G}(\mathbf{p}; E)$ is solely determined by the short distance behavior of the potential $V(r)$ and, for the Coulomb-like potential, it behaves like the free propagator as $\tilde{G}(\mathbf{p}; E) \to \mu/\mathbf{p}^2$ for $|\mathbf{p}| \gg \alpha_s m_t$, while $\Gamma_\Theta \to -\kappa(\mathbf{p}^2/m_t)$. Hence, we suffer from divergence in evaluating $Im\, G(0; E)$.

Nevertheless we find that this divergence is unphysical. The quadratic divergence of Γ_Θ as $|\mathbf{p}| \to \infty$ stems from our approximation of neglecting the higher order terms in

(4.22). In fact we notice that $\Gamma_\Theta(E,\mathrm{p})$ disappears for the kinematical configuration of $t\bar{t}$ where $k_1^2 \leq m_W^2$ due to the appearance of $\Gamma_t(k_1^2)$ in (4.20). This leads to a cut-off in the momentum[19] at

$$\Lambda^2 = \frac{1}{4(2m_t+E)^2}\left[(3m_t+E)^2 - m_W^2\right]\left[(m_t+E)^2 - m_W^2\right]. \tag{A.7}$$

For $\mathrm{p}^2 > \Lambda^2$, there would be no allowed $t\bar{t}$ configuration such that $k_0^2 = m_t^2$ and $k_1^2 \geq m_W^2$. Thus we should cut off our phase space integration on the r.h.s. of (A.6), and obtain

$$2\,Im\,G(0;E)\Big|_{\mathrm{p}^2<\Lambda^2} \equiv \int_{\mathrm{p}^2<\Lambda^2} \frac{d^3\mathrm{p}}{(2\pi)^3}\,|\tilde{G}(\mathrm{p};E)|^2\,\Gamma_\Theta(E,\mathrm{p}). \tag{A.8}$$

This is the very quantity we need for obtaining the total cross section, which correctly incorporates the cut-off in the running width $\Gamma_\Theta(E,\mathrm{p})$ [49]. (In the actual calculation we have cut off the integration at $\mathrm{p}^2 = \Lambda_{eff}^2$ where the $\Gamma_\Theta(E,\mathrm{p})$ given by (4.22) becomes zero.) Fig. 18 shows the $|\mathrm{p}|$-dependence of the integrand in the above equation multiplied by the phase space factor $4\pi\mathrm{p}^2$. We see that it becomes a negative constant for $|\mathrm{p}| \gg \alpha_s m_t$.

We may now transform the r.h.s. of (A.8) to the x-space representation:

$$\begin{aligned}\int_{\mathrm{p}^2<\Lambda^2} \frac{d^3\mathrm{p}}{(2\pi)^3}\,|\tilde{G}(\mathrm{p};E)|^2\,\Gamma_\Theta(E,\mathrm{p}) &= 2\int d^3\mathrm{x}\,\bar{\delta}(\mathrm{x};\Lambda)\,Im\,G(\mathrm{x};E) \\ &+ 2\int d^3\mathrm{x}d^3\mathrm{y}\,\bar{\delta}(\mathrm{x}-\mathrm{y};\Lambda)\,V(|\mathrm{x}|)\,Im\left[G(\mathrm{x};E)G^*(\mathrm{y};E)\right]\end{aligned} \tag{A.9}$$

where we have introduced the cut-off function

$$\bar{\delta}(\mathrm{x};\Lambda) \equiv \int_{\mathrm{p}^2<\Lambda^2} \frac{d^3\mathrm{p}}{(2\pi)^3}\,e^{i\mathrm{p}\cdot\mathrm{x}} = \frac{1}{2\pi^2 r^3}\left[\sin(\Lambda r) - \Lambda r\cos(\Lambda r)\right] \tag{A.10}$$

with $r = |\mathrm{x}|$. We present the technical proof of eq. (A.9) in Appendix B. The cut-off function $\bar{\delta}(\mathrm{x};\Lambda)$ reduces to $\delta^3(\mathrm{x})$ as $\Lambda \to \infty$. If we look at the first term on the r.h.s. of (A.9), we see that $Im\,G(\mathrm{x};E)$ is smeared out around $\mathrm{x}=0$ over a size $\sim \Lambda^{-1}$. As this term reduces to $Im\,G(0;E)$ when we move the cut-off to infinity, it is expected to be the main term related to $Im\,G(0;E)$. The second term vanishes as $\Lambda \to \infty$ since the integrand becomes real.

We refer the reader to ref. [9] for the details of the method for finding $G(\mathrm{x};E)$ by numerically solving the Schrödinger equation (A.4). There it is shown systematically that the S-wave contribution to $G(\mathrm{x};E)$ is given in terms of the solution to the one-dimensional homogeneous Schrödinger equation as

$$G(\mathrm{x};E) = \frac{\mu}{4\pi}\frac{g_>(r)}{r}, \tag{A.11}$$

$$\left[\frac{d^2}{dr^2} + \mu(E + i\Gamma_0/2 - V(r))\right] g_>(r) = 0, \tag{A.12}$$

with the boundary condition

$$\lim_{r\to 0} g_>(r) = 1, \tag{A.13}$$

$$\lim_{r\to\infty} g_>(r) = 0. \tag{A.14}$$

Specifically, for the Coulombic potential

$$V(r) = -\frac{4}{3}\frac{\alpha_s}{r} \tag{A.15}$$

with a constnat α_s, the solution $g_>(r)$ may be determined to be a linear combination of the two solutions $g_0(r)$ and $g_1(r)$ of the same homogeneous equation (A.12) whose analytical behaviors near the origin are given by

$$g_0(r) = r + O(r^2), \tag{A.16}$$

$$g_1(r) = 1 - \beta r \log(r/r_0) + O(r^2 \log r), \tag{A.17}$$

with $\beta = \frac{4}{3}\alpha_s\mu$. We may then solve (A.12) numerically to obtain g_0 and g_1 starting from $r = 0$. If we write

$$g_>(r) = g_1(r) + B\, g_0(r), \tag{A.18}$$

the constant B is determined from the asymptotic behavior of $g_0(r)$ and $g_1(r)$. The boundary condition (A.14) implies

$$B = -\lim_{r\to\infty} \frac{g_1(r)}{g_0(r)}. \tag{A.19}$$

Thus we obtain $G(\mathrm{x}; E)$ from (A.11). The Green's function in momentum space is given by

$$\tilde{G}(\mathrm{p}; E) = \frac{\mu}{p}\int_0^\infty dr\, g_>(r)\, \sin pr \tag{A.20}$$

with $p = |\mathrm{p}|$.

It is easier to evaluate $Im\, G(0; E)|_{\mathrm{p}^2<\Lambda^2}$ from which we can calculate the total cross section. By substituting the Green's function (A.11) to (A.9), we find

$$2\, Im\, G(0;E)\Big|_{\mathrm{p}^2<\Lambda^2} = 2\, Im\left[\frac{\mu}{4\pi}\left\{\frac{2\Lambda}{\pi} + B + \beta(\gamma_E - 1 + \log(\Lambda r_0))\right\}\right] - \frac{|\mu|^2}{2\pi^2}\frac{\Gamma_0}{\Lambda} \tag{A.21}$$

for the Coulombic potential; see Appendix C for the proof and the corresponding formula for the QCD potential. Here $\gamma_E = 0.5772...$ denotes Euler's constant. Therefore, by first fixing some r_0 and determining B, one obtains $Im\, G(0, E)|_{\mathrm{p}^2<\Lambda^2}$. It can be shown that (A.21) is independent of the choice of r_0. The above formula matches well with the correct value given by evaluating eq. (A.8) directly, as shown in Fig. 19.

Appendix B

In this appendix, we derive eq. (A.9):

$$\int_{\mathrm{p}^2<\Lambda^2} \frac{d^3\mathrm{p}}{(2\pi)^3} |\tilde{G}(\mathrm{p};E)|^2 \Gamma_\Theta(E,\mathrm{p}) \;=\; 2\int d^3\mathrm{x}\, \bar{\delta}(\mathrm{x};\Lambda)\, Im\, G(\mathrm{x};E) + 2\int d^3\mathrm{x} d^3\mathrm{y}\, \bar{\delta}(\mathrm{x}-\mathrm{y};\Lambda)\, V(|\mathrm{x}|)\, Im\,[G(\mathrm{x};E)G^*(\mathrm{y};E)]. \tag{B.1}$$

Let us first define the operator Q representing the denominator of the Green's function:

$$Q = H - \left(E + i\frac{\Gamma_\Theta}{2}\right) \tag{B.2}$$

where the Hamiltonian and the running width

$$H = \frac{\mathrm{p}^2}{m_t} + V(r), \qquad \Gamma_\Theta = \Gamma_0 - 2\kappa\frac{\mathrm{p}^2}{m_t}, \tag{B.3}$$

are the Hermite operators. Γ_Θ can be expressed in terms of Q as

$$\Gamma_\Theta = i(Q - Q^\dagger), \tag{B.4}$$

and the Green's functions can be expressed as

$$G(\mathrm{x};E) = \langle \mathrm{x}\,|\,Q^{-1}\,|\,\mathrm{x}'=0\,\rangle\,, \tag{B.5}$$

$$\tilde{G}(\mathrm{p};E) = \langle \mathrm{p}\,|\,Q^{-1}\,|\,\mathrm{x}'=0\,\rangle\,. \tag{B.6}$$

These relations enable us to rewrite the l.h.s. of (B.1) as follows:

$$\begin{aligned}
&\int_{\mathrm{p}^2<\Lambda^2} \frac{d^3\mathrm{p}}{(2\pi)^3} |\tilde{G}(\mathrm{p};E)|^2 \Gamma_\Theta(E,\mathrm{p}) \\
&= \int_{\mathrm{p}^2<\Lambda^2} \frac{d^3\mathrm{p}}{(2\pi)^3} \langle \mathrm{x}'=0\,|\,(Q^\dagger)^{-1}|\,\mathrm{p}\,\rangle\,\langle \mathrm{p}\,|\,\Gamma_\Theta Q^{-1}|\,\mathrm{x}'=0\,\rangle \\
&= i\int_{\mathrm{p}^2<\Lambda^2} \frac{d^3\mathrm{p}}{(2\pi)^3} \left[\langle \mathrm{x}'=0\,|\,(Q^\dagger)^{-1}|\,\mathrm{p}\,\rangle - \langle \mathrm{x}'=0\,|\,(Q^\dagger)^{-1}|\,\mathrm{p}\,\rangle\,\langle \mathrm{p}\,|\,Q^\dagger Q^{-1}|\,\mathrm{x}'=0\,\rangle\right].
\end{aligned} \tag{B.7}$$

In the last line, we want to move $Q^\dagger$ to the left of $|\,\mathrm{p}\,\rangle\langle\mathrm{p}\,|$ so that it annihilates with $(Q^\dagger)^{-1}$. All operators which are diagonal in p can be moved. Thus we find

$$(Q^\dagger)^{-1}\,|\,\mathrm{p}\,\rangle\langle\mathrm{p}\,|\,Q^\dagger \;=\; |\,\mathrm{p}\,\rangle\langle\mathrm{p}\,| + (Q^\dagger)^{-1}|\,\mathrm{p}\,\rangle\langle\mathrm{p}\,|\,V(r) - (Q^\dagger)^{-1}V(r)\,|\,\mathrm{p}\,\rangle\langle\mathrm{p}\,|. \tag{B.8}$$

Inserting (B.8) into (B.7), and using the completeness relation $\int d^3\mathrm{x}\,|\,\mathrm{x}\,\rangle\langle\,\mathrm{x}\,|=1$, we can express the integral in terms of the Green's functions:

$$\begin{aligned}
&\int_{\mathrm{p}^2<\Lambda^2}\tfrac{d^3\mathrm{p}}{(2\pi)^3}\,|\tilde{G}(\mathrm{p};E)|^2\,\Gamma_\Theta(E,\mathrm{p}) \\
&\qquad = i\int_{\mathrm{p}^2<\Lambda^2}\tfrac{d^3\mathrm{p}}{(2\pi)^3}\,\left[\langle\mathrm{x}'=0\,|\,(Q^\dagger)^{-1}\,|\,\mathrm{p}\,\rangle-\langle\mathrm{p}\,|\,Q^{-1}\,|\,\mathrm{x}'=0\,\rangle\right] \\
&\qquad + i\int_{\mathrm{p}^2<\Lambda^2}\tfrac{d^3\mathrm{p}}{(2\pi)^3}\,\Big[\langle\mathrm{x}'=0\,|\,(Q^\dagger)^{-1}V(r)\,|\,\mathrm{p}\,\rangle\,\langle\mathrm{p}\,|\,Q^{-1}\,|\,\mathrm{x}'=0\,\rangle \\
&\qquad\qquad -\langle\mathrm{x}'=0\,|\,(Q^\dagger)^{-1}\,|\,\mathrm{p}\,\rangle\,\langle\mathrm{p}\,|\,V(r)Q^{-1}\,|\,\mathrm{x}'=0\,\rangle\Big] \qquad \text{(B.9)} \\
&\qquad = i\int d^3\mathrm{x}\int_{\mathrm{p}^2<\Lambda^2}\tfrac{d^3\mathrm{p}}{(2\pi)^3}\,\left[e^{i\mathrm{p}\cdot\mathrm{x}}G^*(\mathrm{x};E)-e^{-i\mathrm{p}\cdot\mathrm{x}}G(\mathrm{x};E)\right] \\
&\qquad + i\int d^3\mathrm{x}\int d^3\mathrm{y}\int_{\mathrm{p}^2<\Lambda^2}\tfrac{d^3\mathrm{p}}{(2\pi)^3}V(|\mathrm{x}|) \\
&\qquad\quad \times\left[G^*(\mathrm{x};E)G(\mathrm{y};E)e^{i\mathrm{p}\cdot(\mathrm{x}-\mathrm{y})}+G(\mathrm{x};E)G^*(\mathrm{y};E)e^{-i\mathrm{p}\cdot(\mathrm{x}-\mathrm{y})}\right] \qquad \text{(B.10)}
\end{aligned}$$

Now we define the cut-off function $\bar{\delta}(\mathrm{x};\Lambda)$ as

$$\bar{\delta}(\mathrm{x};\Lambda)\equiv\int_{\mathrm{p}^2<\Lambda^2}\tfrac{d^3\mathrm{p}}{(2\pi)^3}\,e^{i\mathrm{p}\cdot\mathrm{x}}=\frac{1}{2\pi^2r^3}\left[\sin(\Lambda r)-\Lambda r\cos(\Lambda r)\right] \qquad \text{(B.11)}$$

with $r=|\mathrm{x}|$. It is then straightforward to show that (B.10) reduces to the r.h.s. of (B.1).

Appendix C: Formula for $Im\, G(0;E)$

In this appendix we present analytic expressions for the total rate

$$2\, Im\, G(0;E)\Big|_{\mathrm{p}^2<\Lambda^2} \equiv \int_{\mathrm{p}^2<\Lambda^2} \frac{d^3\mathrm{p}}{(2\pi)^3} |\tilde{G}(\mathrm{p};E)|^2\, \Gamma_{\mathrm{e}}(E,\mathrm{p}) \tag{C.1}$$

$$= 2\int d^3\mathrm{x}\, \bar{\delta}(\mathrm{x};\Lambda)\, Im\, G(\mathrm{x};E)$$

$$+ 2\int d^3\mathrm{x} d^3\mathrm{y}\, \bar{\delta}(\mathrm{x}-\mathrm{y};\Lambda)\, V(|\mathrm{x}|)\, Im\, [G(\mathrm{x};E)G^*(\mathrm{y};E)], \tag{C.2}$$

by expanding $G(\mathrm{x};E)|_{\mathrm{p}^2<\Lambda^2}$ in terms of Λ. We show the results for the case where the short distance behavior of the potential $V(r)$ is either Coulomb-like (I), or QCD-like (II) with the asymptotically free running coupling constant.

(I) Coulomb-like potential

We consider the potential that behaves as

$$V(r) \sim -C_F \frac{\alpha_s}{r} \quad \text{for } r \to 0 \tag{C.3}$$

with constant α_s.

With this asymptotic form of the potential, one may determine $g_>(r)$, the solution to the homogeneous Schrödinger equation

$$\left[\frac{d^2}{dr^2} + \mu(E + i\Gamma_0/2 - V(r))\right] g_>(r) = 0, \tag{C.4}$$

with the boundary conditions

$$\lim_{r\to 0} g_>(r) = 1, \tag{C.5}$$

$$\lim_{r\to\infty} g_>(r) = 0. \tag{C.6}$$

We first determine the two solutions, $g_0(r)$ and $g_1(r)$, to the same Schrödinger equation with the boundary conditions

$$g_0(r) = r + \ldots \tag{C.7}$$

$$g_1(r) = 1 + \ldots \tag{C.8}$$

and

$$\frac{dg_0}{dr} = 1 + \ldots \tag{C.9}$$

$$\frac{dg_1}{dr} = -\beta\,[\log(r/r_0) + 1] + \ldots \tag{C.10}$$

with $\beta = C_F\,\alpha_s\mu$. By fixing some r_0, we may solve for $g_0(r)$ and $g_1(r)$, in terms of which $g_>(r)$ is obtained:

$$g_>(r) = g_1(r) + B\,g_0(r), \tag{C.11}$$

$$B = -\lim_{r\to\infty}\frac{g_1(r)}{g_0(r)}. \tag{C.12}$$

Then the Green's function is given by

$$G(\mathrm{x};E) = \frac{\mu}{4\pi}\frac{g_>(r)}{r}. \tag{C.13}$$

To evaluate $2\,Im\,G(\mathrm{x};E)|_{\mathrm{p}^2<\Lambda^2}$, let us first use the x-space representation (C.2), and neglect all terms that vanish as $\Lambda\to\infty$. In this limit the second term disappears, so that the contribution only comes from the first term. We may rewrite the integral in the first term using $g_>(r)$ as

$$\begin{aligned}\int d^3\mathrm{x}\,G(\mathrm{x};E)\,\bar{\delta}(\mathrm{x};\Lambda) &= -\frac{\mu}{2\pi^2}\int_0^\infty dr\,g_>(r)\frac{d}{dr}\left(\frac{\sin\Lambda r}{r}\right)\\ &= \frac{\mu}{2\pi^2}\Lambda + \frac{\mu}{2\pi^2}\int_0^\infty dr\,\frac{\sin\Lambda r}{r}\frac{dg_>(r)}{dr}.\end{aligned} \tag{C.14}$$

Since $\bar{\delta}(\mathrm{x};\Lambda)$ reduces to $\delta^3(\mathrm{x})$ as $\Lambda\to\infty$, we need to consider only the components of $G(\mathrm{x};E)$ that are non-vanishing as $\mathrm{x}\to 0$ in the above equation. This corresponds to keeping terms up to the order r^1 in $g_>(r)$ as

$$g_>(r) = 1 - \beta r\log(r/r_0) + Br, \tag{C.15}$$

or equivalently

$$\frac{dg_>(r)}{dr} = -\beta\left[\log(r/r_0)+1\right] + B. \tag{C.16}$$

Inserting this into (C.14), we have

$$\begin{aligned}\int d^3\mathrm{x}\,G(\mathrm{x};E)\,\bar{\delta}(\mathrm{x};\Lambda) &= \frac{\mu}{4\pi}\left\{\frac{2\Lambda}{\pi} + B + \beta(\gamma_E - 1 + \log\Lambda r_0)\right\}\\ &\quad + (\text{terms that vanish as } \Lambda\to\infty).\end{aligned} \tag{C.17}$$

We further consider the order $1/\Lambda$ corrections to the above expression. For this purpose we may use the momentum-space representation (C.1). The asymptotic behavior of $\tilde{G}(\mathrm{p};E)$ as $\mathrm{p}\to\infty$ is determined from the short distance behavior of the potential $V(r)$, and for $E,\Gamma_0 \sim \alpha_s^2 m_t$, it may be expanded as

$$\tilde{G}(\mathrm{p};E) \sim -\frac{\mu}{\mathrm{p}^2}\sum_{n=0}^{\infty} C_n\left(\frac{\alpha_s m_t}{|\mathrm{p}|}\right)^n \quad (\text{as } \mathrm{p}\to\infty) \tag{C.18}$$

with $C_0 = 1$ and other C_n's of the order of unity. Note that $\tilde{G}(\mathrm{p}; E)$ reduces to the free propagator for $|\mathrm{p}| \gg \alpha_s m_t$. Substituting (C.18) into (C.1), we may find the order $1/\Lambda$ terms. If we neglect the term that is suppressed by the coefficient κ given in (A.3), the only term of this order is found to be

$$-\frac{|\mu|^2}{2\pi^2}\frac{\Gamma_0}{\Lambda}. \tag{C.19}$$

Thus, we obtain the imaginary part of the Green's function with the cut off in momentum space as

$$2\,Im\,G(0;E)\Big|_{\mathrm{p}^2<\Lambda^2} \simeq 2\,Im\,\left[\frac{\mu}{4\pi}\left\{\frac{2\Lambda}{\pi}+B+\beta(\gamma_E-1+\log\Lambda r_0)\right\}\right]-\frac{|\mu|^2}{2\pi^2}\frac{\Gamma_0}{\Lambda} \tag{C.20}$$

neglecting terms of order $1/\Lambda^2$.

(II)The QCD potential

The short distance behavior of the QCD potential which incorporates the running of the strong coupling constant α_s is given by

$$\begin{aligned} V(r) &\sim -\frac{C_F}{r}\frac{\pi/b_0}{\log(r_{QCD}/r)+(b_1/b_0^2)\log\log(r_{QCD}/r)} \\ &\simeq -\frac{\pi C_F}{b_0}\left[\frac{1}{r\log(r_{QCD}/r)}-\frac{b_1}{b_0^2}\frac{\log\log(r_{QCD}/r)}{r\{\log(r_{QCD}/r)\}^2}\right]. \end{aligned} \tag{C.21}$$

Here, r_{QCD} is related to the QCD scale parameter as

$$r_{QCD}=\frac{1}{\Lambda^{(5)}_{\overline{MS}}}\exp\left[-\frac{A(0)}{b_0}\right]\left(\frac{2b_1}{b_0^2}\right)^{b_1/b_0^2}\simeq\frac{0.365}{\Lambda^{(5)}_{\overline{MS}}}. \tag{C.22}$$

The solution to the homogeneous Schrödinger equation $g_>(r)$ may be determined in terms of $g_0(r)$ and $g_1(r)$, whose asymptotic behaviors near the origin are given by

$$g_0(r) = r+\ldots \tag{C.23}$$

$$g_1(r) = 1+\ldots \tag{C.24}$$

and

$$\frac{dg_0}{dr} = 1+\ldots \tag{C.25}$$

$$\frac{dg_1}{dr} = \tilde{\beta}\left[\log(A\log(r_{QCD}/r))+\frac{b_1}{b_0^2}\frac{\log\log(r_{QCD}/r)+1}{\log(r_{QCD}/r)}\right]+\ldots, \tag{C.26}$$

where A is an arbitrary constant, and $\tilde{\beta} = (\pi C_F/b_0)\,\mu$. By fixing A to some value, we may solve for $g_0(r)$ and $g_1(r)$, then $g_>(r)$ is expressed by their linear combination as in (C.11) and (C.12). We find that the derivative of $g_>(r)$ is given by

$$\frac{dg_>}{dr} = \tilde{\beta}\left[\log(A\log(r_{QCD}/r)) + \frac{b_1}{b_0^2}\frac{\log\log(r_{QCD}/r)+1}{\log(r_{QCD}/r)}\right] + B + \ldots \qquad \text{(C.27)}$$

near the origin.

Following the same steps as we did for the Coulomb-like potential, we obtain

$$\begin{aligned} &2\,Im\,G(0;E)\Big|_{\mathbf{p}^2<\Lambda^2} \\ &\quad\simeq 2\,Im\left[\frac{\mu}{4\pi}\left\{\frac{2\Lambda}{\pi} + B + \tilde{\beta}\left(\log A + f_1(\Lambda r_{QCD}) + \frac{b_1}{b_0^2}f_2(\Lambda r_{QCD})\right)\right\}\right] - \frac{|\mu|^2}{2\pi^2}\frac{\Gamma_0}{\Lambda} \end{aligned} \qquad \text{(C.28)}$$

with

$$f_1(x) = \frac{2}{\pi}\int_0^{t_{max}}\frac{dt}{t}\sin t\ \log\log(x/t), \qquad \text{(C.29)}$$

$$f_2(x) = \frac{2}{\pi}\int_0^{t_{max}}\frac{dt}{t}\sin t\ \frac{\log\log(x/t)+1}{\log(x/t)}, \qquad \text{(C.30)}$$

where the infrared singularity is regularized by cutting off the integral region at $t_{max} = xe^{-1}$.

References and Footnotes

[1] K. Fujikawa, *Prog. Theor. Phys.* **61**, 1186 (1979).

[2] J.H. Kühn, *Acta Physica Austriaca, Suppl.* **24**, 203 (1982).

[3] J. Jersak, E. Laermann and P.M. Zerwas, *Phys. Rev.* **D25**, 1219 (1982); S. Güsken, J.H. Kühn and P.M. Zerwas, *Phys. Lett.* **155B**, 185 (1985).

[4] I. Bigi, Y. Dokshitzer, V. Khoze, J.H. Kühn and P.M. Zervas, *Phys. Lett.* **B181**, 157 (1986).

[5] V.S. Fadin and V.A. Khoze, *JETP Lett.* **46**, 417 (1987); see also V.S. Fadin, V. Khoze and T. Sjöstrand, *Z. Phys.* **C48**, 613 (1990).

[6] E.C. Poggio, H.R. Quinn and S. Weinberg, *Phys. Rev.* **D13**, 1958 (1976).

[7] L.F. Abbott, P. Sikivie and M.B. Wise, *Phys. Rev.* **D21**, 1393 (1980); M. Sher and D. Silverman, *Phys. Rev.* **D31**, 95 (1985); G.G. Athanasiu, P.J. Franzini and F.J. Gilman, *Phys. Rev.* **D32**, 3010(1985).

[8] K. Hagiwara, K. Kato, A. D. Martin and C.-K. Ng, *Nucl. Phys.* **B344**, 1 (1990).

[9] M. Strassler and M. Peskin, *Phys. Rev.* **D43**, 1500 (1991).

[10] W. Kwong, *Phys. Rev.* **D43**, 1488 (1991).

[11] S. Komamiya, SLAC-PUB-5324 (1991).

[12] K. Fujii, *Proceedings of the 2nd Workshop on JLC* (1990), KEK Proceedings 91-10, p.271.

[13] J.H. Kühn and P.M. Zerwas, *Phys. Rep.* **167**, 321 (1988).

[14] The intricate role of the QCD and electroweak gauge invariance which necessitates a modification of this simple splitting picture for unstable top quarks will be discussed later in section 7.

[15] F. Feinberg, *Phys. Rev.* **17D**, 2659 (1978).

[16] The Hamiltonian (3.1) dictates the QCD interaction of t and $\bar{t}$, which is defined to operate in the subspace of t and $\bar{t}$. The electroweak interactions responsible for their decays are treated as a perturbation, which may be effectively included as the anti-Hermitian part in the Hamiltonian.

[17] H. Murayama, I. Watanabe and K. Hagiwara, *"HELAS: Helicity Amplitude Subroutines for Feyman diagram evaluation"*, KEK Report 91-11.

[18] S. Jadach and J.H. Kühn, *" The Monte Carlo Program TIPTOP for Heavy Fermion Production and Decay at LEP and SLC"*, MPI-PAE/Pth 64/86 (1986).

[19] I.I. Bigi, V.S. Fadin and V. Khoze, University of Notre Dame preprint, UND-HEP-91-BIG03 (1991).

[20] H. Murayama and Y. Sumino, in preparation.

[21] The use of the Coulombic potential allows us to check our numerical program to calculate the imaginary part of the Green's function $G(\mathbf{x}=0;E)$ in eq. (3.20) against the known analytic expression of Fadin and Khoze [5]. The dashed line in Fig. 4 for the constant toponium width $\Gamma_\Theta = 2\Gamma_t(m_t^2)$ agrees at 1 % level with the analytic results, which tests the accuracy of our numerical program to solve the Schrödinger equation.

[22] Within the general relativistic formalism containing unstable particles, the unitarity relation is preserved only when the running of the particles' self-energies are properly taken into account in the propagators [23].

[23] M. Veltman, *Physica* 29, 186 (1963)

[24] The running top quark width as obtained from the imaginary part of the one-loop top-quark self energy diagram in the renormalizable covariant (R_ξ) gauge is:

$$\Gamma_t(s) = \theta(s-m_W^2)\frac{G_F\sqrt{s}}{8\pi\sqrt{2}} \times \begin{cases} s - 3\frac{m_W^4}{s} + 2\frac{m_W^6}{s^2} & \text{for } \xi > \frac{s}{m_W^2} \\ m_t^2 - 3\frac{m_W^4}{s} + 2\frac{m_W^6}{s^2} + \xi\frac{m_W^2}{s}(2-\xi\frac{m_W^2}{s})(s-m_t^2) & \text{for } 1 < \xi < \frac{s}{m_W^2} \end{cases}$$

[25] B.W. Lee, C. Quigg and H.B. Thacker, *Phys. Rev.* D16, 1519 (1977);
M.S. Chanowitz and M.K. Gaillard, *Nucl. Phys.* B261, 379 (1985).

[26] G. Altarelli, N. Cabibbo, G. Corbo, L. Maiani and G. Martinelli, *Nucl. Phys.* **B208**, 365 (1982).

[27] The angular average of the spin factor $F(n,\bar{n})$ in eq. (4.17) makes Γ_Θ slightly larger than this naive estimate.

[28] J. Schwinger, *"Particles, Sources and Fields"*, Vol. 2 (Addison–Wesley, New York 1973), Chap. 5–4.

[29] T. Appelquist, M. Dine and I.J. Muzimich, *Phys. Lett.* **69B**, 231 (1977);
F. Feinberg, *Phys. Rev. Lett.* **39**, 316 (1977);
W. Fischer, *Nucl. Phys.* **B129**, 157 (1977).

[30] A. Billoier, *Phys. Lett.* **92B**, 343 (1980).

[31] K. Hagiwara, S. Jacobs, M.G. Olsson and K.J. Miller, *Phys. Lett.* **130B**, 209 (1983).

[32] G. Grumberg, *Phys. Lett.* **95B**, 70 (1980).

[33] W. Buchmüller, S.-H.H. Tye, *Phys. Rev.* **D24**, 132 (1981);
W. Buchmüller, G. Grunberg and S.-H.H. Tye, *Phys. Rev. Lett.* **45**, 103, 587(E) (1980).

[34] D. J. Gross and F. Wilczek, *Phys. Rev. Lett.* **30**, 1343 (1973);
H. D. Politzer, *ibid,* **30**, 1346 (1973).

[35] T. Appelquist and J. Carazzone, *Phys. Rev.* **D11**, 2856 (1975).

[36] S. Weinberg, *Phys. Lett.* **91B**, 51 (1980);
L. Hall, *Nucl. Phys.* **B178**, 75 (1981).

[37] If we use the approximate expressions presented by the Particle Data Group [38], the values of $\Lambda_{\overline{\rm MS}}^{(n_f)}$ become as follows: $\Lambda_{\overline{\rm MS}}^{(5)} = (0.068, 0.140, 0.253, 0.416)$ GeV and $\Lambda_{\overline{\rm MS}}^{(4)} = (0.111, 0.212, 0.362, 0.565)$ GeV for $\alpha_s(m_Z)_{\overline{\rm MS}} = (0.10, 0.11, 0.12, 0.13)$, respectively. These values are about 6–7% larger than the values quoted in Table 2.

[38] Review of Particle Propaties, Particle Data Group, *Phys. Lett.* **B239**, 1 (1990).

[39] C. Quigg and J. L. Rosner, *Phys. Rep.* **56**, 167 (1979).

[40] In order to obtain the perturbative potential where the second coefficient b_1 also exhibits the decoupling of heavy quarks, we need to use the two-loop β function in the momentum subtraction scheme [41], which can only be solved numerically. We used the $\overline{\rm MS}$ coupling constant for convenience since the effect of the running of the coefficient b_1 has been found to be negligibly small [42].

[41] T. Yoshino and K. Hagiwara, *Z. Phys.* **C24**, 185 (1984).

[42] K. Hagiwara, A. D. Martin and A. W. Peacock, *Z. Phys.* **C33**, 135 (1986).

[43] A. X. El-Khadra, G. Hockney, A. Kronfeld and P. Mackenzie, Fermilab preprint, Fermilab-PUB-91/354-T (1992);
C. Davies, B. Thacker and P. Lepage, Cornell Univ. preprint (1992).

[44] A. Martin, *Phys. Lett.* **93B**, 338 (1980).

[45] E. Eichten, K. Gottfried, T. Kinoshita, K. D. Lane and T. M. Yan, *Phys. Rev.* **D17**, 3090 (1978); *ibid*, **D21**, 313 (E) (1980); *ibid*, **D21**, 203 (1980).

[46] J. L. Richardson, *Phys. Lett.* **82B**, 272 (1979).

[47] K. Fujii, Talk presented at *the 1st Workshop on Physics and Experiments at Linear Colliders* (Saariselkä, Finland 1991), to be published in the proceedings.

[48] R. Barbieri, R. Gatto, R. Kögerler and Z. Kunszt, *Phys. Lett.* **57B**, 455 (1975).

[49] More generally, the true Γ_Θ should vanish above the kinematical cut-off $\Lambda^2_{kin} = (m_t + E/2)^2 - m_W^2$, since neither t nor $\bar{t}$ can decay when $\mathrm{p}^2 > \Lambda^2_{kin}$. The argument here shows that Γ_Θ becomes negligible well below the kinematical cut-off Λ_{kin}.

Tables

	Symbol	$\tilde{G}(\mathrm{p};E)$	Γ_Θ
constant width (σ_{tot})	σ_{C1}	constant	constant
constant width ($\int d\sigma$)	σ_{C2}	constant	running
running width	σ_R	running	running

Table 1

Notation for the total $t\bar{t}$ production cross section calculated by various approximations. When the running of the width is consistently taken into account in both $\tilde{G}(\mathrm{p};E)$ and Γ_Θ, the total cross section as calculated by using the optical theorem (σ_R) agrees with the integral of the differential cross section.

$\alpha_s(m_Z)_{\overline{\mathrm{MS}}}$	0.10	0.11	0.12	0.13	0.14
$\Lambda^{(5)}_{\overline{\mathrm{MS}}}$ (GeV)	0.064	0.131	0.237	0.390	0.598
$\Lambda^{(4)}_{\overline{\mathrm{MS}}}$ (GeV)	0.104	0.198	0.339	0.533	0.783
m_c (GeV)	1.105	1.298	1.550	1.898	2.375
m_b (GeV)	4.556	4.728	4.956	5.279	5.731
r_0 (GeV^{-1})	0.208	0.233	0.235	0.207	0.168
r_1 (GeV^{-1})	3.962	3.808	3.740	3.745	3.749
a (GeV^2)	0.359	0.354	0.357	0.373	0.401
χ^2	16.57	17.98	19.30	20.38	20.87

Table 2

Parameters of the QCD motivated potential fitted to the charmonium and bottomonium data, together with the corresponding minimal χ^2. The $\Lambda^{(5)}_{\overline{\mathrm{MS}}}$ values are fixed by the definition (5.8) with $m_Z = 91.17$ GeV, and the corresponding $\Lambda^{(4)}_{\overline{\mathrm{MS}}}$ values are calculated by the matching condition (5.11) at $m_b = 5$ GeV. The remaining five parameters m_c, m_b, r_0, r_1 and a have been fitted to the data which are listed in Table 3.

	$\alpha_s(m_Z)_{\overline{\rm MS}}$	QCD						Martin		Cornell		Richardson	
		0.11		0.12		0.13							
			χ^2		χ^2		χ^2		χ^2		χ^2		χ^2
$c\bar{c}$ data:													
$m(1S)$	3068±2	3068	0	3068	0	3068	0	3068	0	3068	0	3068	0
$m(1P)-m(1S)$	457±10	429	8.1	425	10.2	423	11.7	443	1.9	428	8.5	423	11.6
Γ_2/Γ_1	0.432±0.06	0.496	1.2	0.472	0.5	0.448	0.1	0.385	0.6	0.502	1.4	0.437	0
$b\bar{b}$ data:													
$m(1S)$	9452±2.5	9452	0	9452	0	9452	0	9452.6	0.1	9452	0	9452	0
$m(2S)-m(1S)$	567±3	569	0.7	570	0.8	570	1.0	576	9.9	556	13.2	569	0.6
$m(3S)-m(1S)$	900±2.5	902	0.9	902	0.9	902	0.8	911	19.0	904	2.9	899	0.1
$m(1P)-m(1S)$	448±2.5	447	0.3	447	0.3	447	0.3	417	152.8	450	0.9	452	2.0
$m(2P)-m(1S)$	809±6	796	4.5	797	4.3	797	4.2	800	2.2	810	0	805	0.5
Γ_2/Γ_1	0.439±0.03	0.397	1.9	0.399	1.8	0.399	1.8	0.492	3.1	0.414	0.7	0.407	1.2
Γ_3/Γ_1	0.328±0.03	0.307	0.5	0.307	0.5	0.306	0.5	0.329	0	0.301	0.8	0.283	2.2
χ^2_{tot}			18.0		19.3		20.4		189.7		28.3		18.1

Table 3

The optimum fits to charmonium and bottomonium data for various phenomenological potentials. The contribution of each data point to χ^2 and their sum are also given. Masses are given in the MeV units. The QCD motivated potential has the two-loop improved short distance behavior for a given value of $\alpha_s(m_Z)_{\overline{\rm MS}}$. The parameters of the fitted potentials are listed in Table 2 and in the text. Γ_n's are the leptonic widths of the nS states. Only their ratios have been fitted because of the large perturbative QCD correction to the width. The mass difference $m(2S)-m(1S)$ for the charmonium has not been fitted since $m(2S)$ is affected by the mixing to the $D\bar{D}$ channel.

Figure Captions

Fig. 1 The diagram for the $t\bar{t}$ pair production process and their subsequent decays into bW's. The box with the dashed line shows the three-point function $K(x,y,z)$ that carries the information of the toponium resonance.

Fig. 2 A figure that shows the time evolution of the non-relativistic $t\bar{t}$ system.

Fig. 3 Diagram representing $\Pi_t^{\mu\nu}(q)$.

Fig. 4 The energy-dependence of the total cross sections for the Coulombic potential $V = -C_F\alpha_s/r$ calculated with the constant widths and the running widths, where $m_t = 150\,\mathrm{GeV}$ and $\alpha_s = 0.16$. No Z^0 contribution is included. The energy is measured from the threshold: $E = \sqrt{s} - 2m_t$. The dashed curve (σ_{c1}) shows the total cross section calculated via the optical theorem with the constant widths; the dotted curve (σ_{c2}) shows the total cross section calculated from integrating over the differential cross section formula with the constant widths; and the solid curve (σ_R) shows the total cross section with the running widths. The notation is summarized in Table 1.

Fig. 5 The unitarity relation between the diagrams related to the $t\bar{t}$ pair production process.

Fig. 6 The ratio of the running toponium width $\Gamma_\Theta(E,\mathrm{p})$ to twice the on-shell top quark width $2\Gamma_t(m_t^2)$ for $m_t = 150\,\mathrm{GeV}$ versus the top (anti-top) quark momentum $|\mathrm{p}|$. $\Gamma_\Theta(E,\mathrm{p}) = (G_F m_t^3/4\sqrt{2}\pi)[\eta_1 - \eta_2(\mathrm{p}^2/m_t^2)]$ from eq. (4.22). The three curves are for $E = -2, 0, +2\,\mathrm{GeV}$.

Fig. 7 A figure showing the increase in the kinetic energy of the $t\bar{t}$ system due to the binding energy, as compared with the $V(r) = 0$ case.

Fig. 8 The momentum distribution, $|\tilde{G}(\mathrm{p};E)|^2$, of t or $\bar{t}$ with the phase space factor $4\pi\mathrm{p}^2$ for the Coulombic potential $V(r) = -C_F\alpha_s/r$ with $m_t = 150\,\mathrm{GeV}$ and $\alpha_s = 0.16$. The three solid curves are for $E = -2, 0, +2$ GeV. The dashed curve denotes the distribution at $E = +2\mathrm{GeV}$ in the zero binding limit ($V(r) = 0$).

Fig. 9 $-C_F/rV_P(r) = 1/\alpha_s(\mu_1)_{\overline{\mathrm{MS}}}$ versus r. The solid lines are for $n_f = 5$, $m_u = m_d = m_s = 0$, $m_c = 1.5\,\mathrm{GeV}$, and $m_b = 5\,\mathrm{GeV}$; the dashed lines are for the $n_f = 5$

massless theory; and the dotted lines are for the $n_f = 4$ massless theory. The upper and lower sets are for $\alpha_s(m_Z)_{\overline{\rm MS}} = 0.10$ and 0.12, respectively.

Fig. 10 The solid lines are our phenonenological QCD potential $V(r)$ for $\alpha_s(m_Z)_{\overline{\rm MS}} = 0.10, 0.11, 0.12$ and 0.13. The dashed (dotted) lines show the range of the potential accepted by the 5σ variation of the parameter r_0 (a) form its best fit value in Table 2 at $\alpha_s(m_Z)_{\overline{\rm MS}} = 0.12$.

Fig. 11 A comparison of different potentials. The solid lines show the QCD potentials for $\alpha_s(m_Z)_{\overline{\rm MS}} = 0.10, 0.11, 0.12$, and 0.13, where 0.10 is the uppermost solid line. The dotdashed, dashed, and dotted lines show the Cornell, Richardson, and Martin potentials, respectively.

Fig. 12 (a) The total cross sections versus energy for our QCD potential with $m_t = 100$ GeV ($\Gamma_t = 0.095$ GeV). $\alpha_s(m_Z)_{\overline{\rm MS}} = 0.11$, 0.12, and 0.13 for the dotdashed, solid, and dashed lines. The energy is measured from the threshold: $E = \sqrt{s} - 2m_t$.
(b) The same as (a) but for $m_t = 150$ GeV ($\Gamma_t = 0.90$ GeV).
(c) The same as (a) but for $m_t = 200$ GeV ($\Gamma_t = 2.5$ GeV).

Fig. 13 (a) The total cross section versus energy $E = \sqrt{s} - 2m_t$ at $m_t = 150$ GeV and $\alpha_s(m_Z)_{\overline{\rm MS}} = 0.12$. The solid line is the prediction of our QCD potential with the best fit parameters in Table 2. The dotted and dashed lines are obtained by shifting the parameter r_0 from its best fit value by five standard deviations upwards and downwards, respectively. The three curvs are almost degenerate in the figure. $\Gamma_t = 0.90$ GeV for $|V_{tb}|^2 = 1$.
(b) The same as (a) but for $\Gamma_t = 0.1$ GeV, or $|V_{tb}|^2 = 0.11$. The three curves are now distinguished clearly for higher resonances.

Fig. 14 $4\pi {\rm p}^2 |\tilde{G}({\rm p}; E)|^2$ versus $|{\rm p}|$ for our QCD potential with $m_t = 150$ GeV and $E = \sqrt{s} - 2m_t = 0$. $\alpha_s(m_Z)_{\overline{\rm MS}} = 0.11$, 0.12, and 0.13 for the dotdashed, solid, and dashed lines, respectively.

Fig. 15 $4\pi {\rm p}^2 |\tilde{G}({\rm p}; E)|^2$ versus $|{\rm p}|$ for our QCD potential with $m_t = 150$ GeV and $\alpha_s(m_Z)_{\overline{\rm MS}} = 0.12$. $E = \sqrt{s} - 2m_t = -6, -3, 0$, and $+3$ GeV for the dotdashed, solid, dashed, and dotted lines, respectively.

Fig. 16 (a) $4\pi {\rm p}^2 |\tilde{G}({\rm p}; E)|^2$ versus $|{\rm p}|$ for the various potentials with $m_t = 150$ GeV and $E = \sqrt{s} - 2m_t = 0$. The solid line shows the QCD potential with $\alpha_s(m_Z)_{\overline{\rm MS}} = 0.12$.

The dotdashed, dashed, and dotted lines show Cornell, Richardson, and Martin potentials, respectively.
(b) The same as (a) but the normalization of each curve is adjusted so that the peak values are the same.

Fig. 17 Feyman diagrams for the process $e^+e^- \to bW^+\bar{t}$ corrected for gluon exchange in the one-loop order. External self-energy corrections are not shown.

Fig. 18 The asymptotic behavior of the differential cross section $4\pi \mathrm{p}^2|\tilde{G}(\mathrm{p};E)|^2\Gamma_\Theta(E;\mathrm{p})$ for large top (anti-top) momentum $|\mathrm{p}|$. It is calculated for the Coulombic potential $V = -C_F\alpha_s/r$ with $m_t = 150\,\mathrm{GeV}$, $\alpha_s = 0.16$, and $E = -2\,\mathrm{GeV}$. The dashed lines show the position of zero. The behavior for $|\mathrm{p}| > 40\,\mathrm{GeV}$ is magnified and shown as the dotdashed line. The arrows indicate the positions of the cut-offs Λ_{kin}, Λ, and Λ_{eff}.

Fig. 19 The comparison of both sides of the unitarity relation (C.1) for the Green's function with the running toponium width at energies near the threshold. The solid line is calculated by evaluating the constant B in eq. (C.20), which approximates the l.h.s. of the identity in the small $1/\Lambda$ limit. The dashed line shows the r.h.s. of the relation (C.1)

$$\int_{\mathrm{p}^2<\Lambda^2} \frac{d^3\mathrm{p}}{(2\pi)^3}|\tilde{G}(\mathrm{p};E)|^2\Gamma_\Theta,$$

evaluated by the phase space integration. They are calculated for the Coulombic potential $V = -C_F\alpha_s/r$ with $m_t = 150\,\mathrm{GeV}$ and $\alpha_s = 0.16$. The energy is measured from the threshold: $E = \sqrt{s} - 2m_t$.

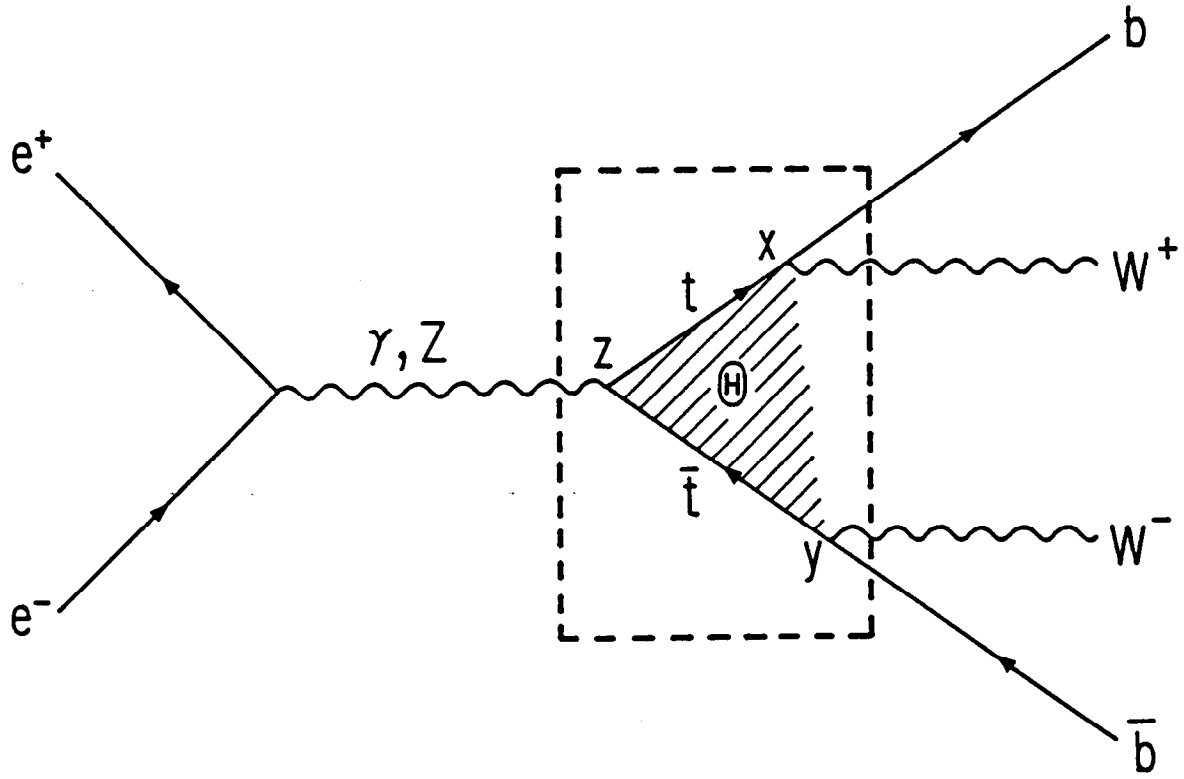

Fig.1

$\frac{1}{\Gamma}\frac{d\Gamma}{d\Theta}$
$\frac{dQ}{ds}$
Q_0
Q_D
X
t
$\bar{t}$
H
W^+
W^-
b
$\bar{b}$

Fig.2

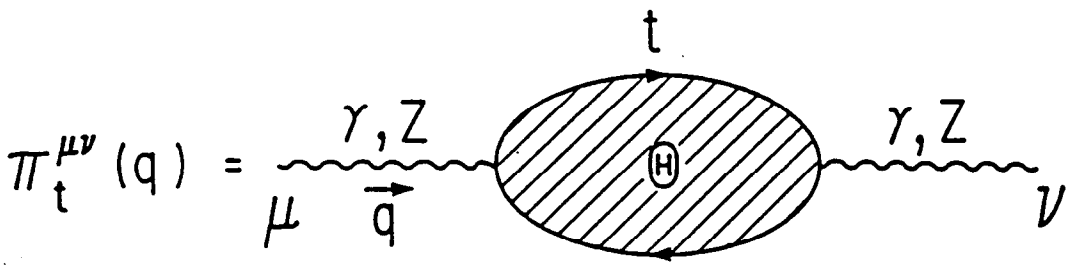

Fig.3

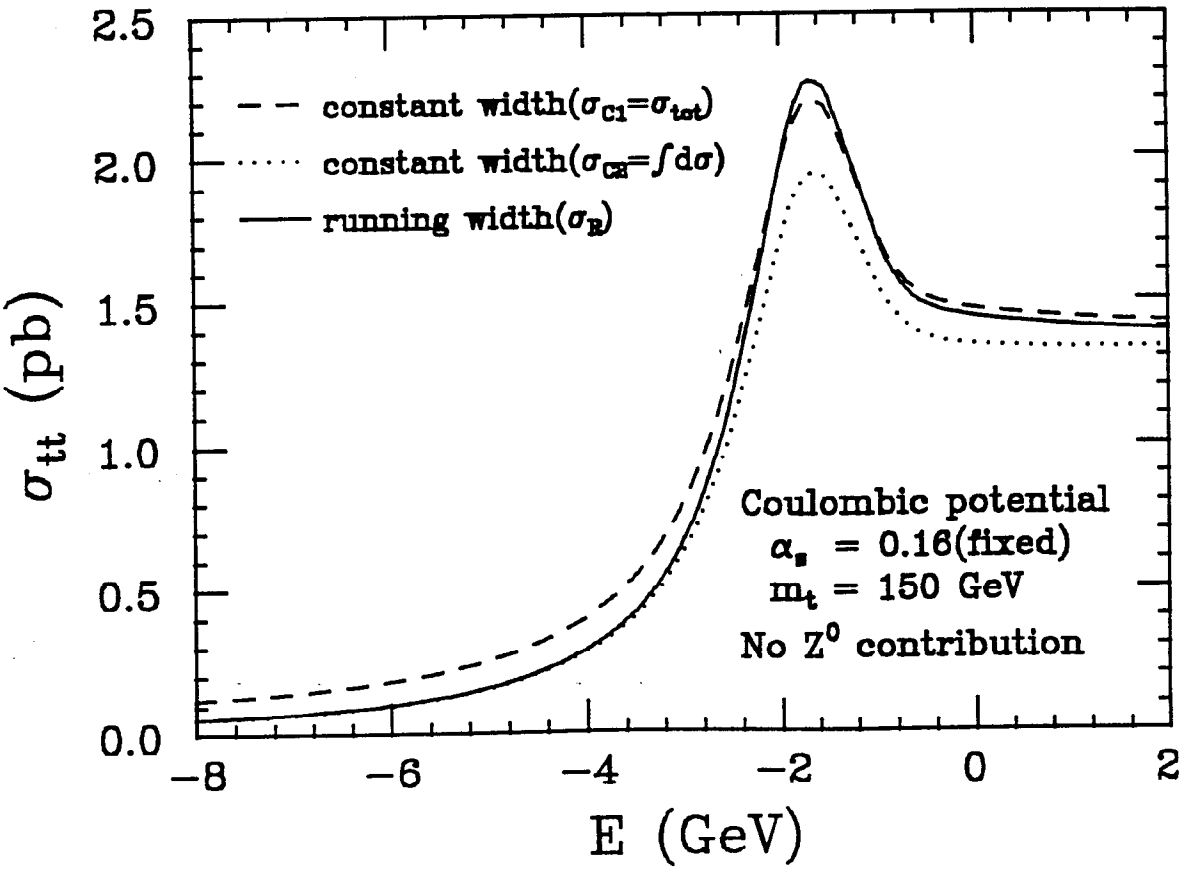
2.5
2.0
1.5
1.0
0.5
0.0
−8
−6
−4
−2
0
2
σ_{tt} (pb)
E (GeV)
constant width($\sigma_{C1}=\sigma_{tot}$)
constant width($\sigma_{C2}=\int d\sigma$)
running width(σ_R)
Coulombic potential
α_s = 0.16(fixed)
m_t = 150 GeV
No Z^0 contribution

Fig.4

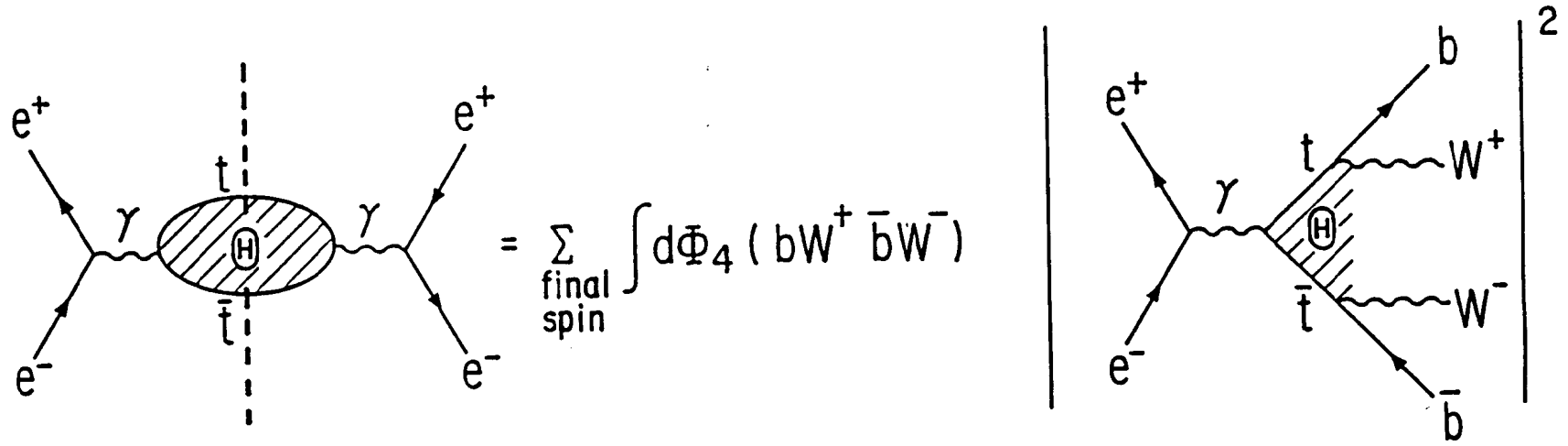

Fig.5

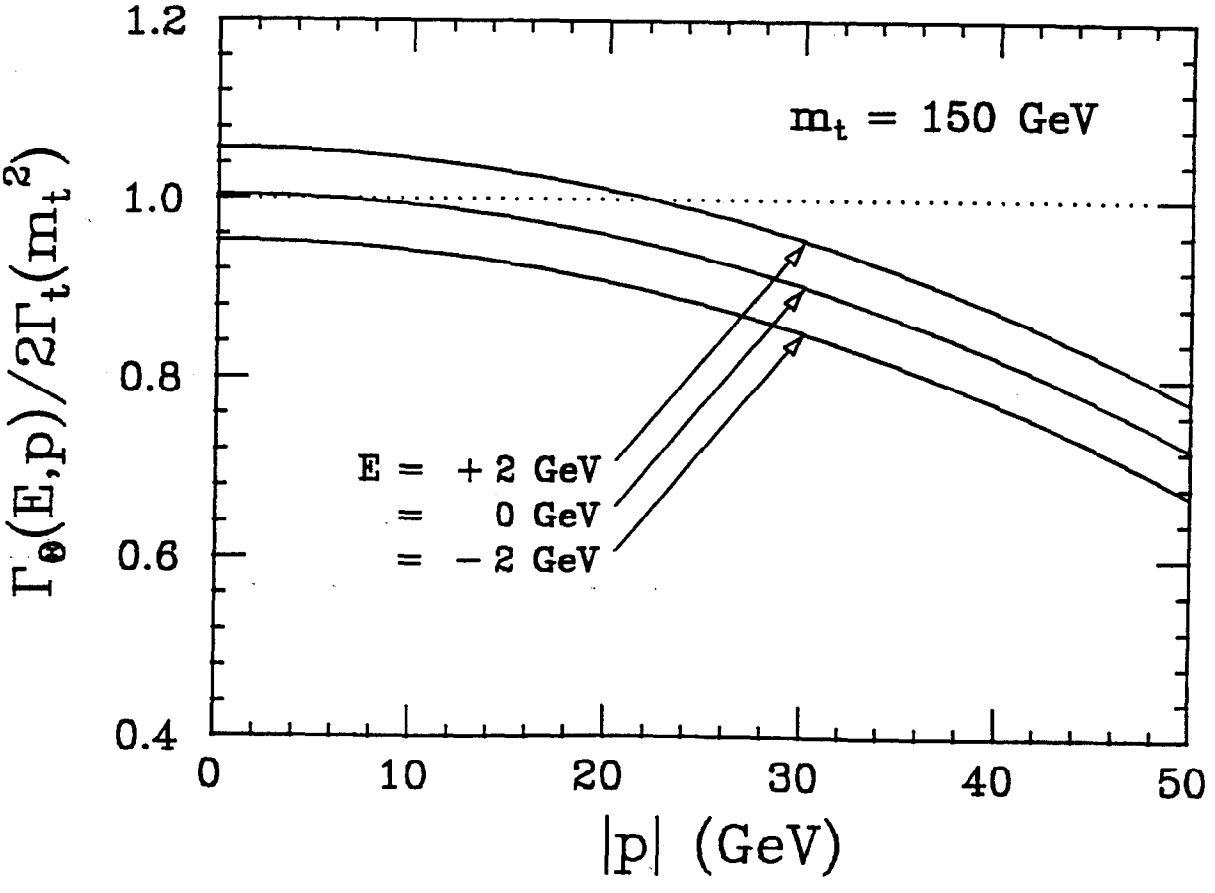
1.2
1.0
0.8
0.6
0.4
0
10
20
30
40
50
m_t = 150 GeV
E = + 2 GeV
= 0 GeV
= − 2 GeV
$\Gamma_\theta(E,p)/2\Gamma_t(m_t^2)$
|p| (GeV)

Fig.6

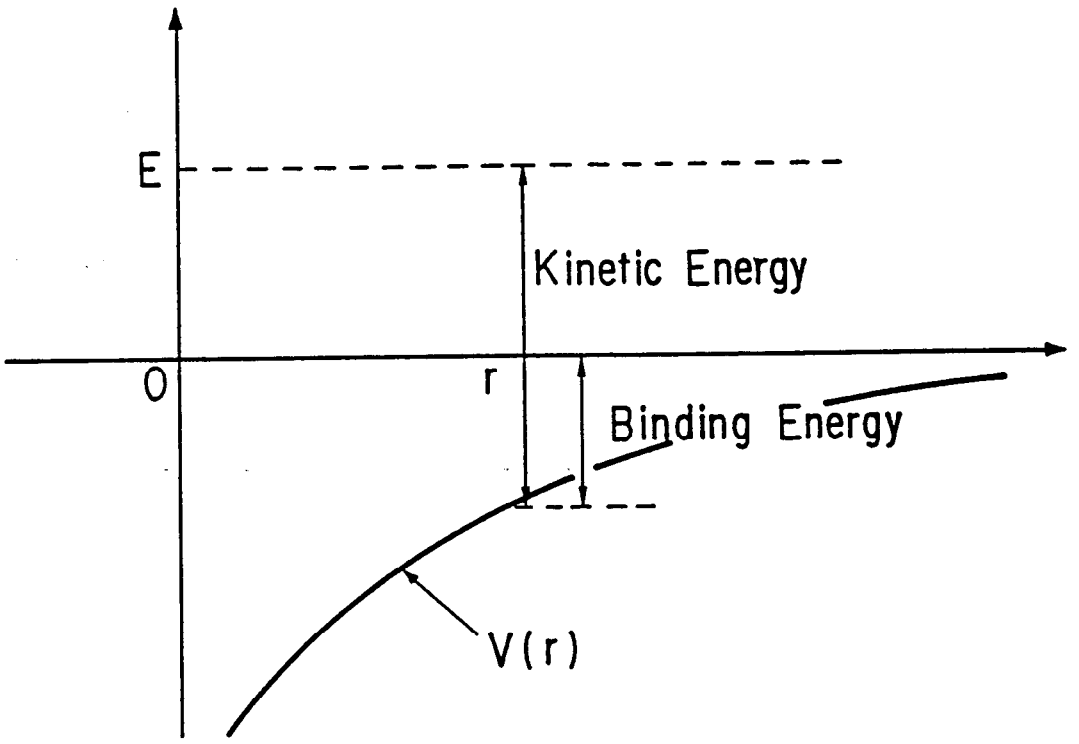

Fig.7

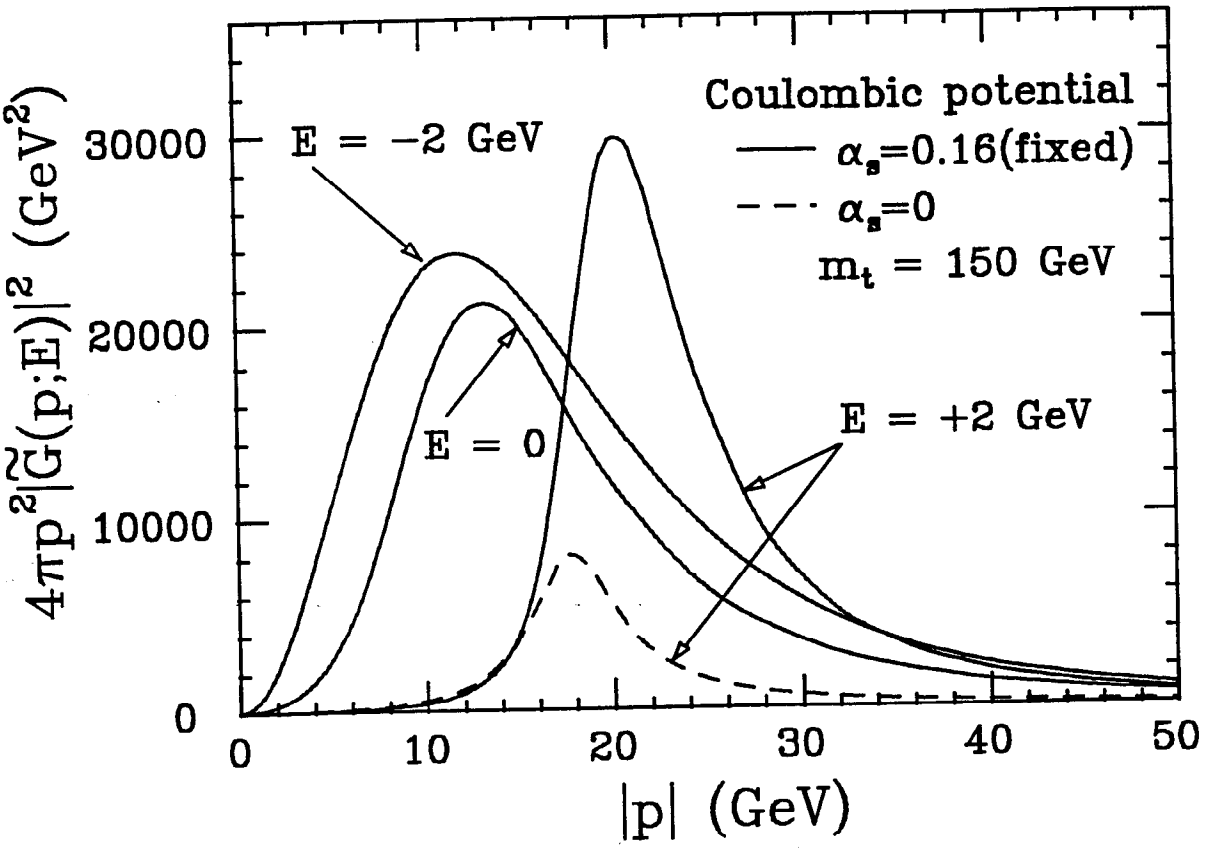
Coulombic potential
α_s=0.16(fixed)
α_s=0
m_t = 150 GeV
E = −2 GeV
E = 0
E = +2 GeV
$4\pi p^2|\tilde{G}(p;E)|^2$ (GeV^2)
|p| (GeV)
0
10000
20000
30000
0
10
20
30
40
50

Fig.8

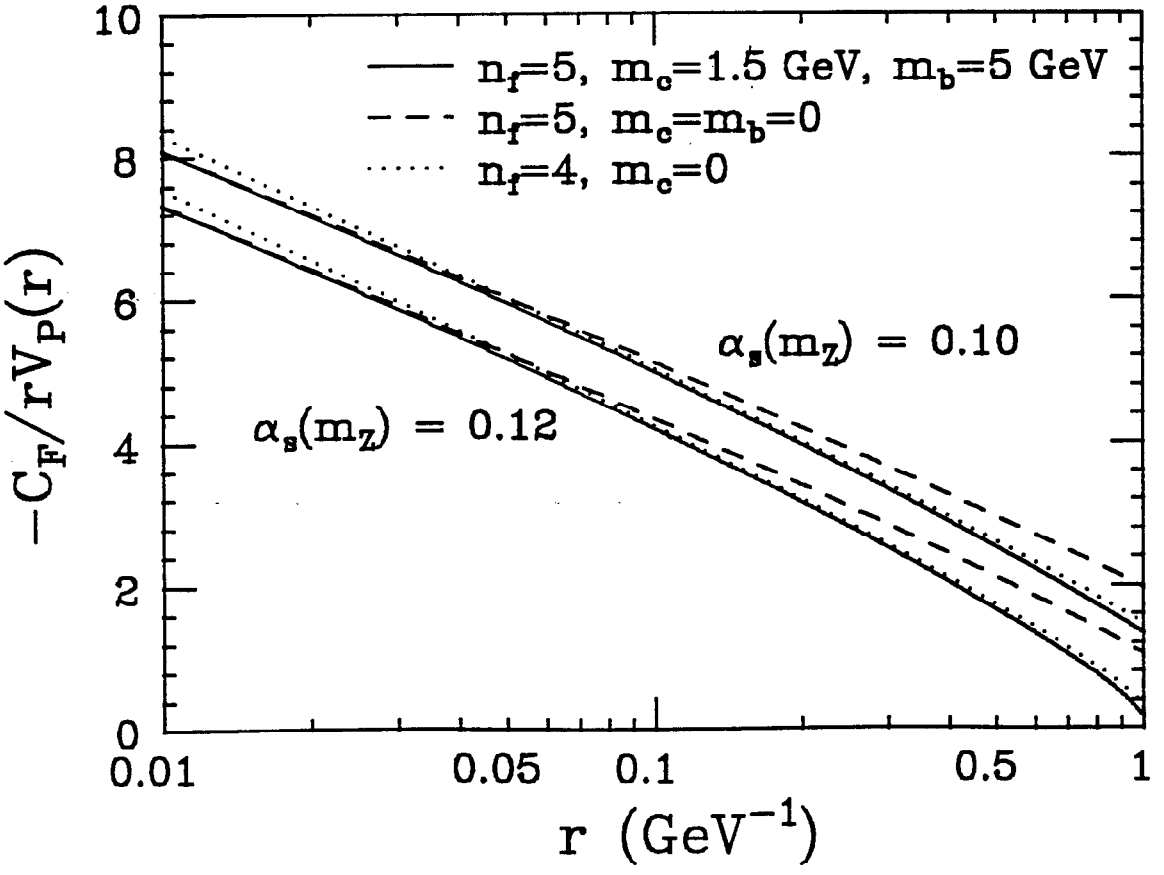
10
8
6
4
2
0
0.01
0.05
0.1
0.5
1
$-C_F/rV_P(r)$
r (GeV^{-1})
n_f=5, m_c=1.5 GeV, m_b=5 GeV
n_f=5, m_c=m_b=0
n_f=4, m_c=0
$\alpha_s(m_Z)$ = 0.10
$\alpha_s(m_Z)$ = 0.12

Fig.9

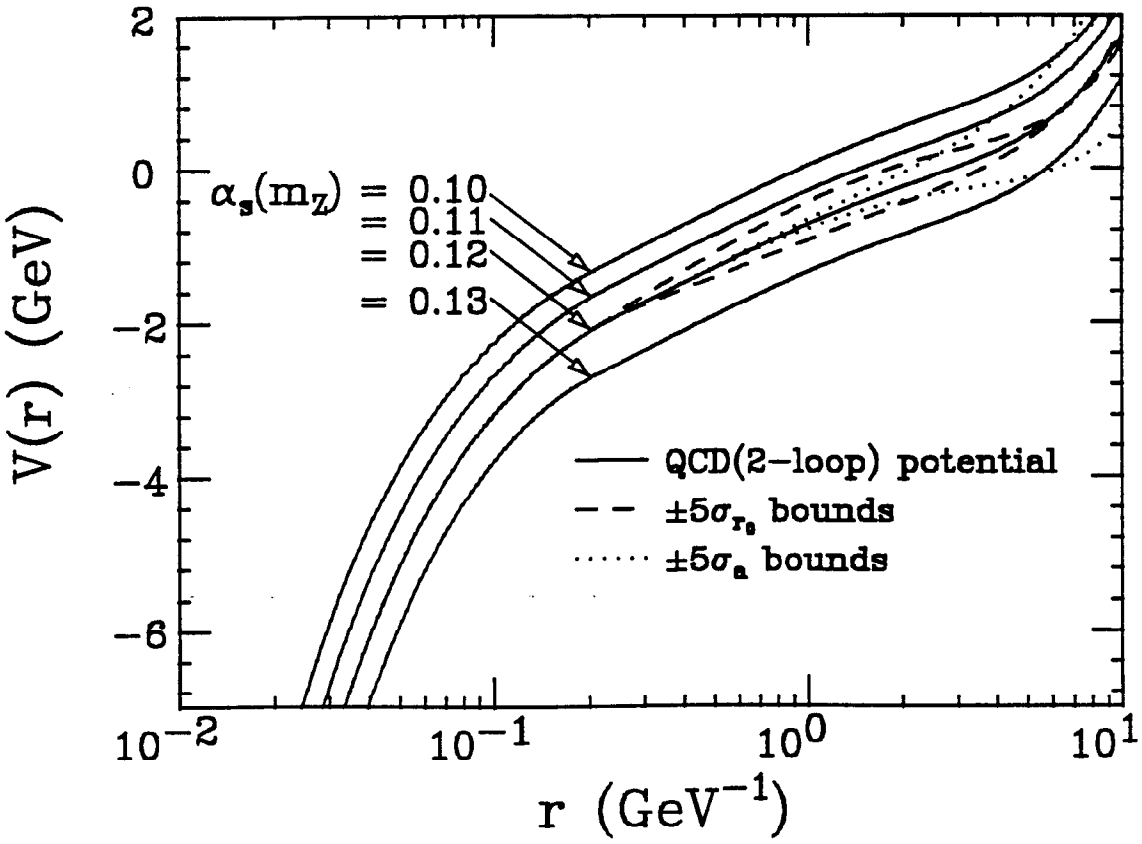
2
0
−2
−4
−6
V(r) (GeV)
$\alpha_s(m_Z)$ = 0.10
= 0.11
= 0.12
= 0.13
QCD(2−loop) potential
$\pm 5\sigma_{r_0}$ bounds
$\pm 5\sigma_a$ bounds
10^{-2}
10^{-1}
10^{0}
10^{1}
r (GeV^{-1})

Fig.10

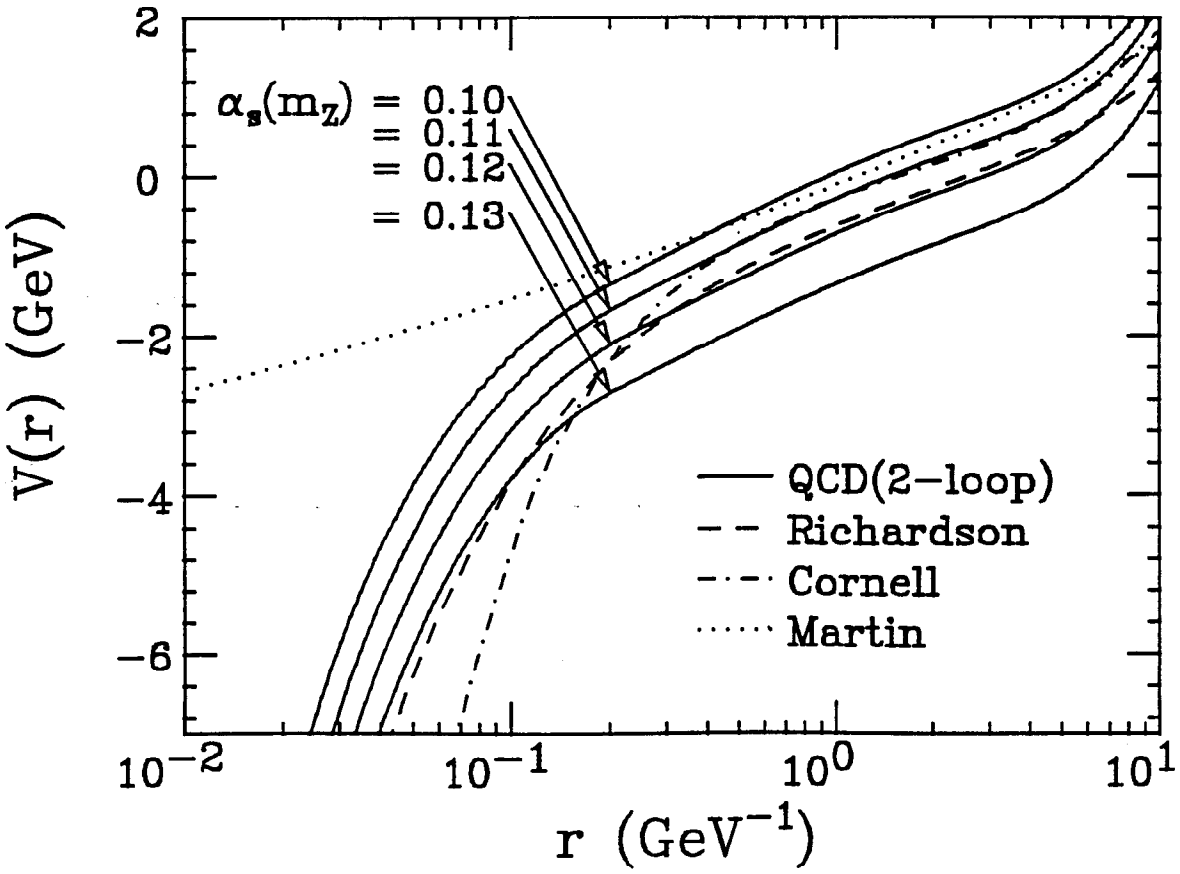
2
0
−2
−4
−6
V(r) (GeV)
$\alpha_s(m_Z)$ = 0.10
= 0.11
= 0.12
= 0.13
QCD(2−loop)
Richardson
Cornell
Martin
10^{-2}
10^{-1}
10^{0}
10^{1}
r (GeV^{-1})

Fig.11

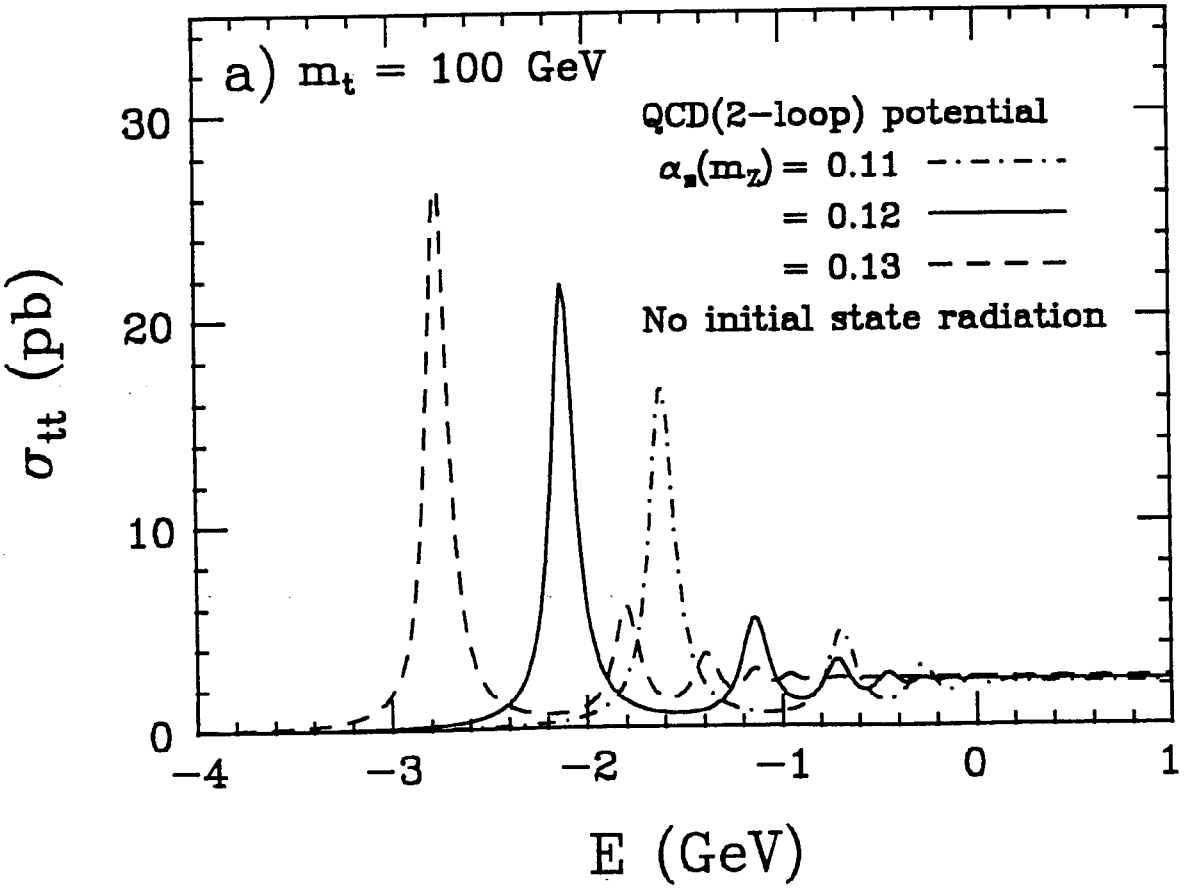
a) m_t = 100 GeV
QCD(2−loop) potential
$\alpha_s(m_Z)$ = 0.11
= 0.12
= 0.13
No initial state radiation
σ_{tt} (pb)
E (GeV)
30
20
10
0
−4
−3
−2
−1
0
1

Fig.12a

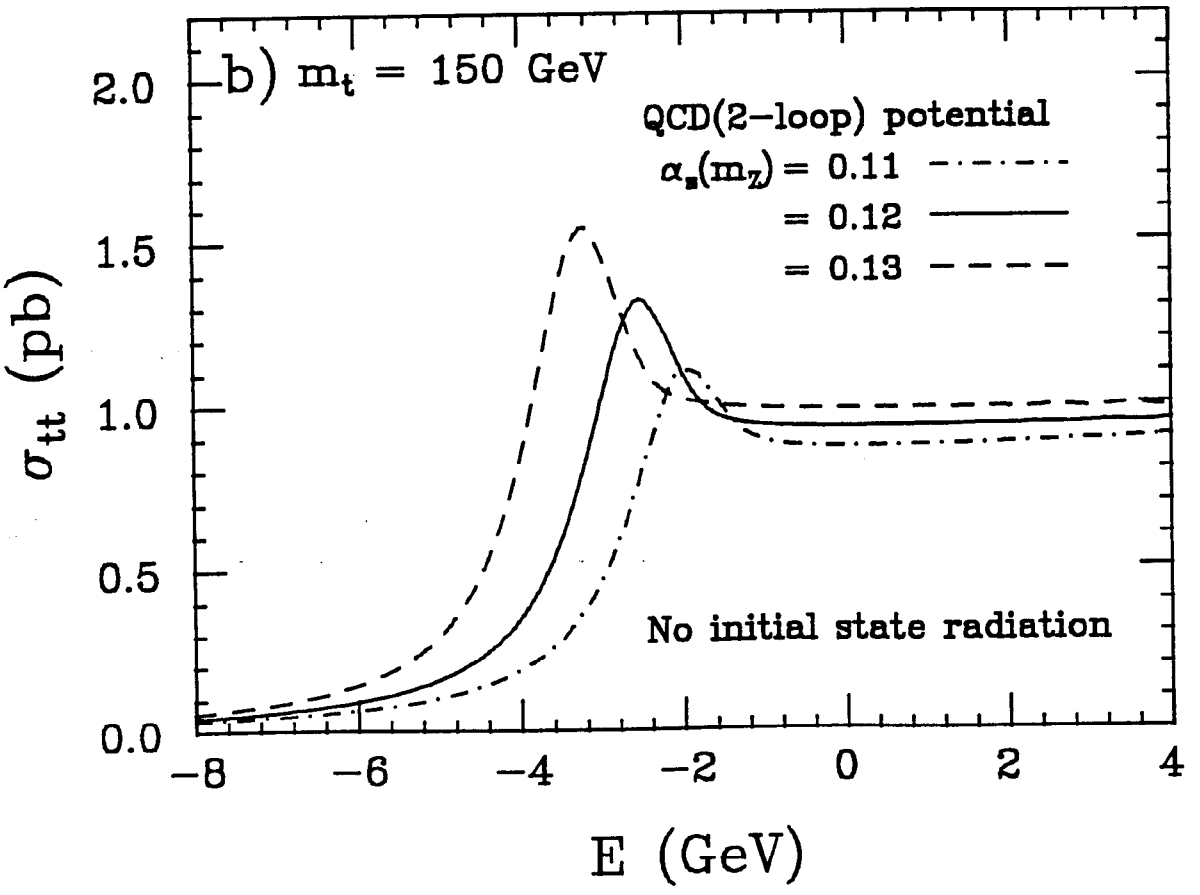
b) m_t = 150 GeV
QCD(2-loop) potential
$\alpha_s(m_Z)$ = 0.11
= 0.12
= 0.13
No initial state radiation
σ_{tt} (pb)
2.0
1.5
1.0
0.5
0.0
−8
−6
−4
−2
0
2
4
E (GeV)

Fig.12b

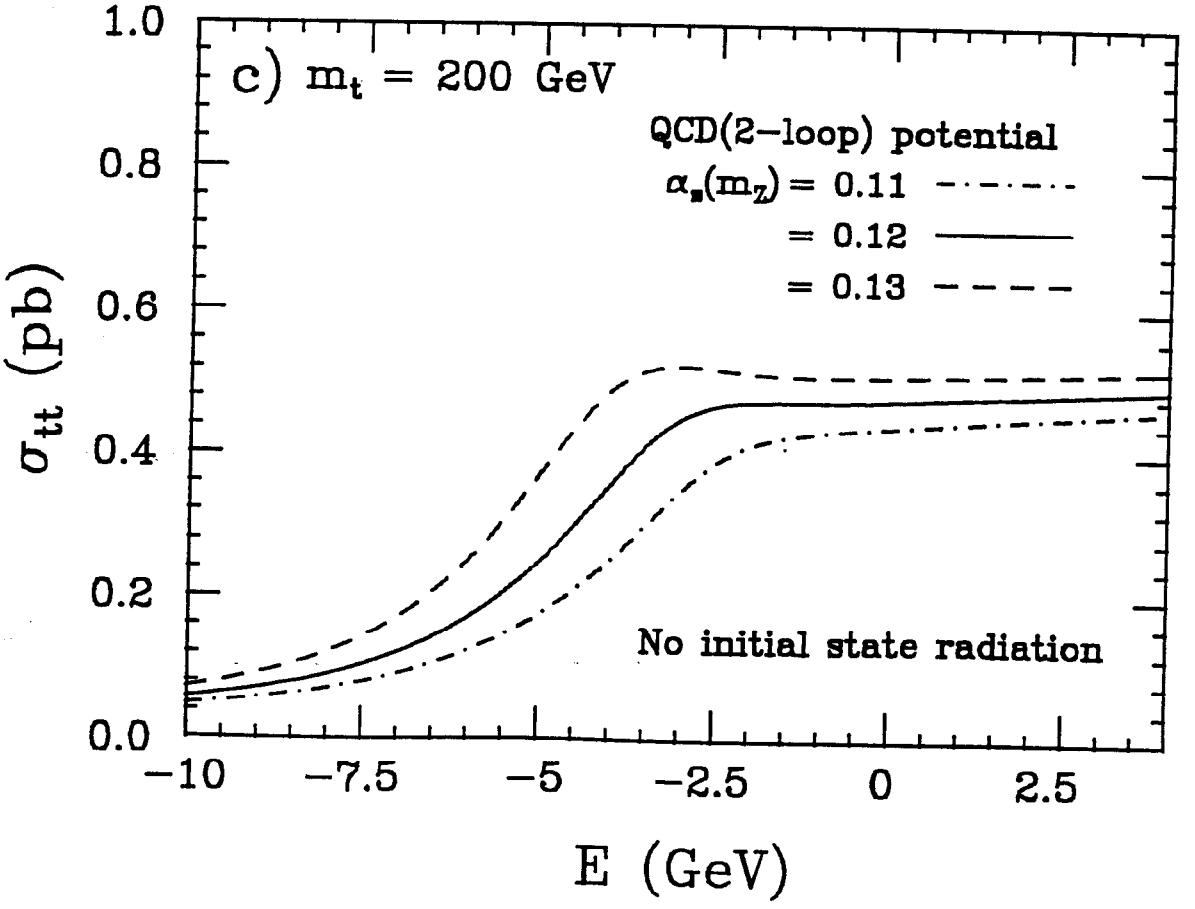
c) m_t = 200 GeV
QCD(2−loop) potential
$\alpha_s(m_Z)$ = 0.11
= 0.12
= 0.13
No initial state radiation
σ_{tt} (pb)
E (GeV)
1.0
0.8
0.6
0.4
0.2
0.0
−10
−7.5
−5
−2.5
0
2.5

Fig.12c

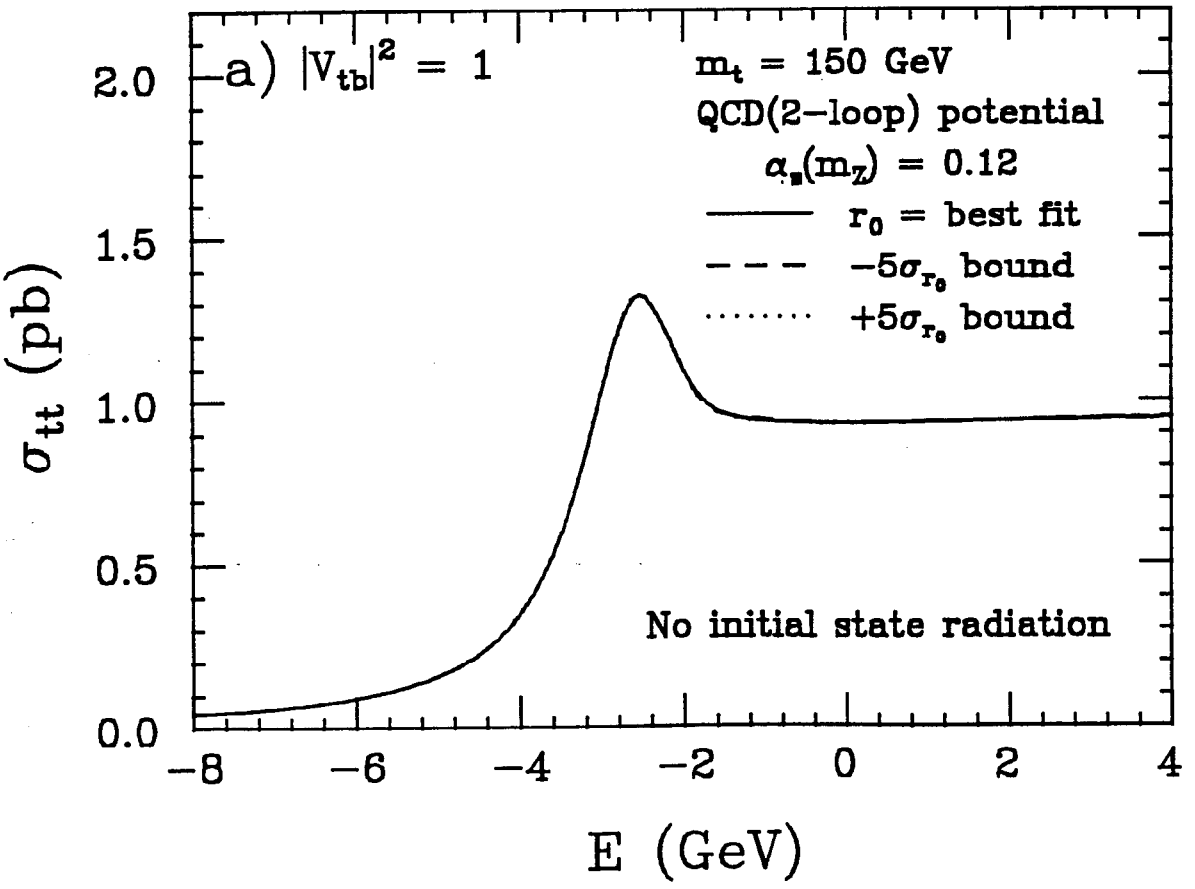
a) $|V_{tb}|^2 = 1$
m_t = 150 GeV
QCD(2−loop) potential
$\alpha_s(m_Z)$ = 0.12
r_0 = best fit
$-5\sigma_{r_0}$ bound
$+5\sigma_{r_0}$ bound
No initial state radiation
σ_{tt} (pb)
2.0
1.5
1.0
0.5
0.0
−8
−6
−4
−2
0
2
4
E (GeV)

Fig.13a

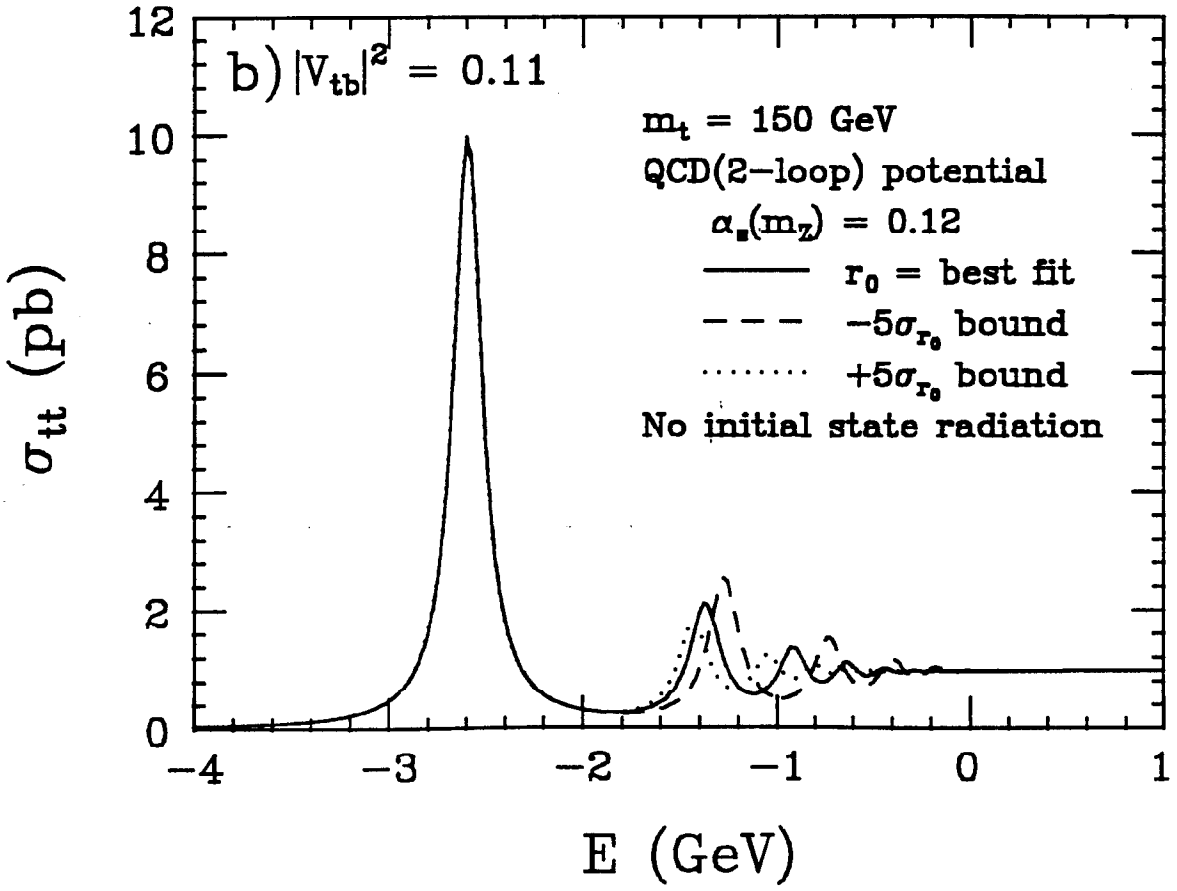
b) $|V_{tb}|^2 = 0.11$
m_t = 150 GeV
QCD(2−loop) potential
$\alpha_s(m_Z) = 0.12$
r_0 = best fit
$-5\sigma_{r_0}$ bound
$+5\sigma_{r_0}$ bound
No initial state radiation
σ_{tt} (pb)
E (GeV)
12
10
8
6
4
2
0
−4
−3
−2
−1
0
1

Fig.13b

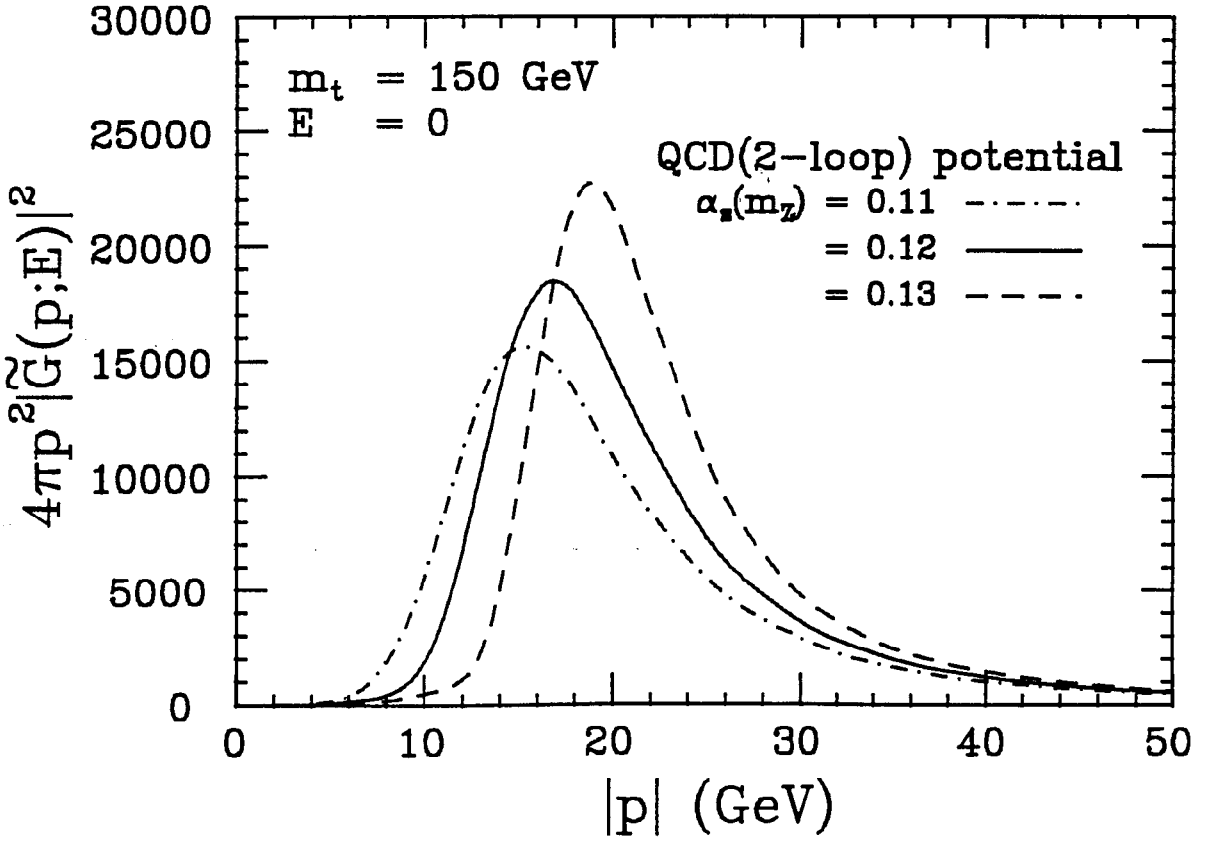
30000
25000
20000
15000
10000
5000
0
0
10
20
30
40
50
m_t = 150 GeV
E = 0
QCD(2-loop) potential
$\alpha_s(m_Z)$ = 0.11
= 0.12
= 0.13
$4\pi p^2|\tilde{G}(p;E)|^2$
|p| (GeV)

Fig.14

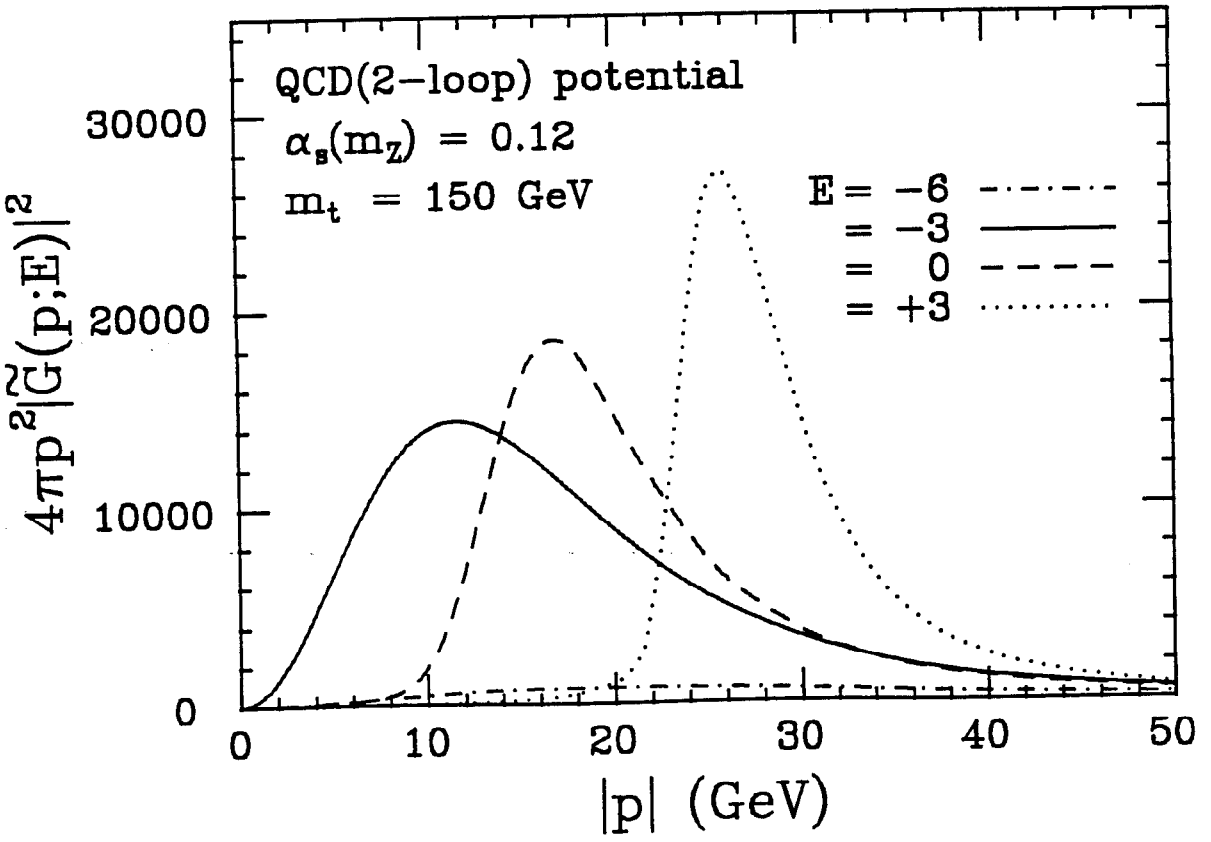
QCD(2−loop) potential
$\alpha_s(m_Z) = 0.12$
$m_t = 150$ GeV
E = −6
= −3
= 0
= +3
$4\pi p^2|\tilde{G}(p;E)|^2$
30000
20000
10000
0
0
10
20
30
40
50
|p| (GeV)

Fig.15

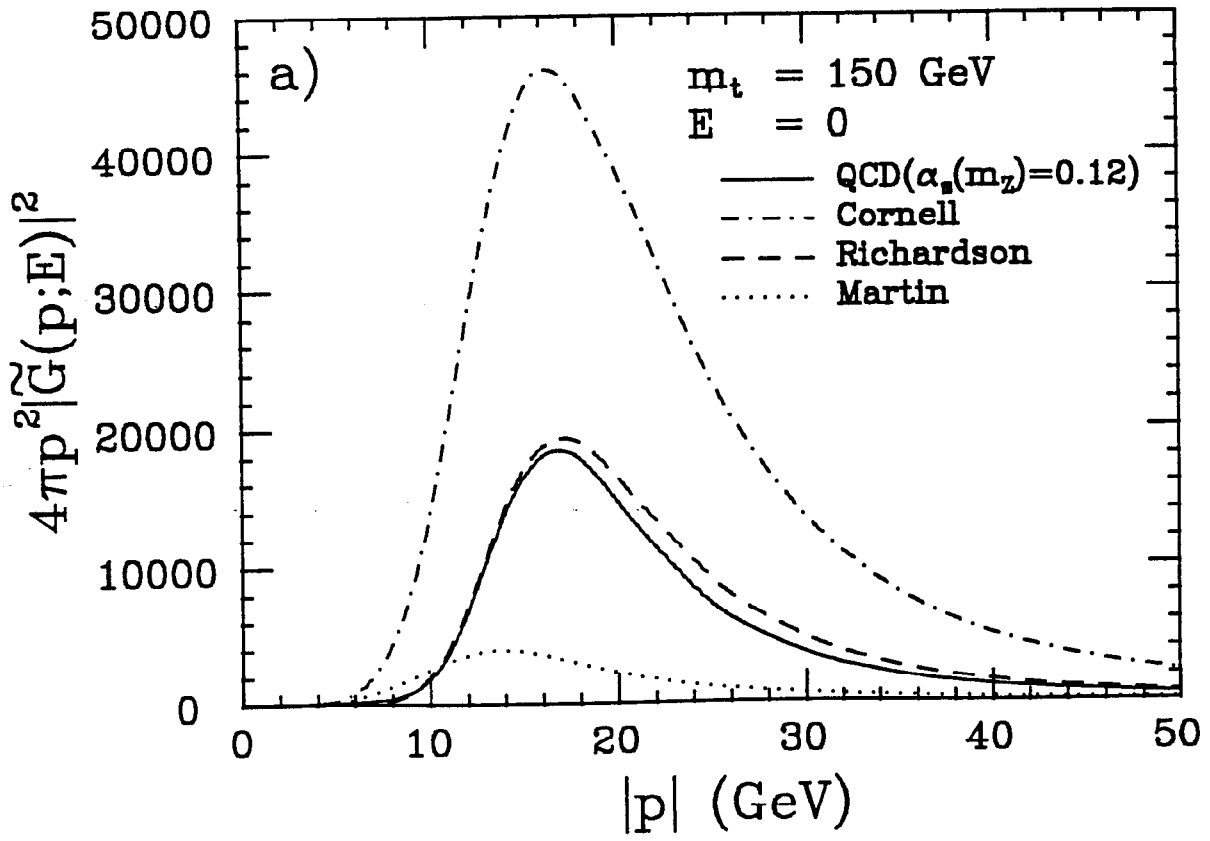
a)
m_t = 150 GeV
E = 0
QCD($\alpha_s(m_Z)$=0.12)
Cornell
Richardson
Martin
$4\pi p^2|\tilde{G}(p;E)|^2$
|p| (GeV)
0
10000
20000
30000
40000
50000
0
10
20
30
40
50

Fig.16a

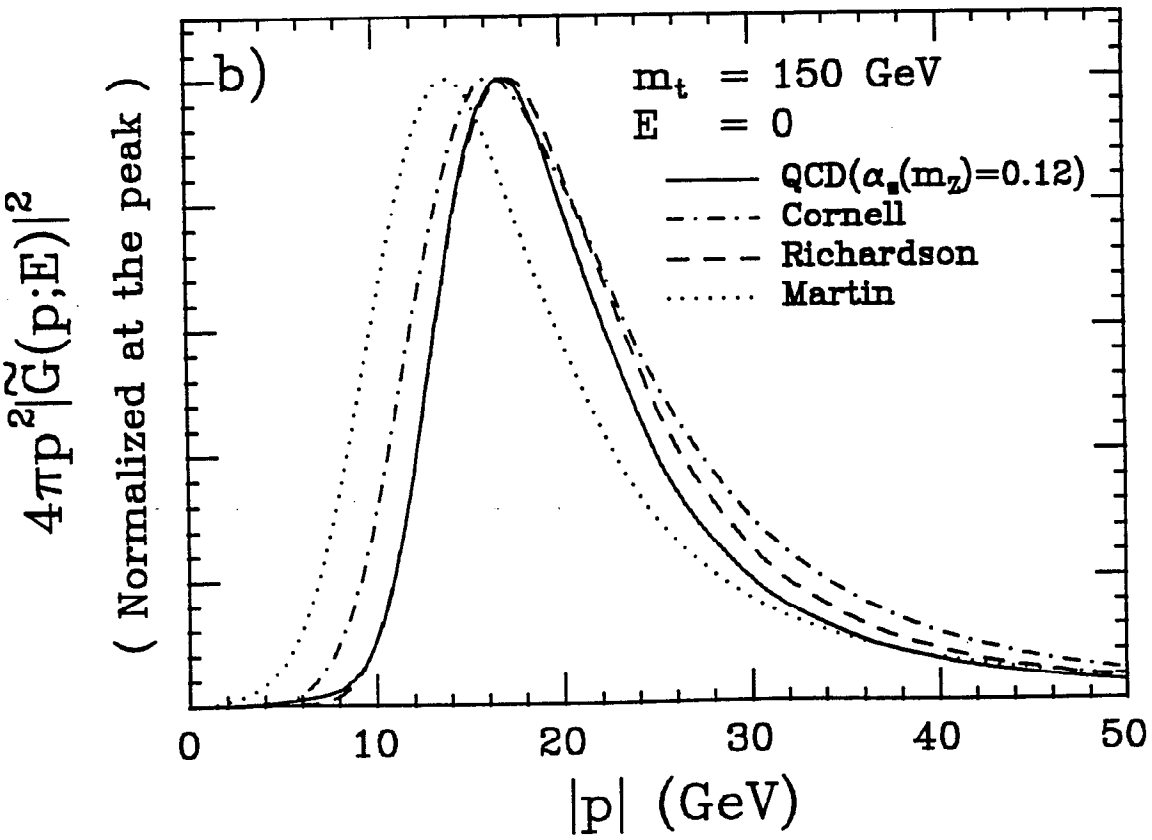
b)
m_t = 150 GeV
E = 0
QCD($\alpha_s(m_Z)$=0.12)
Cornell
Richardson
Martin
$4\pi p^2|\tilde{G}(p;E)|^2$
(Normalized at the peak)
0
10
20
30
40
50
|p| (GeV)

Fig.16b

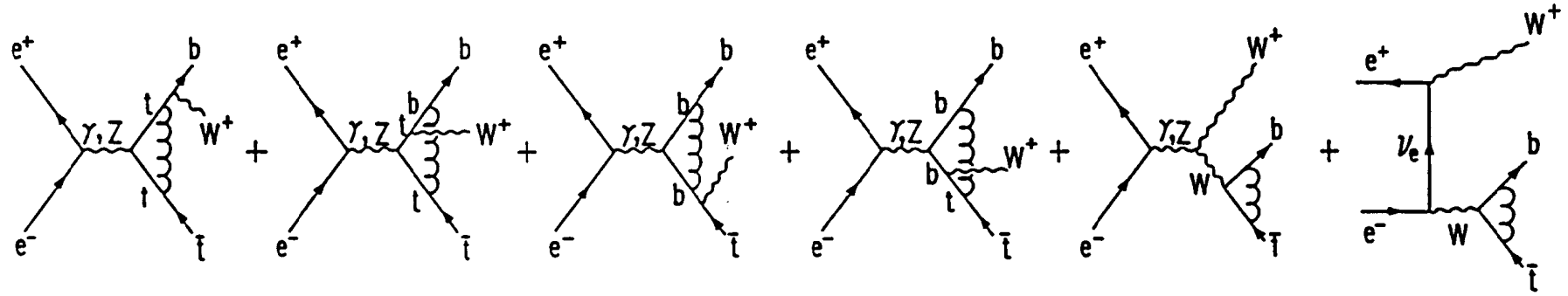

Fig.17

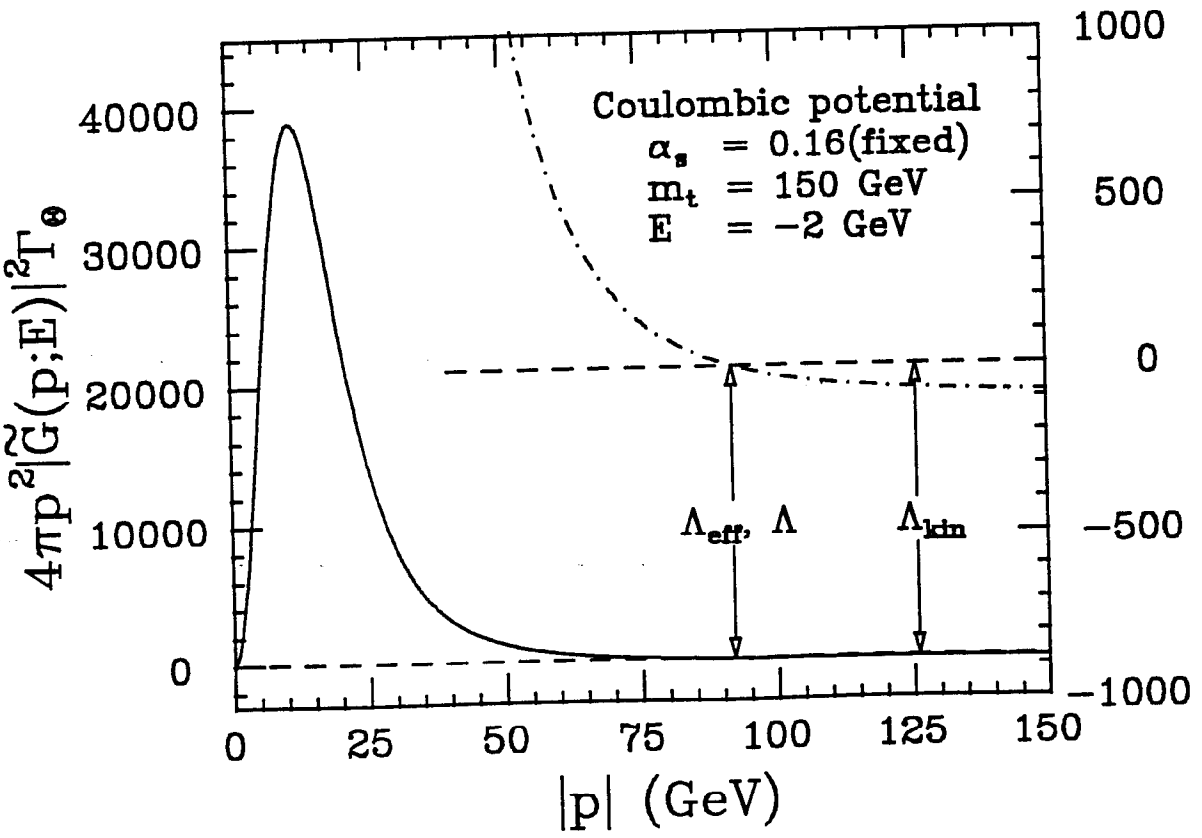
Coulombic potential
α_s = 0.16(fixed)
m_t = 150 GeV
E = −2 GeV
Λ_{eff}, Λ
Λ_{kin}
$4\pi p^2|\tilde{G}(p;E)|^2\Gamma_\Theta$
|p| (GeV)
0
10000
20000
30000
40000
0
25
50
75
100
125
150
1000
500
0
−500
−1000

Fig.18

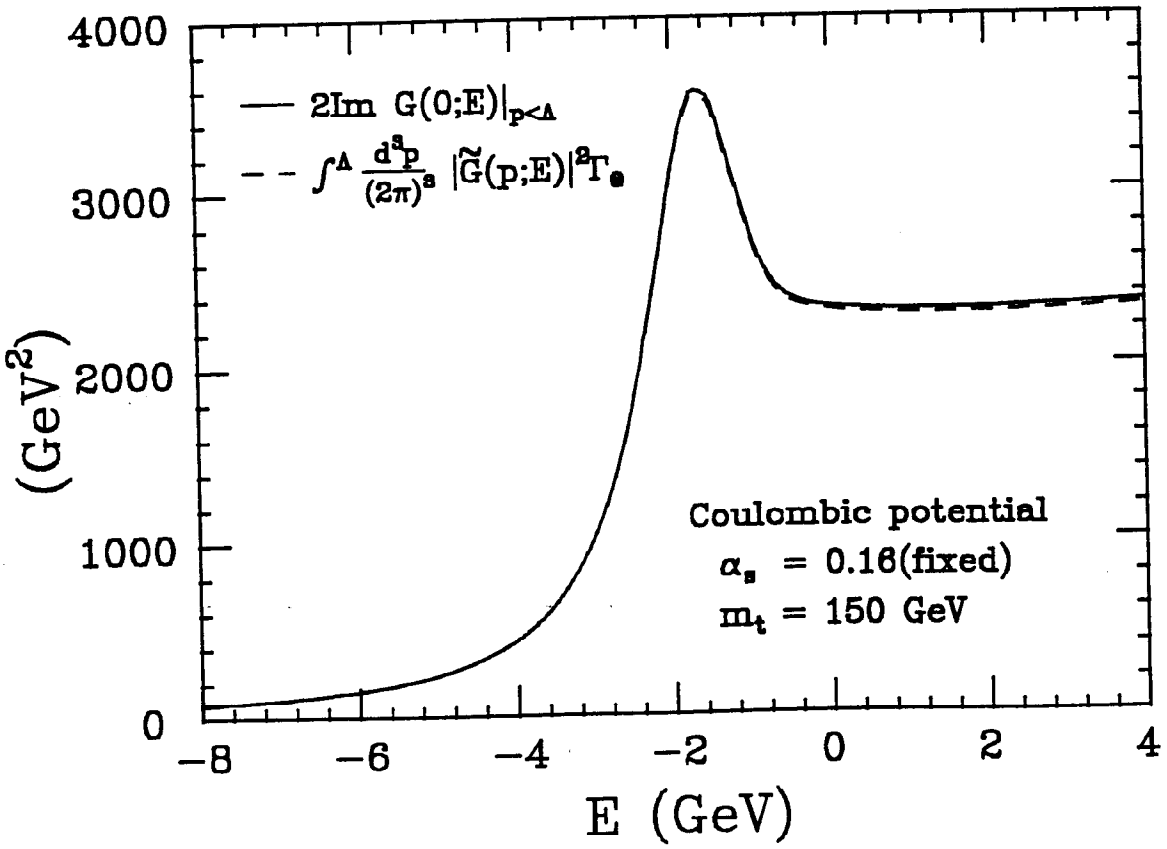
4000
3000
2000
1000
0
(GeV²)
— 2Im G(0;E)|p<Λ
- - ∫^Λ d³p/(2π)³ |G̃(p;E)|²T₀
Coulombic potential
αs = 0.16(fixed)
mt = 150 GeV
−8
−6
−4
−2
0
2
4
E (GeV)

Fig.19